IRON ACTS AS A KEY PLAYER IN BROWN ADIPOSE TISSUE THERMOGENIC ACTIVATION AND SKELETAL MUSCLE REGENERATION

by

WENYAN FU

(Under the Direction of HANG YIN)

ABSTRACT

Iron deficiency is the most common nutrition deficiency in the world. The manifestation of iron deficiency includes but is not limited to cold intolerance and muscle weakness, which associates two major organs: brown adipose tissue (BAT) and skeletal muscle.

BAT can be thermogenically activated under stimuli, such as β-adrenergic agonist and cold exposure. The activated BAT specializes in nonshivering thermogenesis to promote body temperature and consume energy. Whether BAT engages in iron deficiency induced cold intolerance and whether iron participates in BAT activation in unknown. Here we report that BAT activation induced TfR1-mediated iron uptake. Iron ion and transferrin receptor 1 (TfR1) were required for the thermogenic activation of BAT. Iron deprivation or TfR1 ablation in brown adipocyte dampened uncoupling respiration and blocked BAT mediated energy expenditure. On the contrary, iron supplement is sufficient to activate brown adipocyte without adrenergic stimuli. Mechanistically, iron catalyzed hydroxyl radical production via Fenton's reaction and further induced lipid peroxidation during brown adipocyte activation in mitochondria. Neutralization of

hydroxyl radical or lipid peroxidation blocked the BAT activation induced by iron. Our data indicates that chelatable iron plays critical roles in activating thermogenesis of BAT, which expands the physiological functions of iron in metabolism and provides an explanation of iron deficiency associated cold intolerance.

Iron deficiency is also highly associated with skeletal muscle dysfunction. Skeletal muscle possesses the great potential to regenerate upon injury by satellite cells. The life-long maintenance of muscle tissue is orchestrated by satellite cell-mediated muscle regeneration. The biological function of iron in skeletal muscle regeneration and satellite cells activity remains largely unknown. Our study shows that deprivation of iron impaired the proliferation of satellite cells both in vitro and in vivo and jeopardized skeletal muscle regeneration. Iron depletion stabilized hypoxia-induced factor 2 (HIF2α) in the nuclei, further blocking satellite cell proliferation via Rb1/E2F pathway. Moreover, pharmacological inhibition of HIF2α by PT-2385 improved muscle regeneration in iron deficient mice. Overall, our findings demonstrate a critical function of iron in muscle regeneration through HIF2α-Rb1/E2F signaling and provide a therapeutically target to promote muscle regeneration for iron deficient population.

INDEX WORDS: iron, metabolism, brown adipocyte, thermogenesis, mitochondria, ROS, satellite cell, proliferation, HIF2α

IRON ACTS AS A KEY PLAYER IN BROWN ADIPOSE TISSUE THERMOGENIC ACTIVATION AND SKELETAL MUSCLE REGENERATION

by

WENYAN FU

BS, WUHAN UNIVERSITY, CHINA, 2013

A Dissertation Submitted to the Graduate Faculty of The University of Georgia in Partial Fulfillment of the Requirements for the Degree

DOCTOR OF PHILOSOPHY

ATHENS, GEORGIA

2021

IRON ACTS AS A KEY PLAYER IN BROWN ADIPOSE TISSUE THERMOGENIC ACTIVATION AND SKELETAL MUSCLE REGENERATION

by

WENYAN FU

Major Professor:	Hang Yin
Committee:	Stephen Dalton
	Jarrod Call
	Shaying Zhao

Electronic Version Approved:

Ron Walcott
Vice Provost for Graduate Education and Dean of the Graduate School
The University of Georgia
December 2021

DEDICATION

This work is dedicated to my son, Arthur, my husband, Yang, and my parents.

I am grateful to all your love, accompany and support.

ACKNOWLEDGEMENTS

First and foremost, I would like to thank my advisor, Dr. Yin with deepest gratitude. Hang teaches me how to conduct good science step by step. He is serious about science and always guides me to think critically. Hang also gives me the strong support and freedom to explore science. His instruction, patience and understanding allow me to finish these projects that span several scientific disciplines. I want to thank my fellow Yin lab members, Yang and Amelia. We worked together on these projects, and I really appreciate their contribution to the work.

I also express my sincere appreciation to my committee members, Dr. Stephen Dalton, Dr. Jarrod Call, Dr. Shaying Zhao and Dr. Ito Takahiro for their helpful advice and insightful comments. And I want to thank Dr. Zachary Wood and Dr. Lance Wells, for their support and compliment at my student seminars as graduate coordinators.

I give my deepest appreciation to my family. Only without their love and support can I accomplish my Ph.D. study, especially in a foreign land.

TABLE OF CONTENTS

LIST OF FIGURES

CHAPTER 1

INTRODUCTION AND LITERSTURE REVIEW

1.1 Overview of Iron Metabolism

Iron is an essential trace metal for almost all living cells and organisms. Iron participates in multiple biological processes, including erythropoiesis, cellular respiration, cell signaling, cell growth and differentiation.

Iron metabolism

Iron metabolism is tightly controlled (**Figure 1.1**). Ferric iron binds to transferrin (Tf) to transport through the circulation. To import into cells, holo-Tf binds to transferrin receptor (TfR), forming holo-Tf-TfR complex. The entire complex is internalized by receptor-mediated endocytosis. The complex then breaks down in the endosome to release ferric iron because of the low pH (approximately pH 5.5) environment. Free ferric iron is reduced to ferrous iron by the ferric reductase six-transmembrane epithelial antigen of prostate 3 (STEAP3) in the endosome and transported into the cytosol by divalent metal transporter 1 (DMT1) to form labile iron pool (LIP). Apo-Tf bound to the TfR is then recycled to the cell surface for further iron uploading. The LIP is available for immediate cellular use. Part of the iron is stored in ferritin and excess iron is exported back to circulation by ferroportin (Fpn).

Iron utilization in cells

The labile iron pool is destined for storage, export, or metabolic utilization. In mammalian cells, mitochondria are thought to be the major hub for iron utilization. Several mechanisms

contribute to the delivery of iron into mitochondria, and it is cell-type specific. Mitoferrin (Mfrn), an inner membrane-bound iron transporter, may play an important role in mitochondrial iron uptake [1]. Disruption of the yeast Mfrn orthologues, MRS3 and MRS4, causes defects in iron metabolism and mitochondrial Fe–S cluster biogenesis [1]. Besides, iron is found to be delivered directly into mitochondria via "kiss and run" model, of which endosome forms transient contact with mitochondrial outer-membrane (OMM) to deliver iron [2].

Iron in the mitochondria functions as a cofactor in iron-sulfur cluster-containing proteins, heme-containing proteins, and iron ion-containing proteins, which are essential components of crucial enzymes involved in the electron transport chain (ETC), the tricarboxylic acid (TCA) and other cellular processes in mitochondria.

Iron also participates in Haber-Weiss and Fenton's reactions and generates ROS as the natural byproduct of oxygen metabolism in mitochondria. In the Fenton's reaction, iron acts as a catalyst and generates free hydroxyl radicals. The free hydroxy radicals engage in the second oxidation reactions in the mitochondria and cytosol. Hence, the principal source of ROS comes from mitochondria, and it can further be distributed to cytosol. At a physiological level, ROS in mitochondria and cytosol may function as critical intermediates of cellular signaling pathways. Production of ROS at mitochondria integrates cellular energy state, metabolite concentrations, and other upstream signaling events and has important implications in cellular stress signaling, maintenance of stem cell populations, cellular survival, and oncogenic transformation [3].

Besides, iron participates in its own homeostasis regulation in the cytosol. Iron regulatory protein 1 and 2 (IRP1 and 2) bind to the iron responsive elements (IREs) of genes that involve in iron uptake, storage and utilization to tightly control iron level. Interestingly, the activity of IRP1 and IRP2 is iron level sensitive. When iron is deficient, iron -sulfur cluster is compromised and

Apo-IRP1 (no iron-sulfur cluster) can bind to the UTR of genes like transferrin and TfR1 to uptake more iron into cells. As for IRP2, under iron limiting conditions, IRP2 is stabilized and accumulated for iron related genes regulation. In contrast, high iron level leads to the degradation of IRP2 [4-6]. Other iron-related genes like Fbxl5 and HIF1α are also found to be regulated associating with iron level [7-9]. In addition, iron in cytosol loads onto the hypoxia-inducible factor (HIF) prolyl hydroxylases (PHDs) and asparagine hydroxylases (FIH) with the help of poly(rc)-binding proteins (PCBP) for regulation of hypoxia-inducible factors [10].

As part of iron-sulfur cluster protein, iron also engages in DNA repair, DNA replication, ribosome assembly and translation initiation in nucleus and cytosol [11, 12].

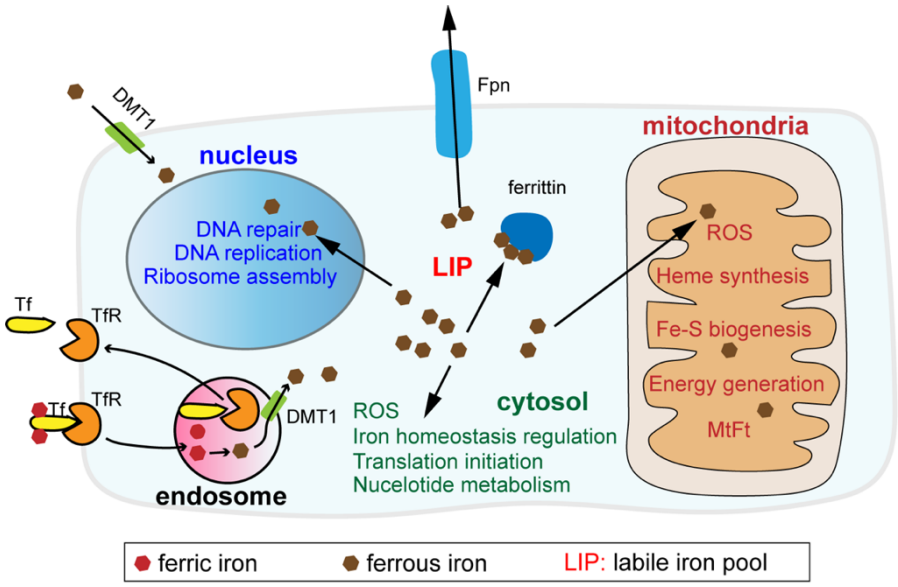

Figure 1.1 Cell biology of iron homeostasis

1.2 Iron and Adipocyte Thermogenesis

Adipose tissues are pivotal for whole-body glucose, lipid, and energy metabolism. White adipose tissue (WAT) stores caloric energy in the form of triglycerides and release fatty acids in response to fed/unfed states. In contrast, brown adipose tissue (BAT) dissipates caloric energy by

characteristic uncoupling protein 1 (Ucp1)–dependent uncoupled thermogenesis (nonshivering thermogenesis; NST) under cold stress. In rodents, Ucp1$^+$ thermogenic adipocytes (also called beige adipocytes) emerge in WAT depots upon chronic cold stress, sustained sympathetic stimulation or cancer-induced cachexia [13]. Recent studies revealed that human Ucp1$^+$ adipocytes also coexist with white adipocytes within adult human adipose tissues [14-17]. Cold exposure and β3-adrenergic receptor agonists are capable of recruiting and activating Ucp1$^+$ adipocytes in humans, which augments energy expenditure (EE), and improves glucose tolerance and insulin sensitivity [18-21]. Thus, stimulating the activation of thermogenic adipose tissues holds promise to restore energy homeostasis in obesity and ameliorate diabetic hyperglycemia.

Iron is being revealed as an essential modulator of energy metabolism, especially related to adipose tissue. Disruption of iron homeostasis leads to adipocytes dysfunction, especially the thermogenic capacity of brown and beige adipocytes. Early from 1984, studies in both humans and animals found that iron deficiency impairs the ability to maintain body temperature upon cold exposure [22-25]. Afterward, a growing number of studies have supported the impact of iron on adipocyte thermogenesis. The importance of iron is well evidenced by the detrimental consequence triggered by iron deficiency (ID) on the function of thermogenic adipose tissues.

Low iron diet-induced iron deficiency is one of the most common and direct iron deficiency models when studying iron deficiency. Yook *et al*. show that dietary iron deficiency attenuates both acute cold-induced body temperature tolerance and CL-induced adaptive thermogenesis. Specifically, the formation of beige adipocyte is decreased by iron deficiency [26]. Diet-induced iron deficiency has its shortcoming when studying tissue-specific functions of iron. TfR1 depletion in BAT is then utilized. Transferrin receptor 1 (TfR1) is one of the key iron uptake machinery in mammalian cells. TfR1 is reported to functionally mark thermogenic adipocytes [27]. Ablation of

TfR1 in adipocyte exhibits impaired thermogenesis, increased insulin resistance and mitochondrial dysfunction [28]. Except for TfR1, mice lacking transmembrane serine protease 6 (Tmprss6) develop iron deficiency in both inguinal white adipose tissue (iWAT) and iBAT and have impaired cold-induced beige adipocyte formation and brown fat thermogenesis [28]. Other iron-related proteins, such as iron regulatory proteins (IRP) 1 and 2, are also reported to be responsive to thermogenic stimulation and involved in brown and beige adipocyte differentiation [29].

Mechanistically, HIF1α and IRP proteins play pivotal roles in regulating TfR1 for iron uptake during beige formation [28, 30]. Once imported into the cell, iron in mitochondria functions in the form of Fe-S cluster to engage in various processes. Disturbance of iron homeostasis results in mitochondrial dysfunction and impaired brown and beige adipocyte differentiation [31-33]. Besides, iron-containing heme dynamics in in nuclei are found to play an import role in adipocyte thermogenesis modulation. Deletion of PGMRC2 in brown fat reduces labile heme in the nucleus and increases the stability of the heme-responsive transcriptional repressors Rev-Erbα and BACH1. Ensuing alterations in gene expression spawn severe mitochondrial defects that rendered adipose-specific PGRMC2-null mice unable to activate adaptive thermogenesis [34]. However, studies are all focusing on the engagement of iron in adaptive beige adipocyte formation. Brown adipocyte can be activated acutely in a Ucp1-dependent manner [35]. The involvement of iron in acute brown adipocyte activation is poorly depicted, and further studies are required to address the gap.

1.3 Iron and Skeletal Muscle

As a major reservoir of body iron, skeletal muscle has been an interest for studying iron metabolism and function. Skeletal muscle represents 40% of body mass and contains 10%-15%

iron [36]. There is evidence that show the critical role of iron in the optimal function of skeletal muscle tissues (**Figure 1.2**). It involves in energy metabolism as well we numerous other cellular processes. The importance of iron is evidenced by the detrimental consequence triggered by iron deficiency and iron overload on the function of skeletal muscle.

Studies reveal that iron deficiency results in skeletal muscle weakness and decreased exercise performance. The endurance and aerobic capacity are dampened after iron depletion [37, 38]. Human studies confirmed the negative effect of iron deficiency on physical performance [39-41], which can be rescued by iron supplements [42, 43].

Iron deprivation causes oxygen storage defects and mitochondrial dysfunction. Skeletal muscle is a metabolically active tissue, which contains a large number of mitochondria. Iron is known for its elemental role in mitochondria function since it is a critical component of the mitochondrial electron transport chain as well as several iron-sulfur mitochondrial enzymes and heme-containing mitochondrial enzymes. Hence iron is essential for cellular respiration and ATP production. Indeed, studies show that iron deficiency leads to mitochondrial dysfunction as well as dysregulated mitochondrial quantity and dynamics [44-49]. In addition to mitochondrial defect, iron deficiency causes an energy challenge to the cell and activates a cellular energy sensor AMPK [50, 51]. Chronic activation of AMPK down-regulates mTOR pathway to repress translation initiation and protein synthesis, further decreasing the activity of skeletal muscle [52]. In the meanwhile, AMPK increases the expression of Hexokinase and Glut4, which may contribute to energy shift toward anaerobic metabolism upon iron deficiency to maximal muscle activity [53].

All of these demonstrate the necessity of iron in skeletal muscle. However, iron overloading negatively affects skeletal muscle function. Aging is associated with muscle atrophy, also known as sarcopenia. Studies have shown that aging-associated iron overloading may be detrimental and

related to muscle atrophy [54, 55]. Consistently, other iron overloading conditions, for example, in hemodialysis patients, iron overloading is found to be associated with the detrimental effect on muscle quality [56]. Direct iron administration reduces skeletal muscle mass, myofiber size and physical activity [57, 58]. Oxidative stress that is induced by excess iron contributes to the muscle atrophy by dephosphorylation of Akt and FOXO3, further reducing the expression of muscle atrophy related atrogin-1 and muscle ring finger 1 (MuRF1) [58].

Skeletal muscle is essential for glucose clearance, and it is responsible for over 80% of glucose uptake from circulation. Defect in skeletal muscle is considered to be one of the major drives for insulin resistance. Obesity is associated with gene accumulation and imaging makers of iron in skeletal muscle [59]. Excess iron supplements can induce insulin resistance of muscle cells [60, 61]. Palmitate-induced iron accumulation mediates insulin resistance in human skeletal muscle cells [62]. Iron regulator protein, transferrin receptor (TfR1) and iron-responsive element-binding protein 2 (IRP2), induce iron accumulation and further result in insulin resistance [62]. Factors including AKT, mTORC1, JNK, autophagy and ER-stress contribute to the iron overloading induced skeletal muscle insulin resistance [60-62].

Skeletal muscle is a highly regenerative organ in the body. Skeletal muscle stem cells, also called satellite cells, are crucial for injury-induced muscle regeneration. Excess administration of iron is reported to inhibit myogenesis and dampen CTX-induced muscle regeneration in an oxidative stress-dependent way [63]. On the contrary, iron depletion by transferrin receptor 1 (TfR1) ablation in satellite cells impedes skeletal muscle regeneration through activation of ferroptosis.

Under physiological conditions, a high amount of iron stores in skeletal muscles. It is essential for skeletal muscle function. However, the homeostasis of iron is tightly controlled. Disruption of

iron homeostasis would result in muscle dysfunction, including muscle weakness, atrophy, insulin resistance as well as a failure of muscle maintenance.

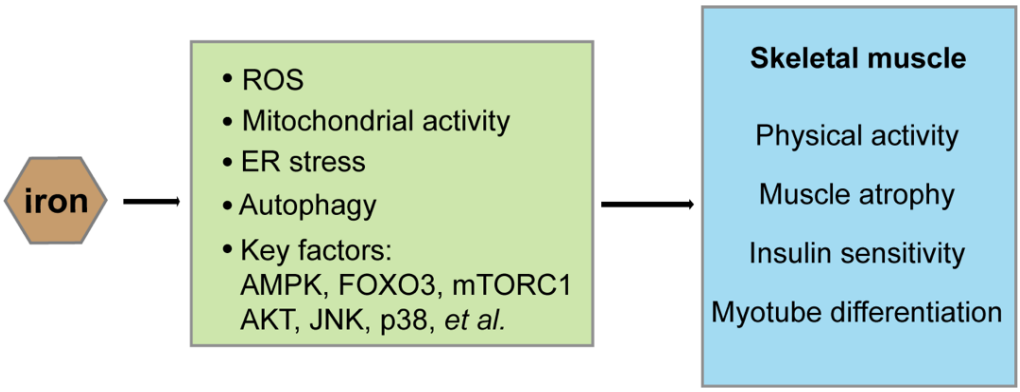

Figure 1.2 Iron and skeletal muscle function

1.4 Iron and Stem Cells

Stem cells have the unique capacity to differentiate into many cell types during embryonic development and postnatal growth. Through coordinated cellular behaviors (self-renewal, proliferation, and differentiation), stem cells are also pivotal to the homeostasis, repair, and regeneration of many adult tissues/organs and thus of great importance in regenerative medicine.

Embryonic stem cells (ESCs) have the pluripotent potential to generate all adult cell types. Adult stem cells instead are multipotent or unipotent and only give rise to limited numbers of cell types. By definition, stem cells must reproduce themselves, a process called self-renewal. Stem cell self-renewal is of great importance to the long-term maintenance of stem cell populations and the transient expansion of stem cells during development and tissue regeneration. Stem cell can self-renew through asymmetrical or symmetrical cell divisions. Through asymmetric cell division, a stem cell gives rise to a daughter stem cell and a daughter progenitor cell. The latter usually has limited lineage potential or progresses closer to the terminal differentiation. Progenitor cells can further differentiate into mature cell types. Under the homeostatic condition, stem cells keep a

delicate balance between self-renewal and differentiation through various intrinsic and extrinsic mechanisms [64]. Defects in stem cell self-renewal lead to their depletion and senescence, eventually resulting in developmental defects, failed tissue homeostasis, impaired tissue regeneration, and cancer [65, 66].

An appropriate balance between self-renewal and differentiation is crucial for stem cell function during both development and tissue homeostasis throughout life. Recent evidence suggests that iron engages in the regulation of the balance and participates in the cell fate determination of stem cells (**Figure 1.3**).

It has been reported that keeping iron at a low level of is essential for stem cell self-renewal. Extra supplemental iron inhibits the self-renewal of human pluripotent stem cells via DNA damage and reactive oxygen species (ROS) generation [67]. Fbxl5 involves in the degradation of iron regulatory protein 2 (IRP2) to repress iron uploading. Deletion of Fbxl5 in mouse hematopoietic stem cell (HSC) results in cellular iron overload, failure of self-renewal, and further exhausting of stem cell [68]. However, even low, iron is still required for the normal function of stem cells. Iron deficiency could impair the self-renewal, proliferation, differentiation as well as pluripotency of stem cells [69-72]. Long-term of iron depletion causes cell death [69].

Iron at a physiological higher level is shown to promote the proliferation rate of stem cells. Iron, at the concentrations detected in sera of iron overloaded patients, stimulates in vitro proliferation of bone marrow mesenchymal stem cells (BW-MSCs) [73]. Exogeneous iron induces the proliferation, migration and invasion of cancer stem cells [74]. Heme oxygenase 1 (HO-1) is a stress protein that catalyzes the degradation of heme into free iron. HO-1 overexpression in bone marrow mesenchymal stem cells exhibits enhanced proliferation and differentiation in the acute kidney injury microenvironment [75]. In addition, FBXL5 inactivation in neural stem progenitor

cells manifests an unexpected increased rate of proliferation [76]. All of these demonstrate the positive regulation of iron on stem cell growth.

However, the effect of iron on stem cell differentiation is complicated. Mesenchymal stromal cells (MSCs) are located in various tissues where these cells show multi-lineage differentiation, which can differentiate into osteoblasts, chondrocyte, skeletal myocyte, adipocyte. Excess iron acts differently on the different lineage. In bone marrow mesenchymal stromal cells (BM-MSCs), addition of iron in the culture medium impairs osteoblastic differentiation acting on both cell commitment and matrix classification process but promotes the adipogenic differentiation [73, 77-80]. The regulation is environment and cell-type specific.

Iron overloading, which is common in several chronic conditions and patients undergoing allogeneic stem cell transplantation, hinders the normal function of stem cells, including proliferation, differentiation and self-renewal [81-85]. Besides, abnormal accumulated iron results in apoptosis and senescence of stem cells [82, 84, 86-88].

Mechanistically, ROS is a well-known mediator of iron's effect on stem cells. Iron in mitochondria involves in ROS generation via Fenton's reaction. A physiological level of ROS is considered as secondary signaling messengers, mediating numerous cellular functions in stem cells, whereas the pathological level of ROS leads to oxidative stress and cell damage [89-91]. Redox sensor proteins (p38, ERK, AKT, NF-κb) and various other transcription factors (p27, p16, p53) that are directly or indirectly modulated by ROS are found to be crucial regulators of stem cell fate [89, 90]. Additionally, other mitochondria-related properties are highly associated with iron [92, 93]. Iron participates in mitochondrial biogenesis, mitophagy, fragmentation and fusion [92]. Emerging evidence indicates that mitochondria dynamics are actively involved in the regulation of stem cell behaviors. Mitochondria undergo specific dynamics (biogenesis, fission,

fusion, and mitophagy) during stem cell self-renewal, proliferation, and differentiation. The alteration of mitochondrial dynamics, fine-tuned by stem cell niche factors and stress signaling, has considerable impacts on stem cell behaviors [94]. Mitochondrial OXPHOS and TCA cycles are also modulated by iron homeostasis. Iron, in the Fe-S cluster or heme complex, is part of components composing complexes of electron transport chains and key enzymes in TCA cycle, which grant iron's key function in regulating mitochondrial oxidative phosphorylation (OXPHOS) and TCA cycle. Both iron deficiency and iron overload dampen the activity of mitochondrial OXPHOS [95-98]. Mitochondrial signaling, through TCA cycle generated metabolite (a-KG, acetyl CoA) and OXPHOS mediated ROS and NAD^+ production, directs the fate of stem cells via modulation of gene expression and epigenetics [99]. In addition, iron is one of the known factors that participate in the stability regulation of hypoxia-inducible protein (HIFα). A decrease in cellular iron availability inhibits PHD-dependent proline hydroxylation of HIFα subunits, resulting in the failure of von Hippel-Lindau tumor suppressor protein (VHL) binding to HIFα subunits for degradation. Hypoxia-inducible proteins HIF1α and HIF2α are known to promote self-renewal of stem cells, including mesenchymal stem cells [100], skeletal muscle stem cells [101] and cancer stem cells [102].

In summary, iron deficiency and iron loading have detrimental effect on stem cells. Whereas iron at physiological levels is pivotal for the determination of stem cell fate. Fine-tuned modulation of iron can lead to controlled stem cell function towards various biomedical applications.

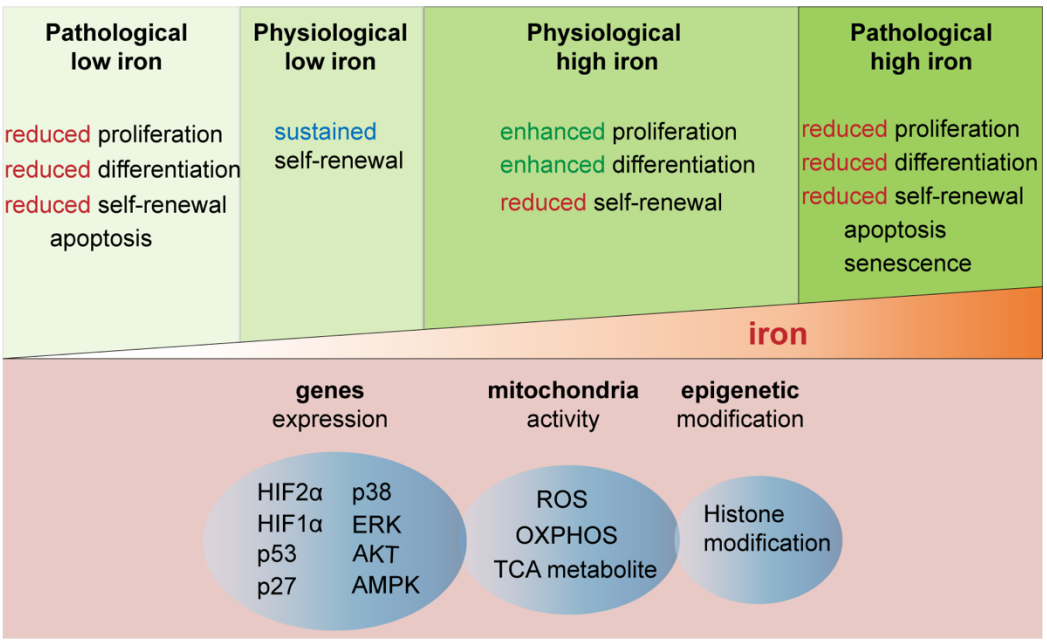

Figure 1.3 Iron effects on stem cells

CHAPTER 2

ACUTE IRON UPTAKE ACTIVATES THERMOGENESIS IN BROWN ADIPOSE TISSUE

2.1 Summary

An oxidative state in mitochondria is critical for the thermogenic activation in brown adipose tissues (BAT). Intracellular chelatable iron catalyzes the production of many oxidative radicals; however, the role of chelatable iron in BAT thermogenic activation remains unclear. Here, we report that BAT activation is concomitant with acute TfR1-mediated iron uptake and a prompt increase of iron-catalyzed mitochondrial Fenton reaction. Iron uptake is critical for the thermogenic activation of brown adipocytes as short-term blockades of iron uptake or transient iron chelation dampened uncoupling respiration. On the other hand, forced iron loading in brown adipocytes is sufficient to induce uncoupling thermogenesis without exogenous adrenergic stimuli. Interestingly, chelatable iron during thermogenic activation augments protein thiol oxidation in mitochondria yet represses oxidative stress in the cytosol. Our data indicate that chelatable iron has critical roles in activating thermogenesis in BAT, which expands the physiological functions of iron in metabolism.

2.2 Introduction

Brown adipose tissue (BAT) in mammals is specialized in UCP1-mediated uncoupling thermogenesis under cold exposure [103]. In human adults, BAT activity is sufficient to increase

energy expenditure and insulin sensitivity [14, 20, 104, 105]. Augmenting BAT activity thus represents a promising strategy to ameliorate symptoms of metabolic diseases.

UCP1 plays a critical role in uncoupling thermogenesis in BAT. In a basal (unstimulated) state, mitochondrial inner membrane (MIM)-bound UCP1 is inhibited by cytosolic ATP and does not mediate proton (H^+) conductance [106]. Upon cold exposure, increased sympathetic inputs act on β-adrenergic receptors and augment lipolysis and transcriptional activation of thermogenic genes by protein kinase A (PKA) and p38 MAPK pathways, respectively [13]. Activated p38 phosphorylates PGC1α and ATF2, both of which transcriptionally activate *Ucp1* [107, 108]. On the other hand, free long-chain fatty acid anions from lipolysis bind UCP1 and carry H^+ across MIM [109]. Besides PKA and p38 pathways, mitochondrial reactive oxygen species (ROS) induce an oxidative state of BAT mitochondria, which is crucial for acute BAT thermogenic activation. Treatment of chemical anti-oxidants (e.g., NAC and MitoQ) or overexpression of a ROS-scavenging protein Sestrin2 represses BAT uncoupling [110, 111]. Conversely, increasing ROS production from ETC (by succinate treatment) or ablating mitochondrial superoxide dismutase (MnSOD/SOD2) leads to augmented BAT thermogenesis and protection from diet-induced obesity [112, 113]. Mechanistically, ROS oxidize cysteine thiol groups on UCP1 and sensitize its H^+ conductivity [110]. Thus, a ROS-mediated oxidative state is obligatory to BAT activation [114]. Yet, the roles and relative contributions of ROS in support of thermogenic activation are not fully understood.

Intracellular chelatable iron catalyzes the production of hydroxyl radicals (•OH) from ETC-originated superoxides (O_2^-) and hydrogen peroxides (H_2O_2) via Haber-Weiss/Fenton reactions [115]. Hydroxyl radicals promiscuously oxidize almost all types of adjacent macromolecules. In particular, •OH can react with unsaturated fatty acids and initiate a cascade of lipid peroxidation

chain reactions, which propagates on cellular membrane structures, and results in the production of reactive aldehydes, such as malondialdehyde and 4-hydroxynonenal (HNE) [116]. Lipid peroxides and reactive aldehydes are major contributors of oxidative stress and are harmful to the viability of cells. However, it has been reported that 4-HNE paradoxically supports uncoupling thermogenesis [117, 118]. Thus, an intriguing question is whether chelatable iron plays a role in BAT thermogenic activation.

Here, we provide the first evidence that the acute accumulation of chelatable iron in brown adipocyte mitochondria is crucial for BAT thermogenic activation. Thermogenic activation was abolished by blocking iron uptake, dampening Fenton reaction by chelating Fe^{2+}, neutralizing hydroxyl radicals, or diminishing membrane lipid peroxidation. On the other hand, forced iron loading either in intact brown adipocytes by holo-ferritin nanocage or in permeabilized brown adipocytes by FAC treatment is sufficient to induce uncoupling thermogenesis without exogeneous adrenergic stimuli. Besides activating uncoupling thermogenesis in mitochondria, chelatable iron also protects against oxidative stress in the cytosol of brown adipocytes. This study elucidates new physiological roles of chelatable iron in uncoupling thermogenesis and may also sheds more light on the relationship of iron and oxidative stress in metabolic active tissues.

2.3 Materials and Methods

Animal studies

All animal studies were approved by the University of Georgia Institutional Animal Care and Use Committee (IACUC) and performed following the guidelines. Animals were raised in a temperature-controlled (22°C) environment with 12:12-hrs light:dark cycle and allowed food and water *ad lithium*. All mouse strains were purchased from the Jackson Laboratory: *C57BL/6J* (JAX:

000664), *Ucp1*^{Cre} (JAX: 024670), *Tfrc*^{flox} (JAX: 028363). For the generation of mild iron deficient mouse models, *C57BL/6J* mice (5-wk old) were fed with iron-sufficient (IS) diet (35 ppm, Dyets #115127) or iron deficient (ID) diet (3 ppm, Dyets #115072) for 8 weeks. Blood hemoglobin levels were measured after 6-8 weeks of feeding by HemoCue Hb^{201+} Hemoglobin analyzer (HemoCue). For induced BAT activation, CL316,243 (1 mg kg^{-1} body weight) was administrated by intraperitoneal (i.p.) injection. For cold exposure assays, mice were housed at either 22°C or 30°C and then exposed to 16°C for the stated time. For cold tolerance assays, mice raised under 22°C were acutely exposed to 4°C for 4 hrs, during which rectal temperatures were measured every 20 mins using a thermometer (MicroTherma 2) equipped with a rectal probe (RET-3).

In vivo compound administration

Male *C57BL/6J* mice (~12 weeks old; body weight between 25-28 g) were utilized for BAT local compound administration. Ketoprofen (1mg kg^{-1} body weight) were injected subcutaneously (s.c.) before surgery. Mice were under isoflurane-oxygen anesthesia during the surgical procedure. An incision (about 1 cm) was made on the dorsal skin (clipped/sterilized) to expose interscapular BAT (iBAT). Various compounds were injected into iBAT using Hamilton syringes (700 series, 10 μL, Hamilton). 0.25 mg 2,2′-bipyridyl (BPD, Sigma Aldrich) in 16 μL 10% DMSO/saline or 0.1 mg gambogic acid (Fisher Scientific) in 16 μL 10% DMSO/saline was injected into each mouse. 10% DMSO/saline vehicle solution was injected at the same volume and served as control.

Cell cultures

Primary adipose stromal vascular fractions (SVFs) were isolated from *C57BL/6J* (JAX: 000664) mice. Briefly, BAT and WAT were dissected, washed in PBS, minced, and digested with 1.5 mg mL^{-1} type II collagenase (Worthington) in isolation buffer (123 mM NaCl, 5 mM KCl, 1.3 mM $CaCl_2$, 5 mM glucose, 100 mM HEPES, and 4% fatty-acid-free BSA) for 30 ~ 45 min at 37 °C.

Tissue suspension was filtered through a 100 μm filter and centrifuged at 800 *g* for 5 min to pellet SVFs. The cell pellet was resuspended in growth medium (DMEM containing 20% FBS and 1% penicillin/streptomycin) and plated in collagen coated cell culture plates. Cells were cultured at 37 °C with 5 % CO_2. Upon confluence, SVFs were induced adipogenic differentiation as following description: For isoproterenol (ISO, 10 μM), 2,2'-bipyridyl (BPD, 200 μM), and gambogic acid (GA, 0.5 μM) treatment, to maintain brown adipocytes at an unstimulated status, BAT SVFs were induced with induction medium (DMEM containing 10% FBS, 0.5 mM isobutylmethylxanthine/IBMX, 125 mM indomethacin, 2 mg mL^{-1} dexamethasone, 850 nM insulin and 1% penicillin/streptomycin) for 2 days, and differentiated in differentiation medium (DMEM containing 10% FBS, 850 nM insulin and 1% penicillin/streptomycin) for 1.5 days. 3T3-L1 preadipocytes were cultured and differentiated following the protocol provided by ATCC. At the end of differentiation, cells were treated with compounds at stated dosage and time, then collected for assays.

Ferrozine assay

For tissues, 10 ~ 20 mg mouse tissues were excised and homogenized in ~300 μL high purity molecular biological (MB) grade water (OMNI Bead Ruptor 24 Elite). An equal volume of extraction buffer (1M HCl and 10% trichloroacetic acid in MB water) was added to each homogenized sample. For cell cultures, ~300 μL cell lysate (0.5 ~ 1 x 10^6 cells) was mixed with equal volume of extraction buffer. For mitochondrial fraction isolation, after extraction, pelleted mitochondria were resuspended with ~200 μL higher purity water and mixed with equal volume of extraction buffer for assay. For cytosolic fraction isolation, cytosol was mixed with an equal volume of extraction buffer for assay. Samples with extraction buffer were thoroughly mixed by vortex and incubated at 98°C for 1 hr. After incubation, the samples were cooled down at room

temperature (RT, 22°C) for 20 min, and then centrifuged at 16,000 *g* for 10 min at RT. Supernatants were transferred into new 1.5 mL tubes and aliquoted 50 μL to each well on a 96-well plate. Each aliquot was incubated with 50 μL reaction buffer (0.5 mM ferrozine, 1.5 M sodium acetate, 1.5% v/v mercaptoacetic acid) at 37°C for 1 hr. 562 nm absorbance was measured by microplate reader (BioTek). Serial ferric ammonium citrate (FAC) dilutions were processed with the same procedures as above and served as standards.

In vivo fluorescent imaging of IRDye800-labeled transferrin

To label transferrin with IRDye800, 0.5 mL of 0.8 mg mL^{-1} mouse apo-transferrin (apo-Tf; Sigma-Aldrich) in PBS was mixed with 30 μL IRDye800 CW-NHS ester (1 mg mL^{-1} in DMSO, Ex/Em = 780/800 nm, LI-COR) for 1 hr at room temperature. The mixture was purified on a NAP-5 column. The concentration of the resulting apo-Tf-IRDye800 was determined by Bradford protein assay. For in vivo imaging, 10 female BALB/c nude mice were randomly sorted into 2 groups (n = 5) and i.p. injected with CL316,243 (CL, 1 mg kg^{-1} in 100 μL saline) or saline (100 μL). For both groups, apo-Tf-IRDye800 (0.8 mg kg^{-1} body weight) was i.v. injected 30 min after the CL/saline injection and were subjected to full-body fluorescence imaging at 1 and 2 hrs on a Maestro II imaging system (PerkinElmer) using NIR emission filter (750-940 nm). All acquired images were unmixed against the library, which was built with a nude mouse s.c. injected with Tf-IRDye800. Region of interest (ROI) analysis was done on both in vivo and ex vivo imaging results with vendor-provided software.

Thermographic imaging

3-day postnatal wild-type and $Ucp1^{Cre};Tfrc^{f/f}$ pups were kept in thermoneutrality (30°C) for 2 hrs and then exposed to room temperature (RT, 22°C) for 30 min. Thermographic images were captured by FLIR ONE camera (FLIR Systems).

Membrane protein extraction

BAT was homogenized in membrane isolation buffer (0.25 M sucrose, 1 mM EDTA, 10 mM Tris-HCL, pH 7.4) with Teflon Potter Elvehjem homogenizer. The homogenate was centrifuged at 20,000 *g* for 15 min at 4°C. The pellet was resuspended, centrifuged at 1,000 *g* for 10 min at 4 °C, and the supernatant was then centrifuged at 21,000 *g* for 20 min at 4 °C. The pellet was resuspended and centrifuged at 58,000 *g* for 30 min at 4 °C on sucrose gradient (1 ~ 1.5 M sucrose in 5 mM Tris-HCL, pH 7.4, 1 mM EDTA). The plasma membrane containing band was collected and pelleted by centrifugation at 21,000 *g* for 30 min at 4°C.

Polysome fractionation

For analysis of BAT polysomes, ~ 50 mg BAT was homogenized in liquid nitrogen and lysed in ice-cold polysome lysis buffer (140 mM KCl, 1.5 mM $MgCl_2$, 20 mM Tris-HCl, pH 7.4, 0.5% Nonidet P-40, 0.5 mM dithiothreitol, 1,000 U mL^{-1} RNase inhibitor, 1x EDTA-free protease inhibitor, 150 mg mL^{-1} cycloheximide). The lysate was centrifuged for 10 min at 10,000 *g* to remove debris. The supernatant was loaded on the top of a 20% to 47% sucrose gradient (20 mM Tris-HCL, pH 7.4, 140 mM KCl, 5 mM $MgCl_2$). The Polysomal fractions were isolated after ultracentrifugation (40,000 rpm, 3 hrs at 4°C) with Beckman SW-41 rotor. RNA in the polysomal fractions was isolated by phenol-chloroform extraction.

Quantitative real-time PCR

Total RNA was isolated from tissue or cell culture using TRIzol reagent (Thermo Fisher Scientific). 500 ng total RNA was reverse-transcripted into cDNA in 25 µL reverse transcription reactions (Maxima; Life technologies) and diluted into 250 µL. 2 µL diluted cDNA was used in an 8 µL quantitative PCR reaction (SsoAdvanced™ Universal SYBR Green mix; Bio-Rad) on a BioRad CFX384™ Real-Time PCR Detection System. Cq-values were determined and expression

values were calculated by BioRad CFX Manager™ Software. Relative expression values were normalized to inner reference genes *Rps18* and *Tbp* of each biological sample. To measure mitochondrial DNA copy number, total genomic DNA was isolated from cells by phenol/chloroform extraction and RNA removal (RNase A). Mitochondrial DNA (*Cox2*) copy numbers were detected and normalized by total genomic DNA content (*Globin*).

Protein extraction and immunoblotting

Tissues or whole cell lysates were prepared by homogenization in RIPA buffer supplemented with 1x proteinase inhibitor cocktail (Amresco). Protein concentration was quantified by BCA assays (Thermo Fisher Scientific). Protein lysates were loaded on 10% SDS-PAGE, transferred to PVDF membranes. The membranes were blocked with 5% non-fat milk/TBST, probed with primary antibodies at 4°C overnight. After secondary antibodies incubation, membranes were treated with ECL reagents (ThermoFisher Scientific) and exposed to X-ray films (Santa Cruz).

Histological analysis

For histological analysis, BAT was excised and fixed with 10% formalin, dehydrated and embedded in paraffin. The sliced tissue (5 μm) was stained with Hematoxylin (Sigma Aldrich) and Eosin Y (Sigma Aldrich). Images were captured by a light microscope (Leica, DM4000B) equipped with a color camera (DFC420).

Preparation and characterization of Fe-loaded ferritin nanocage (HFn)

Recombinant apo-ferritin (heavy-chain only) was prepared following a published protocol (Zhen, Z., et al., Protein Nanocage Mediated Fibroblast-Activation Protein Targeted Photoimmunotherapy. To Enhance Cytotoxic T Cell Infiltration and Tumor Control. Nano Lett, 2017. 17(2): p. 862-869). Holo-Ferritin was prepared following a modified protocol (Uchida M., Q.S., Edwards E., Douglas T., Use of Protein Cages as a Template for Confined Synthesis of

Inorganic and Organic Nanoparticles, in Protein Cages, O. B., Editor. 2015, Humana Press: New York, NY. p. 17-25.). Briefly, 5 mg of apo-ferritin was dissolved in 10 mL of AMPSO buffer (50 mM, pH 8.5). The resulting protein solution was degassed and kept under Argon protection prior to iron loading. An ammonium iron (II) sulfate hexahydrate (12.5 mM) solution and a hydrogen peroxide (4.17 mM) solution were freshly prepared with degassed deionized H_2O and maintained under Ar protection. Two disposable syringes were loaded with the $(NH4)_2Fe(SO_4)_2$ and H_2O_2 solutions and inserted into a syringe pump. The two solutions were simultaneously added by the pump at a rate of 79 μL min^{-1} into the aforementioned ferritin solution. The reaction was kept at 65 °C under gentle stirring and Ar protection. The pH was checked frequently and maintained at around 8.5 with 1 M NaOH. The injection of both solutions was stopped at 3951 μL. The reaction was considered completed after another 5 min. 200 μL of 300 mM sodium citrate solution was added to the completed reaction to chelate any free iron. The product was purified, and the buffer exchanged to 0.9% NaCl (saline) on a centrifugal filter unit (MWCO=100 K).

Seahorse assays for intact cells

Brown adipose SVFs were plated and differentiated on Seahorse XFe24 cell culture microplates under conditions described above. Before Seahorse assays, culture media were changed to Seahorse XF Base Medium supplemented with 2 mM L-glutamine, 1 mM sodium pyruvate and 4.5 g L^{-1} glucose. Cells were placed in a non-CO_2 incubator for 1 hr prior to assay. For BPD and GA treatment, cells were pre-treated with BPD (200 μM), GA (0.5 μM) or vehicle diluted in complete Seahorse Base Medium for 30 min before runs. For holo-HFn and apo-HFn treatment, cells were pre-treated with holo-HFn or apo-HFn (protein concentration = 55 μg/mL), or PBS diluted in culture medium for 1 hr and in complete Seahorse Base Medium for additional 1 hr before runs. To induce acute thermogenic activation, ISO (10 μM) or diamide (200 μM) was

injected into wells by Seahorse analyzer. Oxygen consumption rates (OCR) were measured via the mitochondrial stress test assay (Agilent, 103015-100) following the manufacturer's protocols. Data was processed via Wave software (Agilent).

Seahorse assays for permeabilized cells

To directly access mitochondrial function, brown adipocytes were differentiated on Seahorse XFe24 cell culture microplates and pretreated with BPD (200 μM) for 30 min. Before Seahorse assays, the media was changed to mitochondria assay medium (MAS; 220 mM mannitol, 70 mM sucrose, 10 mM KH_2PO_4, 5 mM $MgCl_2$, 2 mM HEPES, 1 mM EGTA, 0.2 % fatty acid free BSA, pH 7.2) supplemented with 5 mM glutamate, 5 mM malate, and 3 nM PMP.

High-resolution respirometry of permeabilized iBAT

High-resolution respirometry measurement was performed on the Oroboros O2k respirometer (Oroboros Instruments, Innsbruck, Austria). An air saturated calibration was performed on each oxygen sensor prior to starting any respiration measurements. Zero oxygen and instrumental background tests were performed monthly. During respiration measurements, the oxygen concentration was maintained between 200-450 μM O_2 by re-diffusing O_2 into the respiration buffer when O_2 levels neared 200 μM. All respiration experiments were performed at 25°C to slow mitochondrial respiration rates and minimize the number of oxygen infusions needed during each test. All respiration experiments were performed in a respiration buffer (pH 7.1) containing k-MES (105 mM), KCl (30 mM), KH_2PO_4 (10 mM), $MgCl_2$-$6H_2O$ (5 mM), BSA (0.5 mg ml^{-1}), EGTA (1mM). BAT was harvested immediately after sacrifice and dissected into <1 mg strips. BAT samples (~2 mg) were loaded into each chamber of the O2k containing respiration buffer (2 mL) and 2 μM digitonin to permeabilize the outer plasma membrane of the BAT (Kraunsoe et al. 2010). All mitochondrial respiration rates were expressed relative to mg of BAT loaded into the chamber.

Three separate substrate/inhibitor sequences were used to measure mitochondrial respiration. Sequence 1 was used to determine the contribution of ATP synthase activity to the mitochondrial respiration rates. First, glutamate (10 mM), malate (2 mM), succinate (10 mM) were added to induce leak respiration (state 2), followed by ADP (5 mM) to stimulate ATP-synthase supported (state 3) respiration state. Sequence 2 was used to determine the effect of Fenton reaction derived ROS on UCP1 function. Leak respiration was initiated with glutamate (10 mM), malate (2 mM), and succinate (10 mM), followed by serial titrations of ATP (25 mM, 37.5 mM, 50 mM) to inhibit UCP1. Ferric ammonium citrate (FAC; 2 mM) was then added to stimulate the Fenton reaction and subsequent production of ROS. Cyanide, an inhibitor of cytochrome C oxidase (complex IV) was added last to completely block all mitochondrial respiration. Sequence 3 was used to elucidate whether hydroxyl radicals activated UCP1 and caused an increase in respiration following the addition of FAC in sequence 2. Sequence 3 mirrored sequence 2 through the addition of FAC. Then, nicaraven (0.5 mM), a potent hydroxyl radical scavenger was added to block the effects of FAC on UCP1 function. Alternatively, U-74389G (1 mM), a potent membrane lipid peroxidation inhibitor, was added in sequence 3 after FAC treatment. Sequence 4 (sequence 2 without the addition of succinate) was used to determine the requirement of succinate-induced mitochondrial ROS in the thermogenic effect of FAC.

Indirect calorimetry

Mice were individually housed in metabolic chambers in an environmental chamber with adjustable temperature (4-35°C) for 5-7 days before indirect calorimetry measurements. Oxygen consumption (VO_2), carbon dioxide production (VCO_2), respiratory exchange ratios (VCO_2/VO_2) and heat production were measured using an indirect calorimetry system

(Oxymax, Columbus Instruments) with a 12-hr light, 12-hr dark cycles. Mice in each chamber had free access to food and water.

RPA assay to detect mitochondria Fe^{2+}

Cell culture medium was removed, and cells were washed with PBS and then were incubated with 2 μM RPA (Axxora) in HBSS for 20 min at 37°C with 5% CO_2. Cells were then washed twice with HBSS and incubated for another 20 min in HBSS. The intra-mitochondrial RPA signal was determined by fluorescence intensity measurement at Ex/Em = 540/600 nm.

MitoROS™ OH580 assay to detect mitochondria hydroxyl radicals

The MitoROS™ OH580 staining was conducted following manufacturer's instructions. Briefly, cells were washed with PBS and were incubated with 100 μL MitoROS™ OH580 (AAT Bioquest) working solution per well (96-well plate) at 37°C with 5% CO_2 for 30 min. After washing twice with PBS, the assay buffer was loaded into each well and fluorescence intensity was measured at Ex/Em = 540/590 nm.

H_2DCFDA assay to detect reactive oxygen species (ROS)

Cell culture medium were removed and cells were washed with PBS. Then, cells were incubated with 20 μM H_2DCFDA in reaction buffer (4.5 g L-1 glucose, 2 mM glutamine in PBS) for 30 min at 37°C with 5% CO_2. Cells were then wash twice with PBS. The signal was determined by fluorescence intensity measurement at Ex/Em = 495/530 nM.

BAT lipid hydroperoxides assay

Lipid hydroperoxide (LPO) assay was conducted according to kit manual instruction (Cayman). Briefly, 10 mg fresh-excised BAT was homogenized in 300 μL RIPA lysis buffer (Amresco), followed with 20 min sonication. Dilute 30 μL homogenized sample with 470 μL RIPA buffer, and then mixed with 500 μL extraction buffer (Extract R saturated methanol) in glass test tube.

Add 1 mL cold chloroform (4°C) to each tube and mix thoroughly with 20 min agitation at room temperature (22°C). After centrifugation (1,500 *g* for 5 minutes at 4°C), the bottom chloroform layer was collected carefully. Aliquot 500 μL bottom chloroform layer samples into new tubes, add 450 μL chloroform-methanol solvent in each tube and mix with 50 μL Chromogen reaction buffer. Keep assay tubes at room temperature for 5 min. Aliquot 300 μL samples into each well (96-well plate) and measured the absorbance at 500 nm.

Calcein AM assay to detect intracellular chelatable iron

Cell culture medium was removed, and cells were washed by PBS and then incubated with 0.25 μM Calcein AM (Life technologies) in reaction buffer (4.5 g L^{-1} glucose, 2 mM glutamine in PBS) for 30 min at 37°C with 5% CO_2. Then cells were washed twice and incubated in PBS for fluorescence intensity measurement at Ex/Em = 495/530 nm.

Free thiol detection

Free thiol groups were measured with Thiol Detection Assay Kit (Cayman) according to the manual instruction. Briefly, ~50 mg iBAT was collected from each mouse with different treatment. Cellular fractions were collected as described above and suspended in 10 mM Tris-HCl (pH 8.0). 50 μL sample lysate was incubated with 50 μL thiol group detection reagent for 5 min at room temperature. Fluorescence was measured at 385/515 nm.

ATP detection

ATP levels in brown adipocytes were measured with ATP Detection kit (Cayman) according to the manual instruction. Briefly, brown adipocytes were washed with pre-chilled PBS and collected in assay buffer after treatments. Cells were homogenized in the assay buffer. In the process of reaction, add 100 μL reaction mixture and 10 μL diluted sample to wells on the plate. Incubate the plate at room temperature for 15 min and read the luminescence.

Cell viability assay

Cells were stained with ReadyProbe Cell viability imaging kit (Green and Blue, Thermo Fisher Scientific) under the guidance of manual instruction. Briefly, add 2 drops of NucGreen® Dead reagent and 2 drops of NucBlue® Live reagent per mL cell culture medium and incubate for 20 min at 37°C with 5% CO_2. Fluorescence images were captured by EVOS fluorescence microscope (FITC/GFP filter for dead cells and DAPI filter for live cells).

RNA-seq and data analysis

RNA samples were polyA selected and generated into libraries using TruSeq Standard mRNA Library Prep Kits. DNA libraries (thermoneutrality vs. CL316,243 2-hrs) were sequenced on Illumina HiSeq 4000. RNA-seq raw data were mapped to GRCm38 mouse genome and analyzed by HISAT2. Differential expression was called by edgeR. For GO term analysis, differentially-expressed genes (1,328 genes) were analyzed by WebGestalt.

Quantification and statistical analysis

All values in the figures represent mean ± s.e.m. with >= 3 biological replicates. Statistical significance was determined by GraphPad Prism 6. Two tailed Student's *t*-tests were used to compare significance between two groups after normality tests. One-way ANOVA with Bonferroni's *post-hoc* tests were performed for multiple comparison. *: $p<0.05$, **: $p<0.01$, N.S.: not significant.

2.4 Results

Acute thermogenic activation induces iron uptake in BAT

To better understand molecular mechanisms underlying the acute thermogenesis in BAT, we first examined the transcriptomic changes in BAT transiting from thermoneutrality to an early

activated state. Interscapular BAT (iBAT) samples were pooled from adult *C57BL/6* mice that were housed under thermoneutrality (T.N.; 30°C, for 3 days) and later injected (i.p.) with β_3-adrenergic receptor agonist CL316,243 (CL) or vehicle for 2 hrs. RNA-seq and comparative transcriptomic analysis identified 1,123 up- and 205 down-regulated genes in 2-hr CL-activated BAT. Expectedly, CL increased mRNA levels of BAT activation markers *Pgc1α*, *Ucp1*, *Elovl3*, and *Dio2* (**Figure 2.1A**). Gene Set Enrichment Analysis of 1,328 differentially-expressed genes revealed 581 significantly-enriched gene ontology (GO) terms (FDR<0.05). In line with adrenergic activation of BAT, GO terms "brown fat cell differentiation" and "response to cAMP" were enriched (**Figure 2.1B**). "Cellular responses to oxidative stress" (GO:0034599) and other oxidative stress-related GOs (GO:1902882, GO:1902175, GO:0036473, GO:1900407, GO:0008631, GO:1902176, GO:1900408, GO:1900409) were among the most enriched GO terms in the list, consistent with the occurrence of oxidative stress during early BAT activation (Figure 2.1B) [110, 112, 119]. Intriguingly, "cellular iron ion homeostasis" (GO:0006879) is also enriched in CL-treated BAT, implicating altered iron metabolism during acute thermogenic activation (**Figure 2.1B**).

To reveal changes of iron in BAT activation, we first measured non-heme iron levels of multiple tissues during a time course of BAT activation using ferrozine-based assays. Under the inactivated state (30°C, 3 days), non-heme iron content of iBAT was ~70% of liver and ~28% of spleen but was higher than the small intestine, skeletal muscle and WATs (**Figure 2.1C**). CL-induced activation was concomitant with an acute iron redistribution in 1-2 hrs: iron accumulated in activated iBAT, reduced in liver and spleen, and maintained at the same levels in muscle and WATs (**Figure 2.1C**). Cold exposure similarly induced iron accumulation in iBAT (**Figure S2.1A**). To exclude increased blood perfusion in activated iBAT as a possible confounding factor

for iron content measurements, we performed ferrozine-based assays using cultured brown and white adipocytes with or without adrenergic stimulations. After isoproterenol (ISO) treatment for 2 hrs, non-heme iron increased (~1.9 fold) in primary brown adipocytes (BA; **Figure 2.1D**), but not in primary white adipocytes or 3T3-L1 white adipocytes (**Figure 2.1E**, **S2.1B**), confirming acute iron uptake in activated brown adipocytes.

Transferrin receptors (TfR1, TfR2) and divalent metal transporter 1 (DMT1) are key iron-uptake machineries in mammalian cells [120]. *Tfrc* (encoding TfR1) mRNA increased, *Tfr2* mRNA decreased and *Dmt1* mRNA remained unchanged during CL-induced BAT activation (**Figure 2.1F**). Similar to UCP1, TfR1 increased in iBAT after CL-induced activation (**Figure 2.1G**). The increase of *Tfrc* mRNA at 1 hr preceded TfR1 protein increase at 2 hrs, suggesting acute TfR1 translation. Indeed, *Tfrc* mRNA increased in polysome fractions of BAT (~6.5 folds) after 2-hr CL-treatment (**Figure S2.1C**), and TfR1 receptor increased in plasma membrane fractions of iBAT (**Figure S2.1D**). To confirm that acutely-activated iBAT has augmented Transferrin (Tf) binding capacity (due to TfR1 increase), we injected (i.v.) IRDye800-labeled Tf and monitored in vivo distribution of Tf by live-animal imaging. The retention of Tf in iBAT increased (~4.3 fold) at 1 hr after CL-treatment, comparing to the saline-injected control (**Figure 2.1H**).

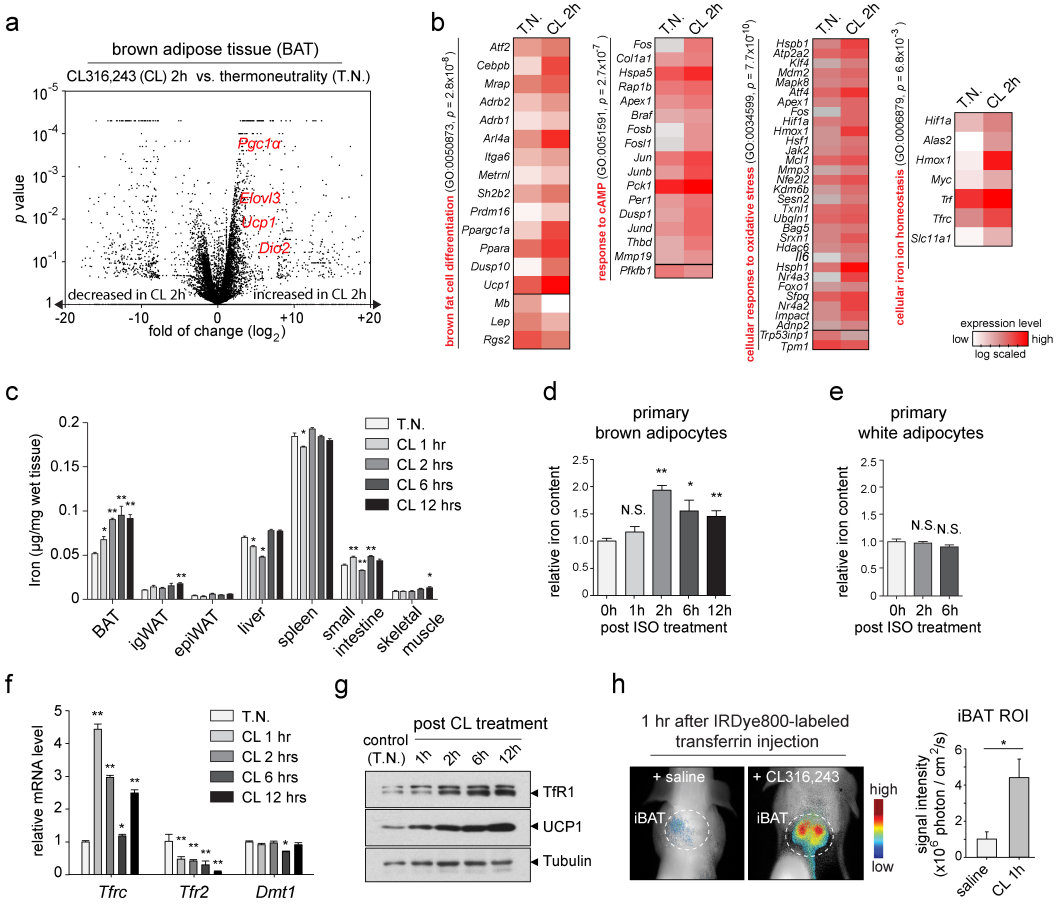

Figure 2.1. Acute thermogenic activation induces iron uptake in BAT

A. A volcano plot showing RNA-seq results of iBAT under T.N. and acute sympathetic activation (CL, 2 hrs). Known thermogenic genes (red) were increased during activation.

B. Heat maps of genes associated with selected significant GO terms from GSEA analysis.

C. Ferrozine assay showing chelatable iron contents in multiple tissues after sympathetic activation by CL316,243 (CL; n=3).

D. Chelatable iron contents of cultured primary brown adipocytes activated by isoproterenol (ISO).

E. Chelatable iron contents of cultured primary white adipocytes activated by isoproterenol (ISO).

F. RT-qPCR of iron uptake-related genes in CL-activated iBAT (n=3).

G. Immunoblot (IB) of TfR1 and UCP1 in CL-activated iBAT.

H. Left: representative in vivo fluorescence images showing the accumulation of IRDye800-labeled transferrin at the iBAT region (circled) at 1 hr after CL-activation. Right: fluorescence signal intensities in circled iBAT ROIs.

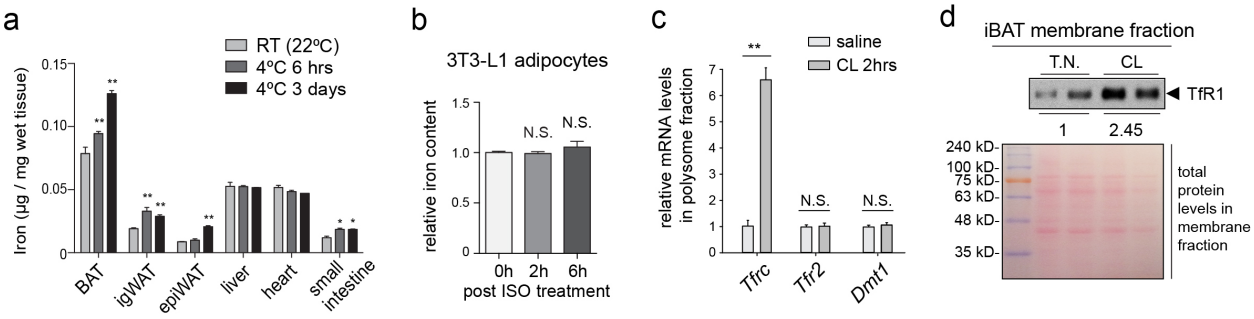

Figure S2.1. Supplementary_ Acute thermogenic activation induces iron uptake in BAT

A. Chelatable iron contents in multiple tissues after cold exposure (n=3).

B. Chelatable iron contents in cultured 3T3-L1 adipocytes before and after ISO stimulation.

C. RT-qPCR showing the enrichment of *Tfrc* mRNA (but not *Tfr2* or *Dmt1*) in polysome fractions of CL-stimulated iBAT (n=3).

D. Upper: TfR1 IB showing a 2.45-fold increase in iBAT membrane fraction after CL activation. Lower: The Ponceau S staining of the PVDF membrane before IB showing equal loading.

Genetic ablation of TfR1 in BAT abolishes thermogenic activation in newborn mice

Next, we investigated whether TfR1 is essential for BAT activation. TfR1 has ubiquitous expression in many types of cells and homozygous TfR1 null mutations are embryonic lethal [121]. To avoid confounding indirect effects from non-BAT tissues, we generated *Ucp1-Cre;Tfrc*$^{f/f}$ (BAT-TfrcKO) mice to ablate TfR1 specifically in UCP1^{+pos} brown adipocytes. At birth, BAT-TfrcKO and control pups had comparable TfR1 and UCP1 protein expression in iBAT (**Figure**

2.2A). Also, both types of newborn pups had the same mRNA levels of *Tfrc*, BAT lineage markers (*Ebf2*, *Prdm16*, *Pgc1β, Cidea, Cox8b*), BAT activation markers (*Pgc1α*, *Ucp1*, *Dio2*, *Elovl3*), and adipose lineage markers (*Pparg2*, *Fabp4*, *Lep*; **Figure 2.2B**), suggesting normal prenatal development of iBAT in BAT-TfrcKO mice. UCP1-dependent thermogenesis in BAT is critical for newborns to maintain body temperature under cold exposure. TfR1-ablation in brown adipocytes (driven by *Ucp1-Cre*) occurred within 3 days postnatally (3 dpn) and led to lower TfR1 and UCP1 protein levels in iBAT (**Figure 2.2C**). Non-heme iron in iBAT increased in control pups from birth to 3 dpn (115%), whereas remained unchanged in BAT-TfrcKO pups (**Figure 2.2D**), suggesting TfR1-ablation impeded iron uptake in BAT during activation after birth. The blockade of iron uptake within postnatal 3 days neither altered the size or morphology of iBAT tissue (**Figure S2.2A**) nor affected systemic iron and glucose homeostasis in BAT-TfrcKO pups as evidenced by comparable liver iron contents and blood glucose levels in mutant and control pups (**Figure S2.2B-C**). However, thermographic imaging revealed that BAT-TfrcKO pups (at 3 dpn) had lower body surface temperature (~0.7°C) when exposed to the room air (22°C; **Figure 2.2E**), consistent with the reduced UCP1 expression in iBAT. Additionally, genes that have increased expression during BAT activation were lower in iBAT of BAT-TfrcKO pups (at 3 dpn), whereas BAT lineage markers remained unchanged (**Figure 2.2F**). Thus, TfR1 is essential for the thermogenic activation of BAT in newborn mice.

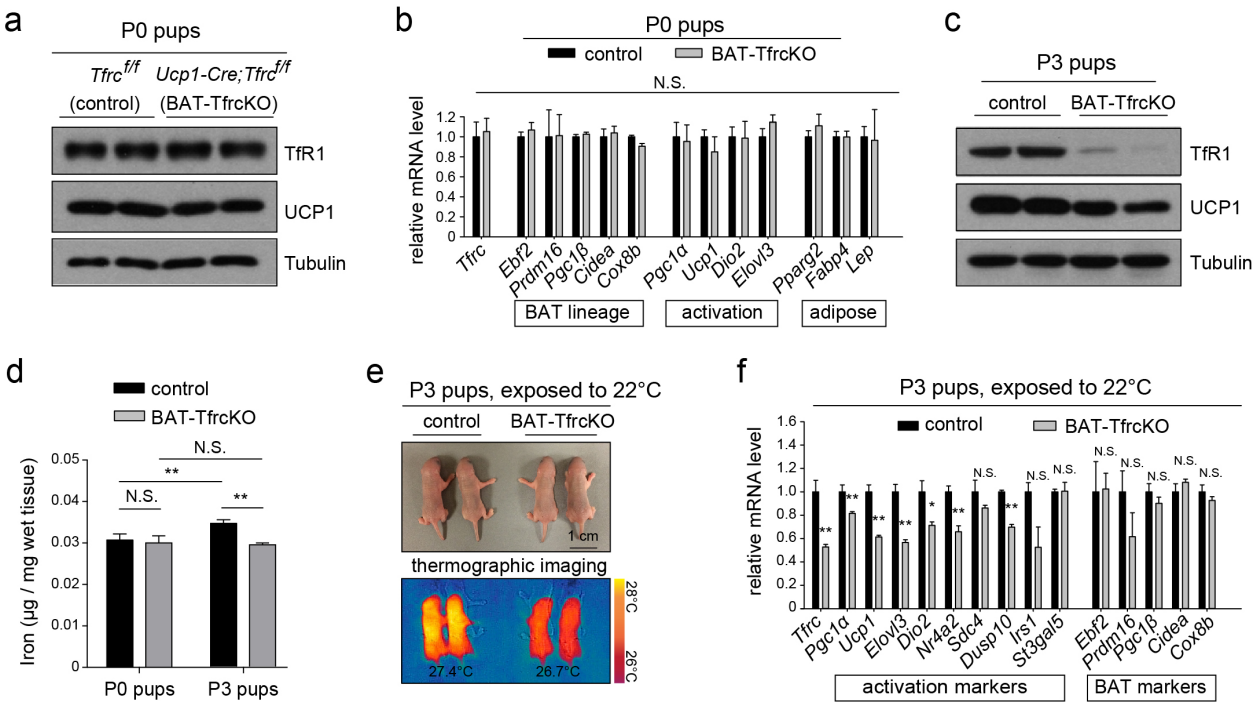

Figure 2.2. Genetic ablation of TfR1 in BAT abolishes thermogenic activation in newborn mice

A. IB showing comparable TfR1 and UCP1 levels in iBAT of BAT-TfrcKO and control pups at birth (P0).

B. RT-qPCR of BAT lineage-, activation-, and adipose-specific markers in above P0 pups (n=3).

C. IB showing reduced TfR1 and UCP1 levels in iBAT of BAT-TfrcKO pups at 3 dpn (P3).

D. iBAT iron contents of BAT-TfrcKO and control pups at P0 (n=4) and P3 (n=3).

E. Regular and thermographic images of BAT-TfrcKO and control pups (P3) under 22°C.

F. RT-qPCR showing reduced BAT activation markers yet virtually unchanged BAT lineage markers in iBAT of BAT-TfrcKO P3 pups (n=3).

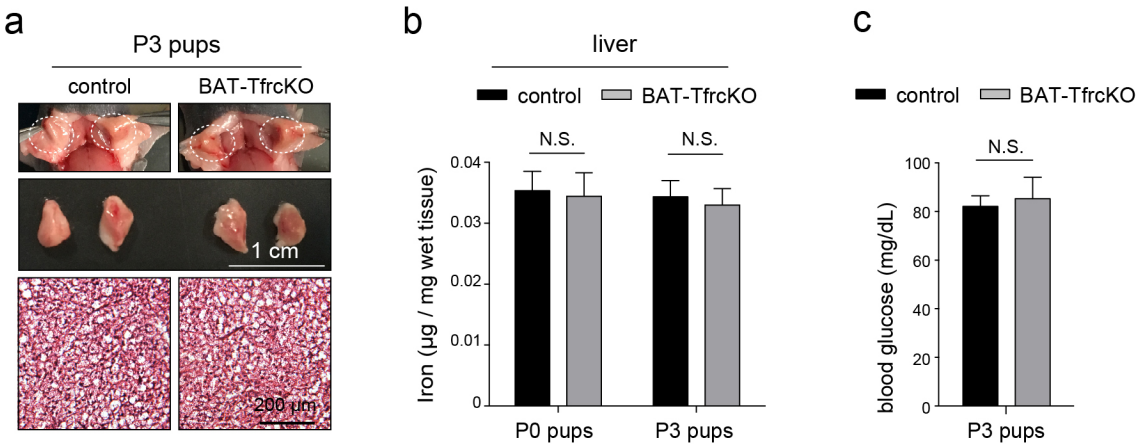

Figure S2.2. Supplementary_ Genetic ablation of TfR1 in BAT abolishes thermogenic activation in newborn mice

A. Upper: images of iBAT in interscapular regions of control and BAT-TfrcKO pups (P3). Middle: images showing the sizes of dissected iBAT from above pups. Lower: H/E staining showing the comparable morphology of brown adipocytes.

B. Liver iron contents of control and BAT-TfrcKO pups at P0 (n=4) and P3 (n=3).

C. Blood glucose level of control and BAT-TfrcKO pups at P3 (n=7).

Pharmacological inhibition of TfR1-mediated iron uptake impairs BAT thermogenic activation in adult mice

Long-term TfR1 depletion and iron uptake blockade expectedly alter mitochondrial functions and have been reported to result in tissue remodeling [122, 123]. These complicate the investigation of the thermogenic activation role of TfR1 in BAT-TfrcKO adult mice. To circumvent these, we utilized gambogic acid (GA) to transiently block TfR1 endocytosis (hence holo-transferrin uptake) in adult wildtype mice [124, 125]. As a validation of GA's function, treating primary brown adipocytes with GA (0.5 μM) abolished ~90% of ISO-induced acute iron uptake (**Figure 2.3A**) without inducing a cytotoxic effect (no change in Caspase-3 cleavage or cell

viability; **Figure S2.3A-B**). Importantly, the treatment of GA did not alter mitochondrial DNA (mtDNA) copy number, mitochondrial protein levels, or the intracellular ATP level (**Figure S2.3C-E**). Seahorse assays indicated that GA (0.5 μM, 30 min) did not affect basal or ISO-stimulated respiration rates yet specifically decreased uncoupled respiration (by ~10%) in primary brown adipocytes (**Figure 2.3B**). Although the level of repression is small, the specific blunting of uncoupled respiration by GA indicates that iron uptake supports thermogenic activation in brown adipocytes.

To investigate the role of iron uptake in BAT activation in adult mice, we injected GA or vehicle into surgically-exposed iBAT of adult *C57BL/6* mice, which received CL injection (i.p.) at the end of the injection/surgery. The non-heme iron content of iBAT (but not liver) in GA/CL-injected mice was lower than the CL-injected control (~85% of the control; 12 hrs after CL injection), confirming the blockade of iron uptake in iBAT (**Figure S2.3G**). The mice were monitored in metabolic cages 12-hr before and after GA and CL injections. Indirect calorimetry data (collected between 1.5 hrs before and 2.5 hrs after GA/CL injection) revealed that CL expectedly increased the energy expenditure (E.E.) and VO_2 in control mice; however, GA blunted the increases without affecting the respiratory exchange ratio (RER) or physical activity (**Figure 2.3C-E**, **S2.3F**). Besides the repression of acute thermogenesis, GA also reduced PGC1α and UCP1 expression as well as mRNA levels of BAT activation markers (12 hrs after GA/CL injection; **Figure 2.3F-G**). The above GA treatment in vivo did not result in Caspase-3 cleavage (**Figure S2.3H**). Thus, acute inhibition of TfR1-mediated iron uptake by GA blunted BAT thermogenic activation in adult mice.

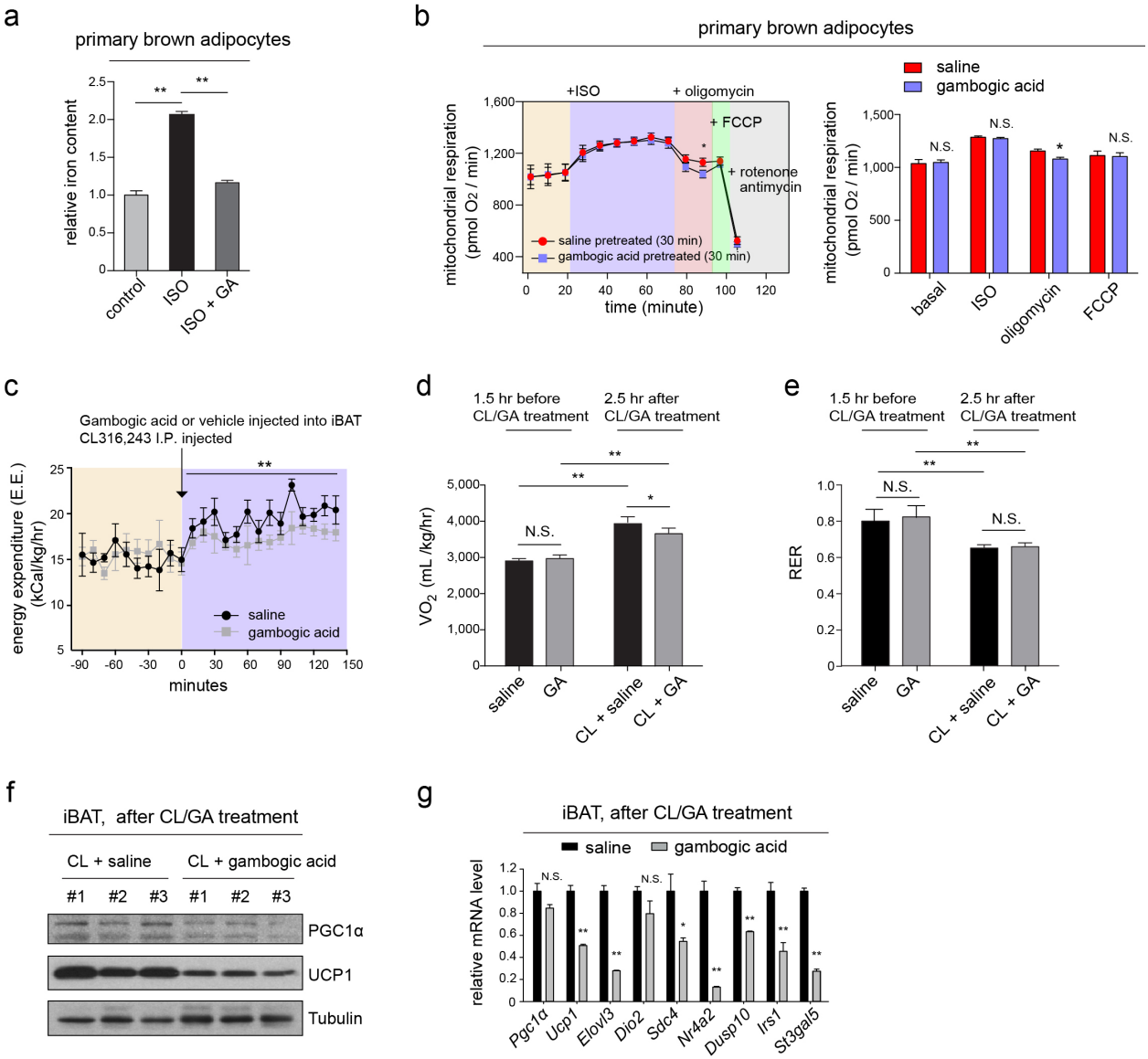

Figure 2.3. Pharmacological inhibition of TfR1-mediated iron uptake impairs BAT thermogenic activation in adult mice

A. Chelatable iron contents of primary BA, treated with ISO (ISO), or ISO and gambogic acids (ISO + GA).

B. Left: a representative trace of Seahorse assays for primary BA pretreated with gambogic acids (blue) or vehicle (red) for 30 min. Right: calculated basal, ISO-stimulated, uncoupled (oligomycin), and FCCP-induced respiration rates.

C. Averaged whole-body energy expenditure (E.E.) of CL/vehicle-treated and CL/GA-treated mice (3 mo.) from 1.5-hr before to 2.5-hr after the injections (n=6).

D. Averaged VO_2 of CL/vehicle-treated and CL/GA-treated mice (1.5-hr before to 2.5-hr after).

E. Averaged RER of CL/vehicle-treated and CL/GA-treated mice (1.5-hr before to 2.5-hr after).

F. IB showing lower levels of activation markers PGC1α and UCP1 in GA-treated iBAT after CL-induced activation.

G. RT-qPCR showing lower levels of activation markers in GA-treated iBAT (n=3).

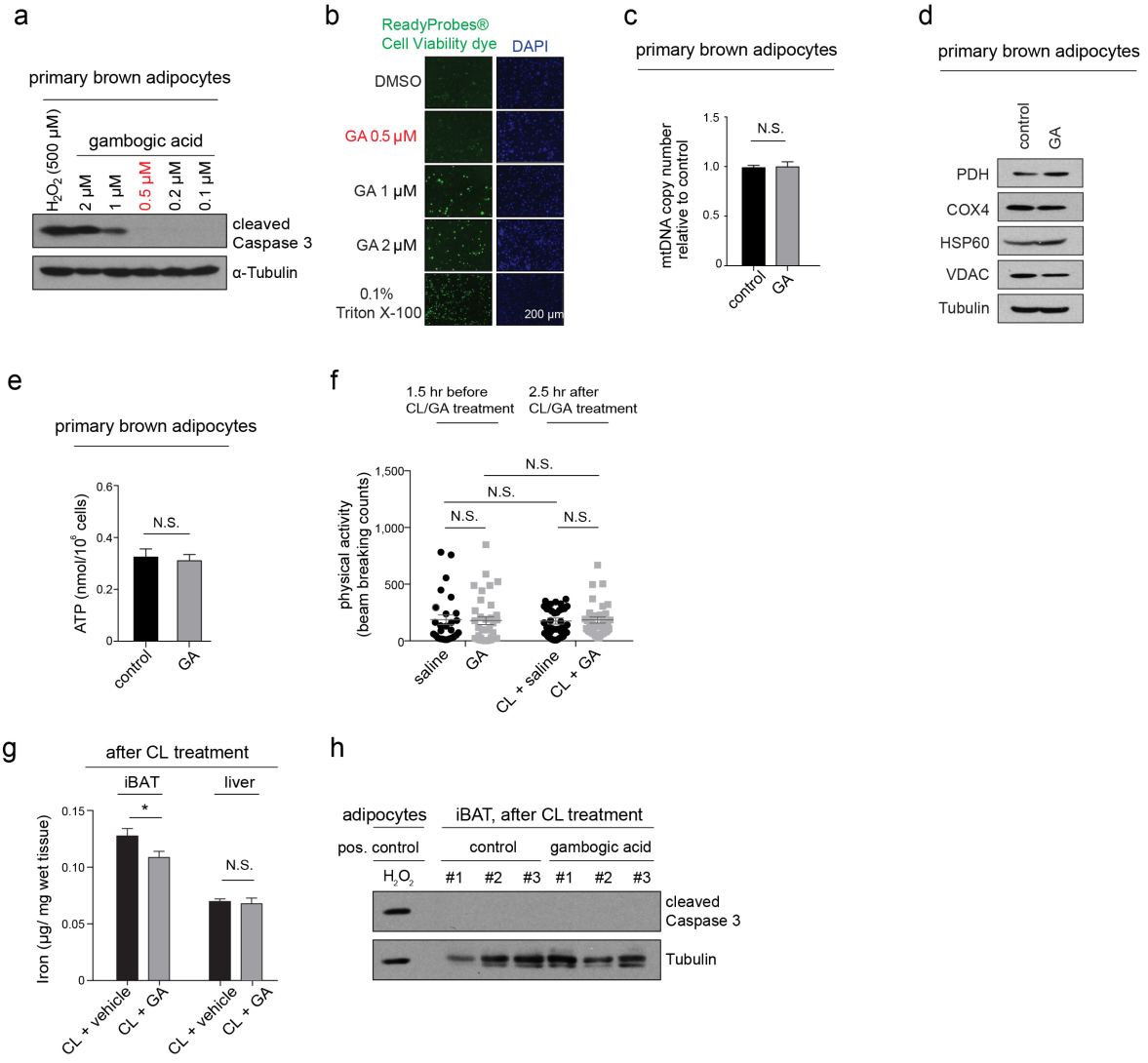

Figure S2.3. Supplementary_ Pharmacological inhibition of TfR1-mediated iron uptake impairs BAT thermogenic activation in adult mice

A. IB of cleaved Caspase 3 in primary BA treated with various concentrations of gambogic acid or H_2O_2 as a positive control.
B. Cell viability assays of primary BA treated with various concentrations of gambogic acid or Triton X-100 as a positive control. Dead cells are positive for green fluorescence; DAPI staining serves as a cell density control. Notably, the results were consistent with cleaved Caspase 3 IB results.
C. mitochondrial DNA (mtDNA) copy numbers (normalized to genomic DNA) in primary BA treated with vehicle or GA (0.5 μM).
D. Mitochondrial protein levels in primary BA treated with vehicle or GA.
E. Total cellular ATP levels in primary BA treated with vehicle or GA.
F. Averaged physical activities of CL/vehicle-treated and CL/GA-treated mice within 1.5-hr before and 2.5-hr after the treatment (n=6).
G. Chelatable iron contents of iBAT and liver in above mice after CL/vehicle or CL/GA treatment (n=6).
H. IB of cleaved Caspase 3 in iBAT from above mice.

Iron induces mitochondrial Fenton chemistry and activates uncoupling thermogenesis

We next investigated the molecular mechanism underlying BAT thermogenic activation associated with iron uptake. In both cold-activated iBAT and ISO-activated primary BA, thermogenic activation increased non-heme iron contents in mitochondrial fractions (**Figure 2.4A-B**), implicating mitochondria as a primary effectory site. As described above, gambogic acid

treatment during the activation of brown adipocytes did not affect basal and ISO-induced respiration rates. As such, we focused on the functions of mitochondrial chelatable iron (rather than the biogenesis of iron-sulfur clusters and heme) in the following study.

In mitochondria, chelatable iron can react with ETC-originated superoxide ($\bullet O2^-$) and hydrogen peroxide (H_2O_2) and catalyze the coupled Haber-Weiss reactions (**Figure 2.4C**). The net effect is the destruction of $\bullet O2^-$ and H_2O_2 in exchange for the production of hydroxyl radical (OH•). The second reaction of the Haber-Weiss reactions (also called Fenton reaction) can be distinguished from the first reaction by the increase of Fe^{3+}/Fe^{2+} ratio as well as by the hallmark OH• production. Rhodamine B-[(1,10-phenanthrolin-5-yl)-aminocarbonyl]benzyl ester (RPA) is a specific and stoichiometric sensor for mitochondrial chelatable Fe^{2+} with its fluorescence quenched upon Fe^{2+} binding [126]. RPA fluorescence increased within the first 5 hrs of ISO-treatment, indicating a decreased amount of mitochondrial chelatable Fe^{2+} in early activation (**Figure 2.4D**). MitoROS™ OH580 is a fluorescence sensor for mitochondrial OH•. Its fluorescence steadily increased after ISO-treatment, indicating an increase of mitochondrial OH• levels during thermogenic activation (**Figure 2.4E**). The above observations support accelerated mitochondrial Fenton reaction during early thermogenic activation.

As a non-enzyme chemical reaction, Fenton chemistry cannot be blockaded through a genetic approach. To delineate the role of Fenton chemistry in BAT activation, we utilized 2,2'-Bipyridyl (BPD) to specifically chelate free Fe^{2+} that is essential for Fenton chemistry (**Figure 2.4C**). To validate the effect of BPD on Fenton reaction, brown adipocytes were treated with BPD (200 μM) or vehicle for 30 min before ISO-simulated activation. Comparing to the vehicle, BPD treatment increased RPA fluorescence (**Figure S2.4A**) and decreased MitoROS™ OH580 fluorescence (**Figure S2.4B**), indicating decreased Fe^{2+} and OH• production in mitochondria. Since Fenton

chemistry is the sole source of OH• in a biological system, BPD treatment dampened Fenton reaction in activated BA.

We performed Seahorse assays to reveal the functions of chelatable iron and Fenton reaction in uncoupling thermogenesis. Seahorse assays revealed that the above BPD treatment did not alter the basal, ISO-stimulated, or FCCP-induced respiration rates of primary BA yet specifically dampened uncoupling thermogenesis (after adding oligomycin; **Figure 2.4F**). Importantly, BPD treatment did not alter the fluorescence of H_2DCFDA (a non-selective probe for H_2O_2 and many other ROS [127]; **Figure S2.4C**), suggesting that the transient BPD treatment in this study did not perturb the overall ROS level in activated BA. In addition, the treatment of BPD had little effect on mitochondria proliferation as neither mtDNA copy number nor mitochondrial protein levels were altered (**Figure S2.4D-E**).

The dampened uncoupling thermogenesis after BPD treatment might attribute to decreased mitochondrial ETC activity/respiration rate due to limited iron availability for mitochondrial biosynthesis of heme and iron-sulfur clusters. To exclude this possibility, we examined the mitochondrial respiration rates in vehicle-treated BA and BPD-treated BA but after BPD withdrawal and washing out. To wash out BPD, both types of cells were treated with perfringolysin O (PMP) to permeabilize the plasma membrane (mitochondrial membranes remain intact) and extensively washed by mitochondrial respiration assay buffer. Seahorse assays indicated that the mitochondrial respiration rates were comparable between vehicle-treated mitochondria and BPD-treated mitochondria after BPD withdrawal/washout (**Figure S2.4F**). As the putative effects of BPD on biosynthesis of Fe-S clusters and heme cannot be reversed by washing, the result from the above Seahorse assays confirmed that the overall mitochondrial respiration and ETC activity was not affected by the BPD treatment in this study.

Consistent with the blunted uncoupling respiration by BPD in activated brown adipocytes, BPD injection into iBAT in vivo similarly repressed the increase of E.E., VO_2, and VCO_2 in response to acute cold stress (30°C to 16°C; immediately following BPD injection; **Figure 2.4G**, **S2.4G**, **S2.4H**). Under the cold stress, BPD-injected mice had a lower RER than mock-injected control mice (**Figure S2.4I**), suggesting a compensatory increase of whole-body fatty acid oxidation as a result of impaired BAT thermogenesis under cold stress. No change of physical activity was observed in the above indirect calorimetry assays (**Figure S2.4J**).

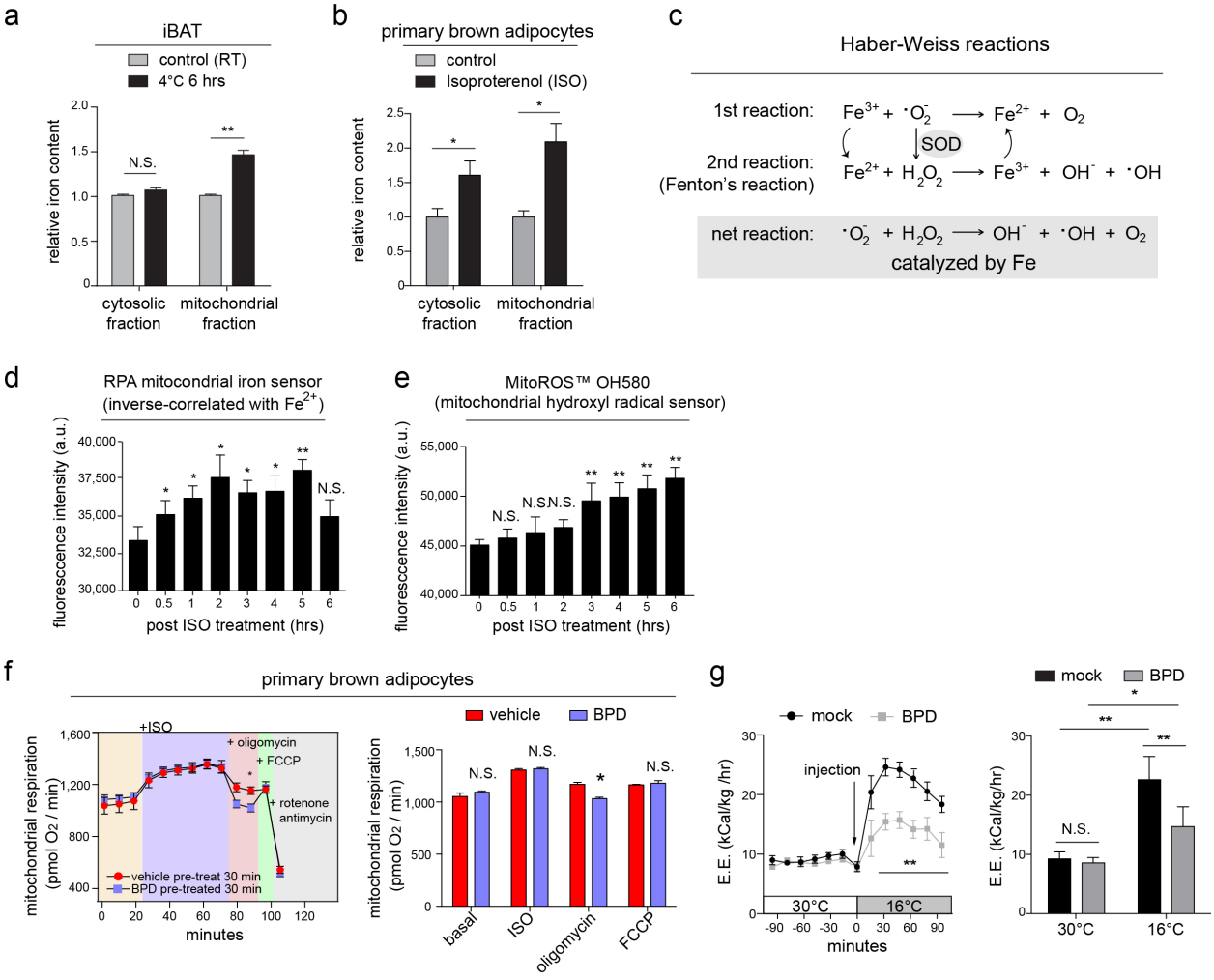

Figure 2.4. Iron induces mitochondrial Fenton chemistry and activates uncoupling thermogenesis

A. Chelatable iron contents of mitochondrial and cytosolic fractions of iBAT (n=3) before and after activation.

B. Chelatable iron contents of mitochondrial and cytosolic fractions of primary BA before and after activation.

C. A diagram depicting Habor-Weiss/Fenton reactions in a biological system.

D. Fluorescence of RPA in primary BA during a 0~6 hr time course of ISO-induced activation.

E. Fluorescence of MitoROS® OH580 sensors in primary BA during a 0~6 hr time course of ISO-induced activation.

F. Seahorse assays showing BPD (30 min pretreatment) reduced uncoupled respiration in ISO-activated primary BA.

G. Left: trace curves of indirect calorimetry showing blunted cold-induced acute increase of E.E. after BPD injection. Right: averaged E.E. of BPD-treated and control mice before and after cold exposure (n=4).

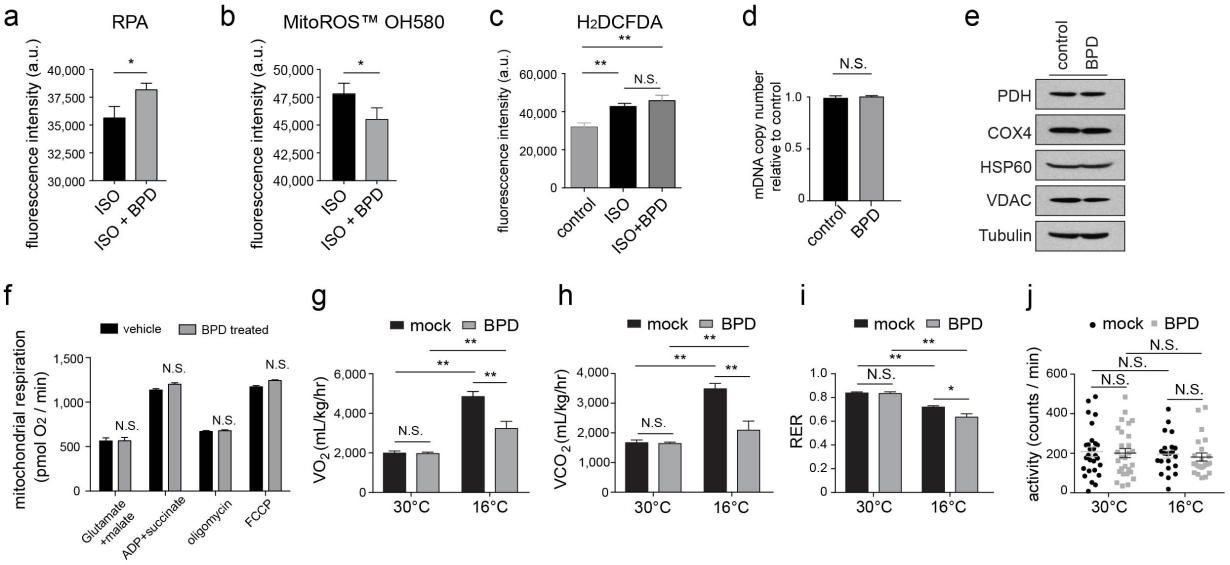

Figure S2.4. Supplementary_Iron induces mitochondrial Fenton chemistry and activates uncoupling thermogenesis

A. Fluorescence of RPA showing decreased Fe^{2+} in mitochondria of ISO-stimulated primary BA after BPD treatment.
B. Fluorescence of MitoROS® OH580 showing decreased OH• in mitochondria of ISO-stimulated primary BA after BPD treatment.
C. Fluorescence of H_2DCFDA showing BPD did not affect the increase of H_2O_2 upon ISO treatment.
D. Unchanged mitochondrial DNA (mtDNA) copy numbers in primary BA after BPD treatment.
E. Comparable mitochondrial protein levels in primary BA after BPD treatment.
F. Seahorse assays of PMP-permeabilized primary BA showing permeabilization and later BPD washout completely reversed the repressive effect of BPD on uncoupled respiration (compare to Figure 2.4G).
G. VO_2 of BPD or vehicle-treated mice before and after cold stimulation (n=4).
H. VCO_2 of BPD or vehicle-treated mice before and after cold stimulation
I. RER of BPD or vehicle-treated mice before and after cold stimulation
J. Activity of BPD or vehicle-treated mice before and after cold stimulation

An increase of intracellular iron is sufficient to activate uncoupling thermogenesis in brown adipocytes

Next, we asked whether increasing iron content is sufficient to induce uncoupling thermogenesis. In the absence of any exogenous sympathetic stimulus, treatment with iron-saturated holo-transferrin (two Fe^{3+} ions per transferrin protein; 55 μg/mL, for 2 hrs) did not

significantly alter intracellular chelatable iron levels (Calcein-AM fluorescence [128]) in primary BA (**Figure S2.5A**). As TfR1 receptor is acutely induced during sympathetic activation, we attribute the above negative observation to the limited capacity of Tf/TfR1-mediated iron uptake in BA in absence of sympathetic stimulation. To force TfR1-mediated iron uptake without sympathetic stimulation, we generated recombinant holo-ferritin nanocages (holo-HFn; see Method section), which held ~2,500 Fe^{3+} ions per ferritin nanocage and can be internalized via TfR1-mediated endocytosis [129, 130]. Holo-HFn treatment (55 μg/mL, for 2 hrs) increased chelatable iron content in unstimulated BA (**Figure S2.5A**). Compared to control unstimulated BA or apo-HFn-treated BA, holo-HFn nanocage-treated BA had elevated basal and uncoupled respiration in the absence of exogenous sympathetic stimulation (**Figure 2.5A**), supporting that iron per se is sufficient to induce thermogenesis.

To further confirm the thermogenic effect of iron in mitochondria, we circumvented TfR1-mediated iron uptake and treated permeabilized iBAT tissues with ferric ammonium citrate (FAC). The BAT tissue permeabilization is necessary for measuring responses of BAT mitochondria to prompt changes of iron in high-resolution respirometry (Oroboros). Oroboros assays indicated that the addition of ATP expectedly reduced complex I/II-supported uncoupled respiration, in line with the inhibitory effect of ATP on UCP1 uncoupling (**Figure 2.5B**). In this state, the increase of chelatable iron concentration by FAC addition to 2 mM (a concentration close to the endogenous chelatable iron concentration in activated iBAT; refer to Figure 2.1C) acutely led to a stable increase of respiration, which can be completely reversed by cyanide (**Figure 2.5B**, **S2.5B**). It has been reported that ATP synthase activity is low in BAT mitochondria [131]. The increase of respiration upon FAC addition suggests that chelatable iron can negate ATP's inhibitory effect on UCP1 uncoupling. Nicaraven [1,2-bis(nicotinamido)-propane] specifically neutralizes hydroxyl

radicals but not other ROS [132, 133]. The addition of Nicaraven (0.5 mM) abolished FAC-induced respiration increase (**Figure 2.5C**, **S2.5B**), suggesting a role of hydroxyl radicals (from iron-catalyzed Fenton reaction) in iron-induced thermogenesis.

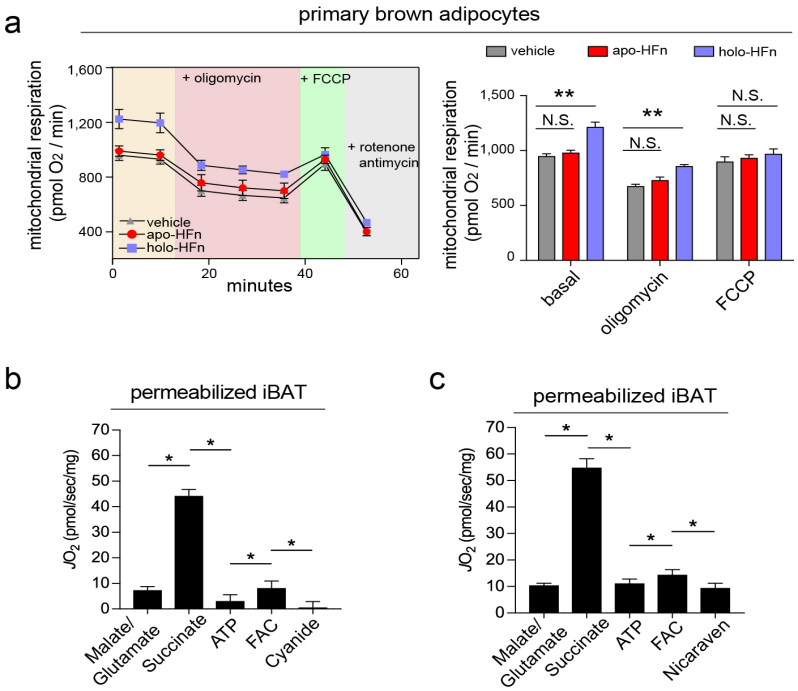

Figure 2.5. An increase of intracellular iron is sufficient to activate uncoupling thermogenesis in brown adipocytes

A. Seahorse assays showing iron-loaded holo-ferritin nanocages (holo-HFn) treatment (2 hrs pretreatment) increased basal and uncoupled respiration rates compared to primary BA treated with vehicle or apo-ferritin nanocages (apo-HFn).

B. Oroboros-2k respirometry of permeabilized iBAT showing FAC negated ATP's effect on UCP1-dependent uncoupled respiration (n=6).

C. Oroboros-2k respirometry showing hydroxyl radical-scavenger Nicaraven negated the thermogenic effect of FAC (n=6).

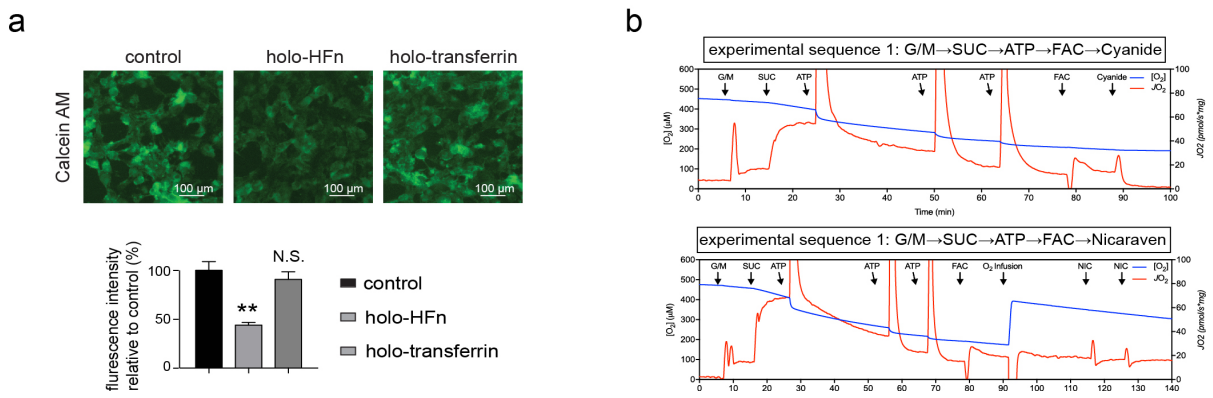

Figure S2.5. Supplementary_An increase of intracellular iron is sufficient to activate uncoupling thermogenesis in brown adipocytes

A. Upper: representative images of primary BA treated with holo-HFn, holo-transferrin, or vehicle for 2 hrs and followed by Calcein AM staining. Notably, only holo-HFn increased intracellular Fe^{3+} content in the absence of exogenous sympathetic stimulation. Lower: quantitative reading of Calcein AM fluorescence.

B. Upper: a representative oxygraph showing changes in respiration rates shown in Figure 2.5B. Lower: a representative oxygraph showing changes in respiration rates shown in Figure 2.5C.

Mitochondrial chelatable iron induces lipid peroxidation and protein thiol oxidation and protects against oxidative stress during thermogenic activation

We next sought to further delineate the molecular mechanism underlying the thermogenic effect of iron. Malate, succinate, and glutamate were included in the assay buffer of the above Oroboros assays. Succinate increases superoxide production from ETC in BAT mitochondria and drives thermogenic activation [113]. Thus, we asked whether FAC-induced thermogenesis depends on succinate. Intriguingly, FAC lost its thermogenic effect in absence of succinate in Oroboros assays (**Figure 2.6A**), suggesting mitochondrial ROS is essential for the thermogenic effect of iron. This is consistent with the notion that iron itself does not induce an oxidative state

but can convert ETC-originated ROS (superoxide and hydrogen peroxide) into hydroxyl radicals via Fenton chemistry.

Hydroxyl radicals from Fenton reaction can non-enzymatically react with polyunsaturated fatty acids (PUFAs) and initiate membrane lipid peroxidation [134]. Previous studies indicate that lipid peroxidation augments in BAT during acute activation [110, 135]. In addition, PUFAs have been reported to boost BAT activity [136, 137]. As such, we hypothesized that hydroxyl radicals may induce acute thermogenesis by virtue of the initiation of lipid peroxidation. Indeed, intra-tissue injection of BPD completely prevented the increase of lipid hydroperoxides in cold-activated iBAT (**Figure 2.6B**), suggesting chelatable iron-catalyzed Fenton chemistry is a major source of lipid peroxidation during BAT activation.

U-74389G is a potent neutralizer of membrane lipid peroxidation [138]. We examined whether Fenton chemistry-induced lipid peroxidation is important for the thermogenic effect of iron. Oroboros assays (with succinate) indicate that U-74389G abolished FAC-induced respiration (**Figure 2.6C**).

Both hydroxyl radicals and reactive aldehydes from lipid peroxidation are potent inducers of protein thiol oxidation [139]. We hypothesized that iron-induced thermogenesis eventually leads to thiol oxidation of mitochondrial proteins, which, at least in case of UCP1, contributes to uncoupling thermogenesis [110]. To test this hypothesis, we measured free thiol contents in mitochondrial and cytosolic fractions of iBAT (normalized to total protein levels). Under thermoneutrality, the free thiol (-SH, reduced form) content of cytosolic fraction was 2-fold higher than the mitochondrial fraction, confirming a more oxidative state of BAT mitochondria compared to the cytosol (**Figure 2.6D, left**). CL-induced BAT activation (2 hrs) decreased free thiol contents in both mitochondria and cytosol (**Figure 2.6D, left**), consistent with the occurrence of oxidative

stress during acute thermogenic activation. During CL-induced activation (2 hrs), BPD injection in iBAT partially reversed the decrease of mitochondrial free thiol content (**Figure 2.6D, left**), suggesting a contribution of chelatable iron to protein thiol oxidation in mitochondria during activation.

Glutathione-dependent anti-oxidant system protects against excessive protein thiol oxidation in oxidative stress [140]. Diamide, a direct oxidizer of glutathione, increases protein thiol oxidation and induces acute thermogenesis in brown adipocytes [113]. Next, we sought to understand whether iron chelation by BPD affects diamide-induced acute thermogenesis in brown adipocytes. As previously reported [113], Acute addition of diamide to brown adipocytes markedly increased respiration in Seahorse assays (**Figure 2.6E**). BPD treatment (30 min before Seahorse assays) largely abolished diamide-induced respiration and uncoupling thermogenesis (**Figure 2.6E**). As glutathione was oxidized in the presence of diamide in above assays and had minimal impact on thiol oxidation status, the above respiration repression by BPD implicates that iron-induced radicals/reactive aldehydes directly oxidize thiol groups on mitochondrial proteins.

Intriguingly, in the above-described in vivo BAT activation experiment, BPD injection in iBAT further decreased (rather than increased) the free thiol content in cytosolic fractions of CL-activated iBAT (**Figure 2.6D, right**). The paradoxical increase of cytosolic thiol oxidation after iron chelation suggests that mitochondrial Fenton reaction may protect against the spread of oxidative stress from mitochondria into the cytosol during acute thermogenic activation of brown adipocytes. In support of this view, RT-qPCR confirmed that oxidative stress markers (*Atf3*, *Egr1*, *Fos*, *Gdf15*, *Junb*), which are acutely transcribed in the nucleus during oxidative stress [141] and are indeed elevated after CL-induced activation further increased in BPD-treated iBAT during thermogenic activation (**Figure 2.6F**). Thus, during acute BAT activation, the increase of iron in

mitochondria not only supports uncoupling thermogenesis but also restrains oxidative stress within mitochondria.

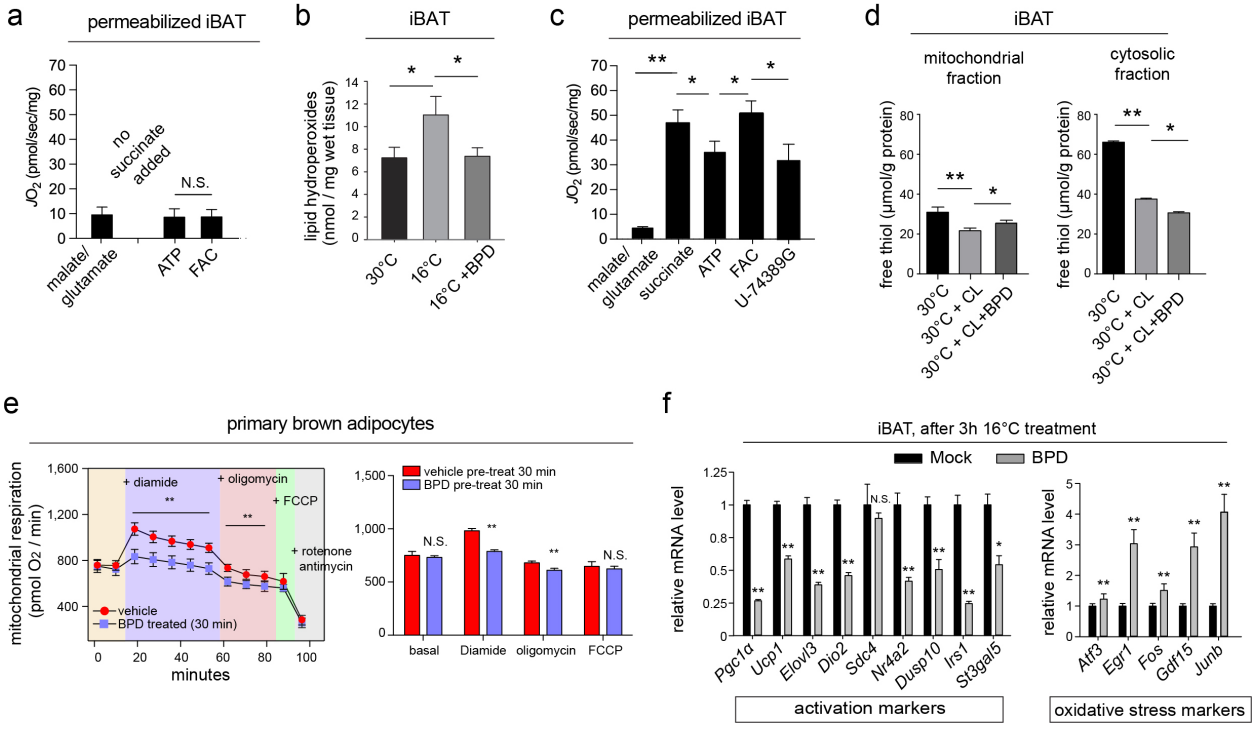

Figure 2.6. Mitochondrial chelatable iron induces lipid peroxidation and protein thiol oxidation and protects against oxidative stress during thermogenic activation

A. Oroboros-2k respirometry of permeabilized iBAT showing FAC has no thermogenic effect in the absence of succinate (n=7).

B. Lipid hydroperoxides in iBAT at TN, after cold exposure or cold exposure combined with BPD injection (n=3).

C. Oroboros-2k respirometry of permeabilized iBAT showing U-74389G negated the thermogenic effect of FAC (n=6).

D. Free thiol contents (normalized to protein) in mitochondrial and cytosolic fractions of iBAT at TN and after CL or combined CL and BPD injections (n=3).

E. Seahorse assays showing BPD dampened diamide-induced total and uncoupled respiration in primary BA.

F. RT-qPCR showing decreased activation markers and increased oxidative-stress related markers in iBAT of BPD-treated mice after cold exposure (n=3).

2.5 Discussion

Taken together, the data in this study support that TfR1-mediated iron uptake, mitochondrial OH• production via chelatable iron-catalyzed Fenton chemistry, membrane lipid peroxidation, and mitochondrial protein thiol oxidation constitute an oxidation cascade that contributes to the acute thermogenic activation in BAT.

TfR1-mediated iron uptake virtually occurs in all types of cells, which plays a pivotal role in iron homeostasis. This study revealed that sympathetic activation initiates acute iron uptake in BAT via TfR1, which echoes similar effects of catecholamines on liver and muscle cells [142]. Catecholamines stimulate the functional conversion of cytosolic aconitase (cACO1) to iron regulatory protein-1 (IRP1), hence stabilizes *Tfrc* mRNA and promotes its translation [120, 142]. This mechanism may underlie the increases of *Tfrc* mRNA and TfR1 protein at 1-2 hrs after CL-induced BAT activation (Figure 2.1F, G). Intriguingly, cytosolic H_2O_2 triggers the above functional conversion by oxidizing a [4Fe-4S] cluster in cACO1 [143]. Thus, oxidative stress occurring during the early BAT activation may act as an initial trigger of TfR1-dependent iron uptake. As a result of iron uptake and iron accumulation in mitochondria, the augmentation of Fenton reaction converts relatively stable H_2O_2 into short-lived OH•, which might restrain oxidative stress in mitochondria in support of thermogenesis and lessen its genotoxic effect. The

above feedback mechanism may finetune iron uptake with redox homeostasis in support of BAT thermogenesis.

Both genetic and pharmacological assays demonstrated a predominant role of TfR1 in acute iron uptake upon BAT activation. However, contributions from other iron uptake mechanisms cannot be excluded. Notably, Lipocalin-2, a mammalian scavenger of iron-siderophores, has been shown to stimulate BAT activation independent of adrenergic stiumuli [144]. This corroborates with the observation in this study that iron itself is sufficient to induce thermogenic activation. Further investigation is warranted to define the physiological relevance of Lipocalin-2 in BAT iron uptake and its impacts on BAT iron homeostasis.

The thermogenic effect of chelatable iron in brown adipocytes is substantiated by the observations from BPD-treated activated brown adipocytes. Notably, the treatment of Fe^{2+}-chelator BPD in this study did not affect the basal or ISO-induced respiration rates in mitochondria, whereas specifically dampened the uncoupled respiration (**Figure 2.4F**). Thus, chelatable iron directly activates uncoupling thermogenesis rather than augments ETC respiration in brown adipocytes. Iron chelation may affect the biosynthesis of heme and iron-sulfur clusters in mitochondria; however, this is not the case in this study since BPD-treated mitochondria had unaltered respiration after the washing out of BPD (**Figure S2.4F**). The thermogenic effect of chelatable iron is also substantiated by the increases of uncoupled respiration observed both in intact brown adipocytes with TfR1 receptor-mediated iron uptake (holo-ferritin nanocages; **Figure 2.4H**) and in permeabilized brown adipocytes with direct iron loading (FAC treatment; **Figure 2.4I-J**).

How does chelatable iron stimulate uncoupling thermogenesis in brown adipocytes? It is noteworthy that the thermogenic effect of chelatable iron disappeared in the absence of succinate

(**Figure 2.5A**), a potent inducer of ROS generation from mitochondrial ETC [145]. Mitochondrial ROS play a pivotal role in the thermogenic activation by oxidizing thiol groups of UCP1 protein (sulfenylation) [110]. Increasing $\bullet O2^-$ in the mitochondrial matrix, either due to its increased release from complex I as seen in succinate oxidation [113] or by ablating its neutralization in the matrix as seen in AdSod2 KO mice [112], stimulates UCP1-dependent uncoupling thermogenesis. The observation that chelatable iron's thermogenic effect depends on the high levels of ROS from ETC ($\bullet O2^-$ and H_2O_2) corroborates with the catalytic function of chelatable iron in Haber-Weiss/Fenton reactions (converting $\bullet O2^-$ and H_2O_2 into OH•). As $\bullet O2^-$ is critical for BAT thermogenesis, the conversion of $\bullet O2^-$ into OH• catalyzed by chelatable iron appears to be redundant or even detrimental to uncoupling thermogenesis, which is seemingly contradictory to the thermogenic effect of iron. We propose that this paradox may be resolved by a unique "oxidation threading" function of OH• within mitochondria. Compared to $\bullet O2^-$ and H_2O_2, OH• has the shortest action range and lifespan given its highest redox potential and reactivity. Thus, iron-catalyzed OH• production and the effectory sites of OH• are likely also close to complex I/III and mitochondrial inner membrane (MIM; where $\bullet O2^-$ and H_2O_2 are generated from ETC). The phospholipids constitution of BAT MIM includes very high concentrations of PUFAs [146] – the substrates for lipid peroxidation chain reactions. Thus, OH• from iron-catalyzed Fenton chemistry may initiate lipid peroxidation chain reactions on MIM, which could propagate along the inner membrane and eventually leads to the oxidation of thiol groups of MIM-bound UCP1 [110] and perhaps other uncouplers (e.g., adenine nucleotide translocase [117]). Therefore, while ETC-originated ROS are undoubtedly the primary causes of the oxidative state essential for BAT thermogenesis, OH• from mitochondrial Fenton chemistry may amplify and spread the oxidative state in BAT mitochondria during acute activation. In line with the above, previous studies have

demonstrated critical roles of PUFAs [136, 137] and lipid peroxidation product 4-HNE [117, 118] in BAT thermogenesis. In this study, BPD treatment blunted ISO-induced protein thiol oxidation in mitochondria (**Figure 2.6D**) as well as diamide-induced uncoupling thermogenesis (**Figure 2.6E**). These observations support that chelatable iron contributes to the oxidative state during thermogenic activation.

In addition to Fenton reaction in the mitochondrial matrix, $\bullet O2^{-}$ is also released from ETC/complex III into intermembrane space and converted to H_2O_2 by Cu,Zn-SOD/SOD1 [145, 147]. Iron-catalyzed Fenton reaction may also take places on the cytoplasmic side of MIM. Indeed, BPD treatment during BAT thermogenic activation paradoxically elevated the thiol oxidation in the cytosol (**Figure 2.6D**). This observation implicates that iron-catalyzed Fenton reaction converts long-life and diffusible H_2O_2 into short-life OH• on the cytoplasmic side of MIM and consequently restrains the oxidative state within mitochondria for thermogenesis. This supposition is consistent with the further increases of expression levels of oxidative stress-responsive genes in CL-activated brown adipocytes with BPD treatment (**Figure 2.6F**), which attests a protective effect of chelatable iron against oxidative stress in brown adipocytes.

Overall, this study revealed a previously unappreciated physiological function of chelatable iron in BAT thermogenic activation. The finding that Iron has a thermogenic effect may lead to new insights in the prevention and treatment of metabolic diseases. It has been reported that iron deficiency increases the susceptibility to ischemic heart disease [148] and is associated with worse prognosis of chronic heart failure [149]. Thus, the finding of a protective role of sufficient iron under oxidative stress may also have broader implications in the preventive healthcare of oxidative stress-related diseases.

CHAPTER 3

IRON DEFICIENCY IMPAIRS SATELLITE CELL PROLIFERATION AND SKELETAL MUSCLE REGENERATION VIA STABILIZING HIF2α

3.1 Summary

Skeletal muscles manifest excellent potential to regenerate after injury via muscle stem cell (also called satellite cells) expansion and differentiation. Iron homeostasis is crucial for skeletal muscle physiology. However, the biological function of iron in satellite cells and skeletal muscle regeneration remains largely unknown. Here we reported the pivotal role of iron in skeletal muscle regeneration. We observed the increase of iron homeostasis-related genes and iron ion level in the proliferating myoblasts (activated satellite cells), comparing to starvation-induced non-cycling myoblasts. Deprivation of iron impaired satellite cell proliferation both *in vitro* and *in vivo*. Furthermore, iron deficiency severely jeopardized the regeneration after cardiotoxin-induced muscle injury. Mechanically, iron depletion stabilized hypoxia-induced factor 2 (HIF2α) in the nuclei, and HIF2α blocked satellite cell proliferation via Rb1/E2F pathway. HIF2α or Rb1 inhibition rescued the iron deficiency-induced myoblast proliferation defect. Remarkably, pharmacological inhibition of HIF2α by PT-2385 improved muscle regeneration in iron deficient mice. Overall, our findings delineated a critical function of iron in muscle regeneration through HIF2α-Rb1/E2F signaling and provided a therapeutically target to promote muscle regeneration for iron deficient population.

3.2 Introduction

The life-long maintenance of muscle tissue is orchestrated by satellite cell-mediated muscle regeneration. Satellite cells possess the ability to regenerate upon injury and to adapt to physiological demands such as growth or training. Once activated, satellite cells undergo proliferation and differentiation to repair injured muscle fibers. A recent study reported profound changes in the muscle expression of heme and iron genes during muscle damage and regeneration [150]. They made the conclusion that macrophage plays a critical role in skeletal muscle regeneration by recycling iron. Selective disruption of macrophage ferroportin (Fpn) resulted in abnormal iron accumulation within muscle-infiltrating macrophages and jeopardized muscle healing, prompting fat accumulation [150]. However, the homeostasis and direct biological function of iron on satellite cells during skeletal muscle regeneration have not been exclusively characterized. Moreover, since satellite cells exhibit a limited number of mitochondria and lower oxhphos activity[151, 152], whether there is any mitochondria independent mechanism that plays a role in regulating iron deficient phenotype in satellite cells remains to be explored.

Iron is reported to engage in proliferation in various cell types [153-155]. E2F transcriptional factors and retinoblastoma tumor suppressor protein (pRb) are well-known regulators of proliferation, involving the regulation of cell cycle progression, DNA replication and DNA repair. Rb1/E2F axis was found participated in skeletal muscle regeneration. E2F1 and E2F2 were highly induced during skeletal muscle regeneration. Mutation of E2F1 resulted in a defect in skeletal muscle regeneration [156]. Meanwhile, lack of Rb1 in satellite cells could accelerate the cell cycle re-entry of quiescent satellite cells, leading to the expansion of satellite cell and its progeny myoblasts [157]. In contrast, overexpression of p16INK4 induced a reduction in phosphorylation of Rb, further repressing Rb/E2F targets. It resulted in the blocking of cell cycle progression and

further led to senescence [158, 159]. Given this, the relationship between iron homeostasis and Rb1/E2F pathway in proliferation regulation and whether they play roles in skeletal muscle regeneration remains to be a knowledge gap that intrigues us for further exploration.

Here, we show the importance of iron on satellite cell proliferation and muscle regeneration. Upon iron depletion, progenitor cells failed to proliferate, and skeletal muscle regeneration was jeopardized. Low iron stabilized HIF2α, which blocks E2F pathway by directly inducing Rb1. Accordingly, pharmacological inhibition of HIF2α by PT-2385 can rescue the impairment of regeneration of iron deficient mice, which might provide a potential therapeutic target.

3.3 Materials and Methods

Animal studies

All animal studies were approved by the University of Georgia Institutional Animal Care and Use Committee (IACUC) and performed following the guidelines. Animals were raised in a temperature-controlled (22°C) environment with 12:12-hrs light:dark cycle and allowed food and water *ad lithium*. All mouse strains were purchased from the Jackson Laboratory: *C57BL/6J*, *Pax7*^{CreERT2}(Jax:017763); *R26R*$^{CAG\text{-}Sun1/sfGFP,}$ (Jax: 021039). For the generation of mild iron deficient mouse models, *C57BL/6J* mice (4-wk old) were fed with iron-sufficient (IS) diet (35 ppm, Dytes #115127) or iron deficient (ID) diet (3 ppm, Dytes #115072) for 8 weeks. Blood hemoglobin levels were measured by HemoCue Hb^{201+} Hemoglobin analyzer (HemoCue). For induction of muscle injury, CTX (0.5 nmol, 50 μl) was injected into one side of TA muscles of iron sufficient and iron deficient mice. TA muscles were collected at post-injury day (dpi) 10 and 30 for characterization. For PT-2385 administration, from 2 days after CTX induced injury, PT-2385 (1ug, 50ul) was injected into the damaged side of TA muscles for 3 consecutive days.

Satellite cells isolation and FACS

nmGFP^{+} SCs (~5 × 10^4) from 3-month-old *SC(Pax7)- INTACT* mice were isolated as previously described [160]. Briefly, all legs muscles were dissected and washed. Then muscles were cut and minced into smooth pulp and digested with collagenase solution (0.2% collagenase Type 2 in DMEM). The digestion lasted for 45-60minutes and triturated in the middle of digestion. The digestion was stopped by adding 2% FBS in DMEM. The mixture was then filtered with 70um cell strainer, followed by 40um strainer. Then Hoechst were stained, and cells were resuspended with FACS buffer for sorting. The sorting of SC was performed on a MoFlo XDP Cell Sorter (Beckman Coulter) to isolate Hoechst and GFP double positive cells.

Cell culture and treatment

C2C12 myoblasts were cultured at growth medium (DMEM containing 10% FBS and 1% penicillin/streptomycin). For serum starvation treatment, cells at 40-50% confluence were washed twice and changed to starvation medium (DMEM with 0.1% FBS and 1% penicillin/streptomycin). The starvation lasted for 3 days. Then full FBS medium (10%) was changed back for another 3 days to refeed the cells. To induce iron deprivation, C2C12 myoblasts were treated with 2,2′-bipyridyl (BPD) (30uM, Sigma Aldrich) for indicative days. DMSO treated myoblasts served as control. For induction of HIF2α, doxycycline (0.25ug/ml, Sigma Aldrich) was added into HIF2α OE C2C12 myoblasts. HIF2α inhibitor, PT-2385 (10uM, Tocris Bioscience) was treated together with BPD or Dox to inhibit the activity of HIF2α for indicative purpose.

siRNA treatment on HIF2α OE myoblasts

HIF2α OE myoblasts were treated with siRNA smart pool against *Rb1*(Santa Cruz Biotechnology, sc-29469) or control siRNA (Santa Cruz Biotechnology, sc-36869). Transfection was performed

using Lipofectamine RNAiMAX (Invitrogen, Carlsbad, CA, USA) according to the manufacturer's instructions.

Inducible HIF2α overexpression construction

Degradation-resistant mouse HIF2α was cloned from pcDNA3 mHIF-2α MYC TM (P405A/P530V/N851A, Addgene #44027) into Tet-on inducible expression system pCW57 (Addgene #71783) for lentivirus packaging. C2C12 inducible HIF2α overexpression cell line was constructed by pCW57-mHIF2α TM OE lentivirus transduction and neomycin selection. HIF2α overexpression was induced by 250 ng/mL doxycycline in culture medium at stated time.

Quantitative real-time PCR

Total RNA was isolated from tissue or cell culture using TRIzol reagent (Thermo Fisher Scientific). 500 ng total RNA was reverse-transcripted into cDNA in 25 µL reverse transcription reactions (Maxima; Life technologies) and diluted into 250 µL. 2 µL diluted cDNA was used in an 8 µL quantitative PCR reaction (SsoAdvanced™ Universal SYBR Green mix; Bio-Rad) on a BioRad CFX384™ Real-Time PCR Detection System. Cq-values were determined and expression values were calculated by BioRad CFX Manager™ Software. Relative expression values were normalized to inner reference genes *Rps18* and *Tbp* of each biological sample.

Protein extraction and immunoblotting

Whole cell lysates were prepared by homogenization in RIPA buffer supplemented with 1x proteinase inhibitor cocktail (Amresco). For nuclei lysate preparation, cells were incubated in lysis buffer (20mM Tris-HCl, pH7.4, 10mM NaCl, 3mM MgCl2 and 0.5% NP40) for 30 minutes on ice. Vortex at high speed during incubation. Then centrifuge cells at 1000g for 5 min at 4.C. Collect nuclei pellet and lysed in RIPA buffer supplemented with 1x proteinase inhibitor cocktail (Amresco). For both whole lysate and nuclei lysate, Protein concentration was quantified by BCA

assays (Thermo Fisher Scientific). Protein lysates were loaded on 10% SDS-PAGE, transferred to PVDF membranes. The membranes were blocked with 5% non-fat milk/TBST, probed with primary antibodies at 4°C overnight. After secondary antibodies incubation, membranes were treated with ECL reagents (ThermoFisher Scientific) and exposed to X-ray films (Santa Cruz).

Calcein AM assay to detect intracellular chelatable iron

Cell culture medium was removed, and cells were washed by PBS and then incubated with 0.25 μM Calcein AM (Life technologies) in reaction buffer (4.5 g L^{-1} glucose, 2 mM glutamine in PBS) for 30 min at 37°C with 5% CO_2. Then cells were washed twice and incubated in PBS for fluorescence intensity measurement at Ex/Em = 495/530 nm. For quantitative comparation, cells were ran into a CytoFlex Cytometer (Beckman Coulter), and profiles were analyzed with FlowJo, version 10.

Flow cytometry for CD71

Cells were digested and washed with PBS. To stain CD71, cells were resuspended with flow buffer (1% FBS, 1mM EDTA and 25mM HEPEs in PBS) with CD71 antibody (CD71, #113805, Biolegend, San Diego, CA, USA) and incubated on ice for 30 minutes. After incubation, cells were washed with flow buffer and ran into a CytoFlex Cytometer (BioTek). Profiles were analyzed with FlowJo, version 10.

Cell viability assay

Cells were stained with ReadyProbe Cell viability imaging kit (Green and Blue, Thermo Fisher Scientific) under the guidance of manual instruction. Briefly, add 2 drops of NucGreen® Dead reagent and 2 drops of NucBlue® Live reagent per mL cell culture medium and incubate for 20 min at 37°C with 5% CO_2. Fluorescence images were captured by EVOS fluorescence microscope (FITC/GFP filter for dead cells and DAPI filter for live cells).

Cell proliferation and DNA content analysis

For cell number counting, C2C12 myoblasts were stained with Hoechst 33342 (Thermo Fisher, Waltham, MA, USA) and imaged were acquired by BioTek Lionheart FX automated microscope. For Edu staining, 10μM Edu were added into culture medium 4 hours before assay. Edu click it kit (C10340, Thermo Fisher Scientific) was utilized for the detection of Edu signal. Briefly, the Edu treated cells were washed and fixed with 4% paraformaldehyde followed by 0.5% Triton X-100 permeabilization. After washing with wash buffer (3% BSA in PBS), Edu was stained with reaction cocktail for 30 minutes at dark. Further Hoechst counter staining was performed before quantification. Images were acquired by BioTek Lionheart FX automated microscope. Positive nuclear were quantified with cell number counting system.

To determine DNA content, C2C12 myoblasts were fixed with 70% ethanol at 4°C for 4 hours. RNA was digested with RNase A. Then cells were stained with Propidium Iodide (PI, Tocris Bioscience) at room temperature for 10 minutes. Myoblasts were run into a CytoFlex Cytometer (Beckman Coulter), and profiles were analyzed with FlowJo, version 10.

Immunofluorescence staining

For staining of myoblasts, fixed cells were permeabilized with 0.5% Triton X-100 for 15 min, washed twice with PBS and then incubated in blocking solution: 5% normal goat serum (Sigma Aldrich, St. Louis, MO, USA) and 1% BSA (Thermo Fisher, Waltham, MA, USA) for 1 hr at room temperature. Cells were incubated with primary antibodies at 4°C overnight. The primary antibody used were anti-Ki67 (#ab15580, Abcam, Waltham, MA, USA) and anti-myogenin (#F5D, DSHB, lowa, IA, USA), anti-HIF2α (#PA1-16510, ThermoFisher, Waltham, MA, USA). After washing, cells were incubated with secondary antibodies (1:250 diluted). The secondary antibodies were affinity purified AlexaFluor anti-mouse 546 and anti-rabbit 488 (Thermo Fisher, Waltham, MA,

USA). Washed cells were counterstained with Hoechst 33342 (Thermo Fisher, Waltham, MA, USA) and mounted with fluoroshield reagent (Sigma Aldrich, St. Louis, MO, USA). Fluorescence images were acquired on an Evos fluorescence microscope. For Ki67 quantification, images were taken with BioTek Lionheart FX automated microscope and Ki67 positive myoblasts were quantified with cell number counting system.

For staining of muscle sections, muscle sections were fixed with paraformaldehyde (PFA)/PBS (4%, 10 min), quenched with glycine (50 mM, 10 min), permeabilized with Triton X-100 (0.5%, 10 min), blocked with Mouse On Mouse (M.O.M.) Blocking Reagent (Vector Laboratories) and 5% BSA/5% normal goat serum/PBS, and incubated with the following primary antibodies: anti-Pax7 (1:5; Developmental Studies Hybridoma Bank [DSHB] Pax7); anti-HIF2α (1:250; Thermo Fisher; PA-16510); anti-Ki67 (1:1,000; Abcam; ab15580); anti–laminin B2 (1:1,000; MilliporeSigma; 05-206); anti-eMyHC (1:50; DSHB; F1.652) overnight at 4°C. Sections were washed in PBS/0.1% Tween-20, incubated with Alexa Fluor–labeled secondary antibodies (1:200, 1 h), and then washed and mounted with DAPI-containing mounting medium (Life Technologies, Thermo Fisher Scientific).

Histological analysis

For histological analysis, transverse sections (10um) of the frozen TA muscles were stained with Hematoxylin (Sigma Aldrich) and Eosin Y (Sigma Aldrich). Images were captured by a light microscope (Leica, DM4000B) equipped with a color camera (DFC420). Cross-sectional areas of TA fibers were measured using ImageJ software. At least How many fibers area was calculated for each muscle section.

Chromatin IP and qPCR (ChIP-qPCR)

For each target, myoblasts were fixed (1% formaldehyde) and resuspended in 100 µl lysis buffer (1% SDS, 10 mM EDTA, 50 mM Tris HCl, pH 8.1, 1× protease inhibitor cocktail) and sonicated at 4°C in a Bioruptor Pico Sonicator (Diagenode) using 15 on/off cycles of 30:30 seconds. The sheared chromatin (~300 bp) was 1:10 diluted in IP dilution buffer (50 mM HEPES-KOH, pH7.5, 140 mM NaCl, 1 mM EDTA, 1% Triton X-100, 0.1% sodium deoxycholate, 0.1% SDS) and centrifuged at 20,000 *g* at 4°C for 10 minutes. The supernatant was transferred to siliconized tubes and incubated with primary antibody for specific targets: 2 µg HIF2α antibody (Thermo Fisher), 2µg H3K27ac antibody (Cell Signaling) or rabbit IgG (Santa Cruz Biotechnology) on a rotating platform at 4°C overnight. PBS-washed Protein A Dynabeads (30 µl 50% slurry) were added to the chromatin-antibody mixture and incubated on a rotating platform at 4°C for 4 hours. All ChIP beads were sequentially washed with low salt, high salt, lithium, and TE buffer 2 times each and reverse cross-linked with 1 M NaCl for 6 hours at 65°C. Samples were digested with 10 µg RNase A (37°C, 0.5 h) and 20 µg proteinase K (55°C, overnight). Genomic DNA (gDNA) for ChIP analysis was purified by phenol/chloroform/isoamyl alcohol (25:24:1) extraction followed by precipitation with 100% isopropanol, 0.3 M sodium acetate, and GlycolBlue (Thermo Fisher Scientific) at –20°C overnight. Primers were used to quantify relative enrichment levels at HRE-flanking regions in promoters of stated genes in the mouse genome. Gene-lacking regions on chromosomes 5 and 6, which serve as inner reference controls in the calculation of relative enrichment levels.

RNA-seq and data analysis

RNA samples were polyA selected and generated into libraries using TruSeq Standard mRNA Library Prep Kits. DNA libraries (C2C12 myoblasts WT, HIF2αOE, HIF2αOE+PT-2385) were sequenced on Illumina HiSeq 4000. RNA-seq raw data were mapped to GRCm38 mouse genome

and analyzed by HISAT2. Differential expression was called by edgeR. Hallmark gene sets were performed with Gene set enrichment analysis (GSEA).

Quantification and Statistical Analysis

All values in the figures represent mean ± s.e.m. with >= 3 biological replicates. Statistical significance was determined by GraphPad Prism 6. Two tailed Student's *t*-tests were used to compare significance between two groups after normality tests. One-way ANOVA with Bonferroni's *post-hoc* tests were performed for multiple comparison. *: $p<0.05$, **: $p<0.01$, N.S.: not significant.

3.4 Results

Iron homeostasis related genes and intracellular iron level is upregulated in activated satellite cells and proliferating myoblast

Transferrin receptors (TfR1, TfR2) and divalent metal transporter 1 (DMT1) are key iron-uptake machinery in mammalian cells [120]. We first wondered the expression of these genes in quiescent (QSCs) and activated satellite cells (ASCs), respectively. To isolate the quiescent satellite cells, we generated a SC-INTACT mouse model as described in our previous study [101], within which greater than 99% of Pax7+ QSCs were genetically labeled with nuclear membrane–located GFP (nmGFP) in the muscle. For satellite cells activating, we injected cardiotoxin into TA muscle and collected samples at post-injury day 5 (5dpi). GFP+ positive QSCs (non-injury) and ASCs (CTX 5dpi) cells were sorted by FACS, and RNA was extracted for analysis. As expected, the mRNA level of proliferation markers *Ccne2*, *Cdk2* and satellite cell activation marker *Myod1* were higher in ASCs than QSCs (**Figure 3.1A**). Meanwhile, genes that are highly expressed in QSCs, *Epas1* and *Spry1*, were repressed in ASCs (**Figure S3.1A**). All these suggest the success of

satellite cells activation. Then we detected the mRNA of iron uptake-related genes *Tfrc*, *Tfr2* and *Slc11a2*. The result showed that *Tfrc*, the main receptor for ferric iron loading, increased significantly in ASCs (**Figure 3.1B**). The mRNA of *Slc11a2* was also elevated in ASCs. However, the expression of *Tfr2* was low and beyond the detection limit to compare between groups.

At 5 dpi, the Pax7+ cells could be a mixture of proliferating satellite cells, differentiating myoblast as well as self-renewing satellite cells. To further distinguish the expression of iron loading genes is higher in activated proliferating myoblast, we detected the mRNA level of iron loading genes in noncycling and cycling C2C12 myoblast *in vitro*. We cultured C2C12 myoblast (50% confluence) in serum-starvation (0.1% FBS) medium for 48 hours to force most of myoblasts in G0/G1 arrest state to mimic noncycling quiescence state. To stimulate activation, we refed the starved cells to 10% FBS culture medium for another 72 hours to induce the cells re-entering the proliferating stage. The staining and quantification of proliferation marker, Ki67, illustrated that starvation greatly limited C2C12 myoblast proliferation to ~27% Ki67 + cells comparing to ~97% proliferating cells (**Figure 3.1C**). Meanwhile, the starved cells were not differentiated, and there was no cell death as indicated by *Myogenin* negative staining (**Figure S3.1B**) and cell-death indicator propidium iodide (PI) staining (**Figure S3.1C**). By comparing the mRNA of iron uptake-related genes, we found that the mRNA level of *Tfrc* was higher in cycling myoblast, whereas *Tfr2* and *Slc11a2* did not change between the two groups (**Figure 3.1D**). Consistently, the protein level of TfR1 was increased upon serum stimulating comparing with starved cells (**Figure 3.1E**). Transferrin receptor 1 (TfR1) is known to facilitate the uptake of iron at the cell surface by internalizing di-ferric transferrin. To check the expression of TfR1 on the cell surface, we stained the live cells with CD71 (also known as TfR1) and performed FACS to compare the cell surface TfR1 in starved and refed myoblasts. The result exhibited the higher expression of

cell surface TfR1 in proliferating myoblasts (**Figure 3.1F**). These data indicate that iron loading genes, especially *Tfrc*, respond to satellite activation, encode and express more TfR1 protein in the cell surface of proliferating myoblasts.

To explore if iron level changed associated with iron loading-related genes, we detected labile iron in starved and refed myoblast by calcien AM staining [161]. When the non-fluorescent acetoxymethyl ester moiety (calcein-AM) enters cells, it is immediately cleaved by cytosolic esterase to its cell-impermeable, fluorescent calcein form. Cytoplasmic labile iron ion binding to calcein quenches its fluorescence. Thereby, the quenchable iron level is inversely correlated with fluorescence intensity [161]. We performed FACS analysis to compare the calcien AM signal and the result showed that proliferating myoblast exhibited lower intensity of calcein AM, indicating more labile iron in the cytosol of activated proliferating myoblasts (**Figure 3.1G**). Taken together, these experiments demonstrated that activated proliferating myoblasts expresses a higher level of iron loading genes and accumulated more iron labile iron in the cytosol.

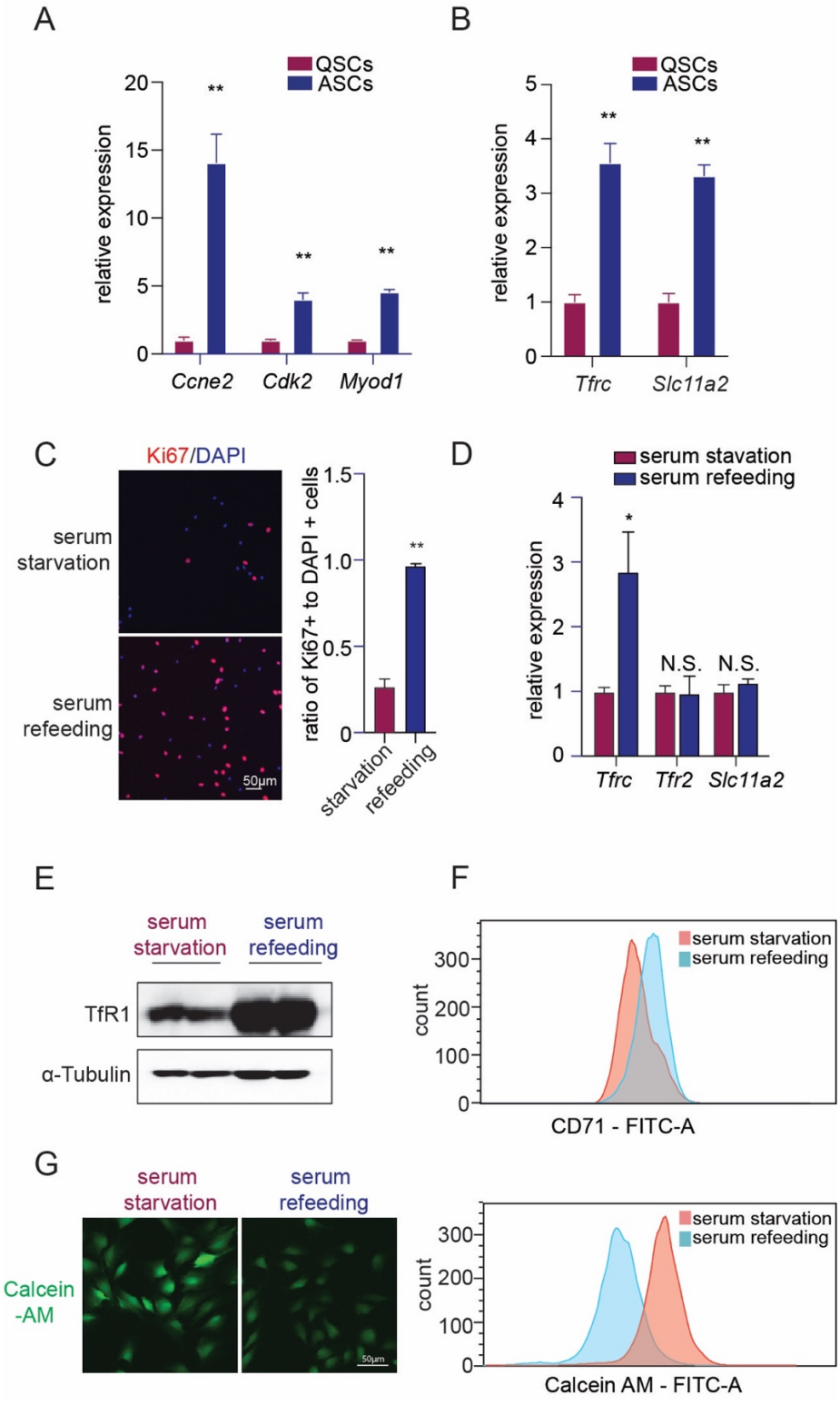

Figure 3.1. Iron homeostasis related genes and intracellular iron level is upregulated in activated satellite cells and proliferating myoblast

A. RT-qPCR of proliferation-related genes and *myod1* in quiescent satellite cells (QSCs) and activated satellite cells (ASCs).

B. RT-qPCR of iron uptake-related genes in quiescent satellite cells (QSCs) and activated satellite cells (ASCs).

C. Ki67 and DAPI staining to compare the ratio of Ki67 positive myoblasts to all myoblasts indicating proliferating.

D. RT-qPCR of iron uptake related-genes in starved non-cycling myoblasts and refed cycling myoblasts.

E. Immunoblot showing higher level of TfR1 in cycling myoblasts comparing with starved non-cycling myoblasts.

F. Fluorescence-activated cell sorting (FACS) analysis of cell-surface marker CD71 showing cell-surface TfR1 in cycling myoblasts.

G. Representative images and flow cytometry histogram showing less calcein-AM fluorescence intensity in cycling myoblasts.

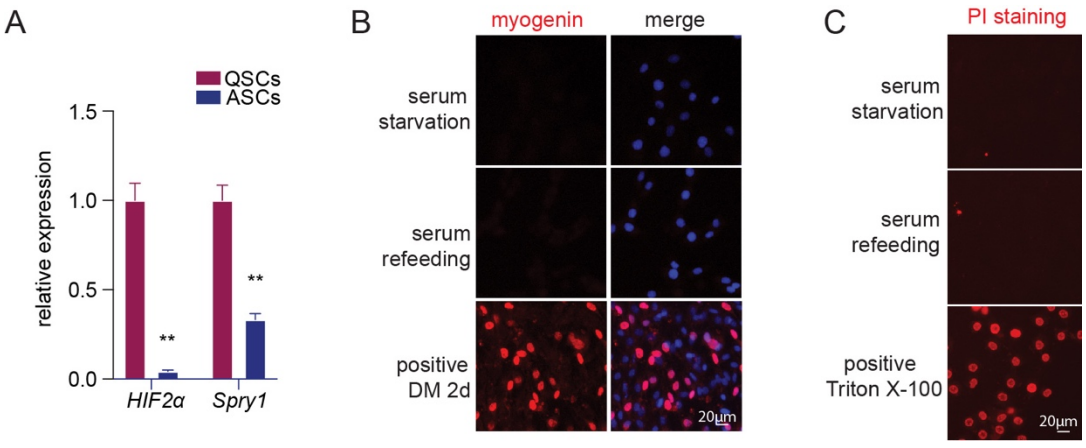

Figure S3.1. Supplementary_Iron homeostasis related genes and intracellular iron level is upregulated in activated satellite cells and proliferating myoblast

A. RT-qPCR of Spry1 and HIF2α in quiescent satellite cells (QSCs) and activated satellite cells (ASCs).

B. Myogenin staining of starved non-cycling myoblasts and refed cycling myoblasts. Differentiated myoblasts serve as positive control.

C. Propidium iodide (PI) staining of starved non-cycling myoblasts and refed cycling myoblasts. Triton X-100 treated myoblasts serve as positive control.

Iron depletion impairs myoblast proliferation

To explore whether iron engages in myoblast proliferation, we deprived iron in C2C12 myoblast by iron chelator, 2,2′-bipyridyl (BPD). We first tested the dosage of the BPD and treated myoblasts with a relatively lower concentration (20uM) to mimic mild iron deprivation. There was no cell death after 5 days of BPD treatment (**Figure S3.2A**). We monitored the cell proliferation by counting cell number. The proliferation curve illustrated that BPD-treated myoblast expanded much slower than control cells (**Figure 3.2A**). Edu staining showed less Edu incorporation after BPD treatment (**Figure 3.2B**). The results suggest that the procession of proliferation in iron chelator-treated myoblasts is slower than control myoblasts.

To determine the consequence of iron deprivation *in vivo*, we established a mild iron deficiency mouse model, mimicking latent iron deficiency in humans. Briefly, to induce iron deficiency, *C57BL/6* mice were fed with a low-iron diet for 8 weeks (**Figure 3.2C**). Littermates that were on a matched iron sufficient (IS) chow were served as control. After 8 weeks of feeding, we first stained TA and soleus muscle section with Pax7 to mark quiescent satellite cells. The quantification of Pax7 positive satellite cells demonstrated that the TA muscle of IS and ID mice contained the comparable number of satellite cells in both TA and soleus muscle (**Figure 3.2D**

and **Figure S3.2B**). The results rule out the potential possibility of mild iron deficiency on satellite cell death. Then we induced skeletal muscle injury by cardiotoxin (CTX) administration into TA. Muscles were collected at 10dpi for characterization of proliferation. We observed that after injury, the number of Pax7+ cells were significantly decreased in the TA muscle of ID mice (**Figure 3.2E**). To quantify proliferating satellite cells, we co-stained satellite cells with Pax7 and proliferating marker Ki67. As showed in Figure 3.2F, the ratio of Ki67 and Pax7 double-positive cells to all Pax7 positive cells was significantly lower in ID mice, indicating less activated proliferating satellite cells. Both the BPD treated myoblasts and *in vivo* iron deficiency mice model show that iron deprivation results in dampened myoblasts proliferation.

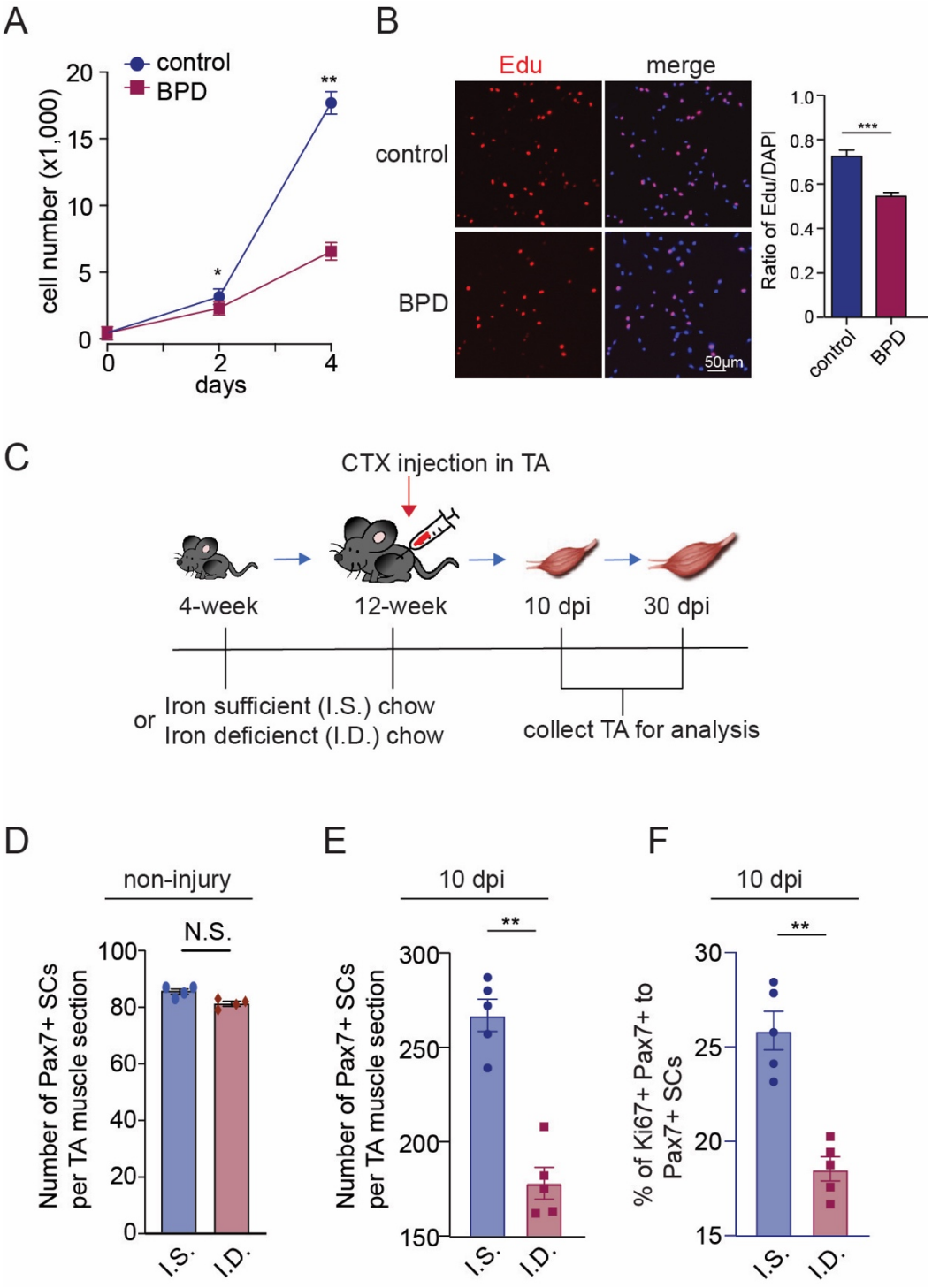

Figure 3.2. Iron depletion impairs myoblast proliferation

A. Proliferation curve of control and BPD-treated C2C12 myoblasts.

B. Representative images of Edu labeling and quantification of the ratio of Edu positive cells to DAPI positive cells of control (DMSO) and BPD-treated C2C12 myoblasts.

C. Diagram depicting the timeline of chow feeding (iron sufficient and iron deficient), CTX injection and sample collection for characterization.

D. Number of Pax7 positive SCs per TA section in undamaged TA muscle of iron sufficient (I.S.) and iron deficient (I.D.) mice (N=4).

E. Number of Pax7 positive SCs per TA section at 10 dpi in TA muscle of iron sufficient (I.S.) and iron deficient (I.D.) mice (N=5).

F. The ratio of Pax7 and Ki67 double-positive SCs to all Pax7 positive SCs per section at 10 dpi in TA muscle of iron sufficient (I.S.) and iron deficient (I.D.) mice (N=5).

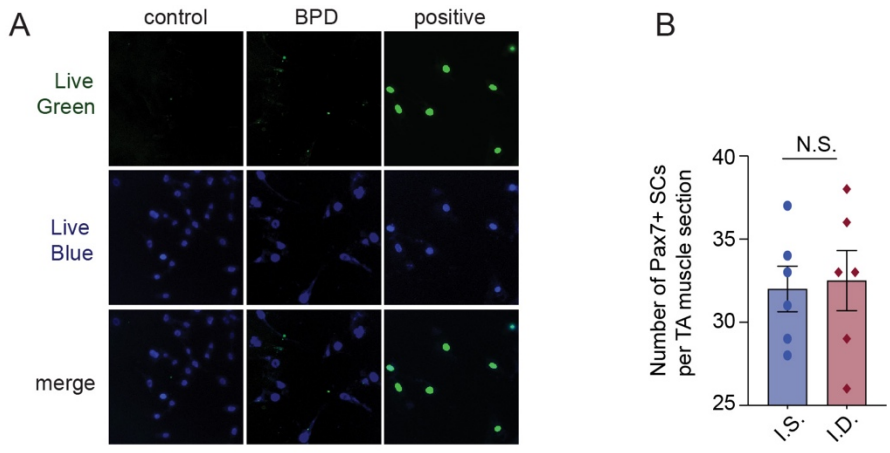

Figure S3.2. Supplementary_Iron depletion impairs myoblast proliferation

A. Live cell dye staining of control and BPD-treated myoblasts showing no cell death after 20μM BPD treatment. Live Green indicates cell death.

B. Number of Pax7 positive SCs per soleus section at 10 dpi in TA muscle of iron sufficient (I.S.) and iron deficient (I.D.) mice (N=5).

Iron deficiency dampens skeletal muscle regeneration

We next investigated whether the capacity of muscle repair was affected by iron deprivation. We collected TA muscle of IS and ID mice at 0 days, 10 days and 30 days of post-injury for histological analysis. After 8 weeks of iron sufficient and iron deficient feeding, the bodyweight of IS and ID mice were comparable (**Figure S3.3A**). Before the injury, no difference between IS ad ID muscle were noticeable. IS and ID mice exhibited normal, well-organized and similar size of myofiber (**Figure 3.3A**). And the nuclei were positioned at the periphery of myofibers. At 10 dpi the TA muscle of IS mice was composed of new myofibers with centrally located myonuclei. However, ID muscles contained a higher amount of fibrotic tissues. The size of ID muscle fibers was smaller than IS muscle. (**Figure 3.3B**). At day 30, IS muscles were fully regenerated. The newly regenerated fibers were large with centralized nuclei. The architecture was restored to normal. However, the TA muscle of ID mice still displayed a smaller fiber size. There were a greater number of smaller fibers (CSA <= 1200μm^2) and fewer larger fibers (CSA >= 1800μm^2) in ID muscle. Fibrotic tissues were also visible in ID muscle (**Figure 3.3C**). Embryonic myosin heavy chain (eMyHC) is expressed at a higher level in newly formed myofibers but disappeared when fibers are mature [162]. We stained eMyHC at day 10 and day 30 of IS and ID muscle for myoblasts differentiation characterization. At 10 dpi, eMyHC presented in many small-caliber myofibers in IS mice. Almost all the eMyHC diminished upon 30 dpi. On the contrary, the ID muscle exhibited less eMyHC at 10 dpi (**Figure 3.3D**), but more visible eMyHC positive myofibers at 30 dpi. The result indicates the delayed maturation of ID muscle (**Figure 3.3D**). To determine the self-renewal capacity of ID muscle, we stained Pax7 of IS and ID TA muscle at 30 dpi. As displayed in Figure 3E, the number of Pax7 SCs was comparable between IS and ID

muscle, suggesting that the mild iron deficiency does not affect SCs self-renewal. All these results suggest that iron is essential for muscle repair.

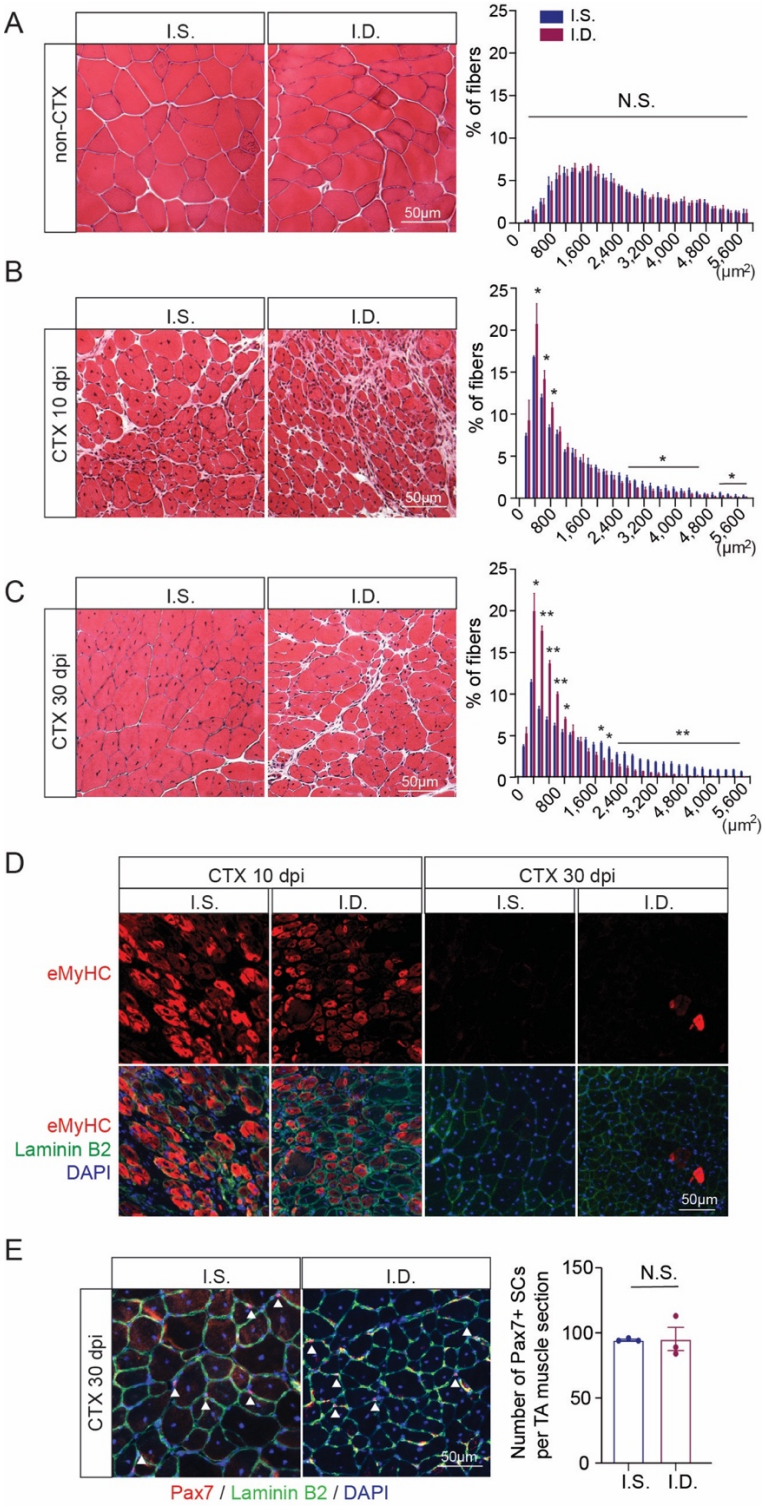

Figure 3.3. Iron deficiency impairs skeletal muscle regeneration

A. Representative images of the H&E staining and distribution of the fiber cross-sectional area of undamaged TA cross-section from iron sufficient (I.S.) and iron deficient (I.D.) mice (N=3).

B. Representative images of the H&E staining and distribution of the fiber cross-sectional area of TA cross-section at 10 dpi from iron sufficient (I.S.) and iron deficient (I.D.) mice (N=3).

C. Representative images of the H&E staining and distribution of the fiber cross-sectional area of TA cross-section at 30 dpi from iron sufficient (I.S.) and iron deficient (I.D.) mice (N=3).

D. Representative eMyHC (red) and Laminin B2 (green) immunofluorescence images of TA section at 10 dpi and 30 dpi from iron sufficient (I.S.) and iron deficient (I.D.) mice.

E. Representative images of Pax7 (red), Laminin B2 (green) and DAPI (blue) staining and the number of Pax7 positive SCs per TA muscle cross-section at 30 dpi from iron sufficient (I.S.) and iron deficient (I.D.) mice (N=3).

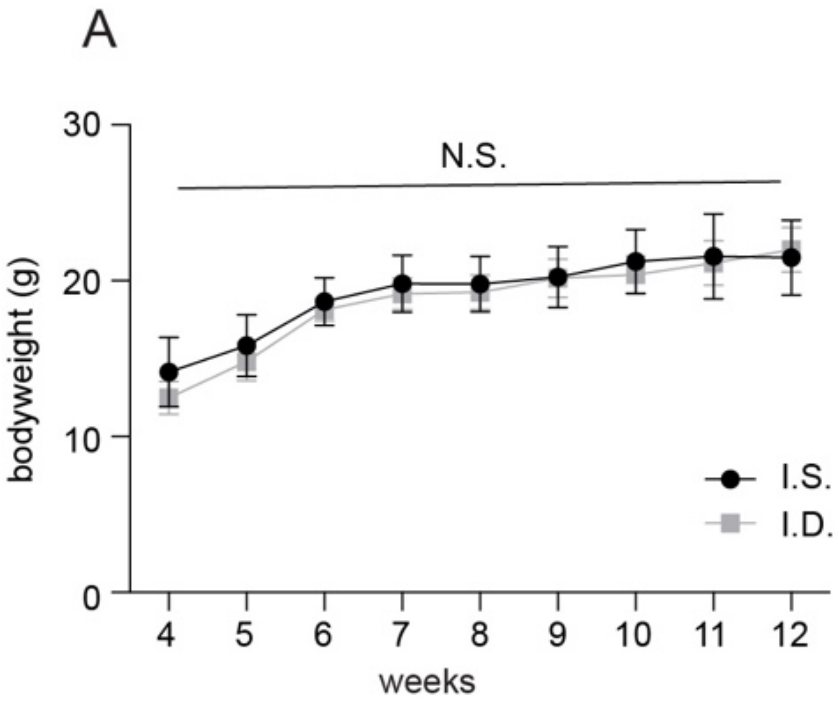

Figure S3.3. Supplementary_Iron deficiency impairs skeletal muscle regeneration

A. Bodyweight curve of IS and ID mice during iron sufficient and iron deficient chow feeding.

Iron depletion-induced HIF2α stabilization blocks the myoblasts proliferation

Iron is one of the known factors that participate in the stability regulation of hypoxia-inducible protein (HIFα). A decrease in cellular iron availability inhibits PHD-dependent proline hydroxylation of HIF α subunits, resulting in the failure of von Hippel-Lindau tumor suppressor protein (VHL) binding to HIFα subunits for degradation [8]. A previous study from our group revealed that transient HIF2α knockout improves muscle regeneration [101]. We hypothesized that HIF2α plays a critical role in iron deprivation-induced proliferation blockage.

To prove this, we first examined whether HIF2α is stabilized in satellite cells upon iron depletion. We co-stained the CTX 10 dpi TA muscle section with HIF2α and Pax7 of IS and ID mice. Three populations of cells were HIF2α positive in TA section: mononuclear immune cells, myocytes and Pax7+ SCs (**Figure 3.4A**). Both IS and ID TA muscle showed the positive staining of HIF2α in the mononuclear immune cells (**white triangle in Figure 3.4A**). However, only ID muscle had myonuclear HIF2α accumulation (**white star in Figure 3.4A**). As for Pax7+ SCs, most of the Pax7+ cells were HIF2α negative in IS mice, which echoes previous study from our lab that HIF2α is downregulated in activated satellite cells [101]. The ~22% HIF2α positive satellite cells could be self-renewing satellite cells. However, approximately ~ 84% of Pax7+ cells in ID muscle had nuclear staining for HIF2α (**white circle in Figure 3.4A**). The result indicates increased HIF2α stabilization in SCs of ID muscle. Consistently, in cultured BPD-treated C2C12 myoblasts, there was a notable accumulation of HIF2α in the nuclear, whereas vehicle control showed limited expression of HIF2α with peri-nuclei pattern (**Figure 3.4B**). We confirmed the augmented HIF2α in BPD-treated myoblasts by immunoblot. In both total and nuclear lysate, the protein of HIF2α in BPD-treated myoblasts was higher than in the vehicle control (**Figure 3.4C**).

To investigate whether the abnormal accumulated HIF2α in the nuclear is a causative factor for proliferation inhibition, we utilized HIF2α inhibitor, PT-2385 [163], to treat together with BPD on myoblasts. Notably, PT-2385 treated myoblast can significantly ameliorate the proliferation inhibition induced by BPD (**Figure 3.4D**). The Edu incorporation also supported the fact that HIF2α inhibition rescued the proliferation of BPD-treated myoblasts (**Figure 3.4E**). We further administered PT-2385 in the injured muscle of ID mice to examine the beneficial effect on proliferation *in vivo* (**Figure 3.4F**). Consistently, we found that PT-2385 could promote the number of both Pax7+ (**Figure 3.4G**) and Pa7+Ki67+ (**Figure 3.4H**) satellite cells. Collectively, these data suggest that iron deprivation stabilizes HIF2α, which mediate the inhibition of proliferation.

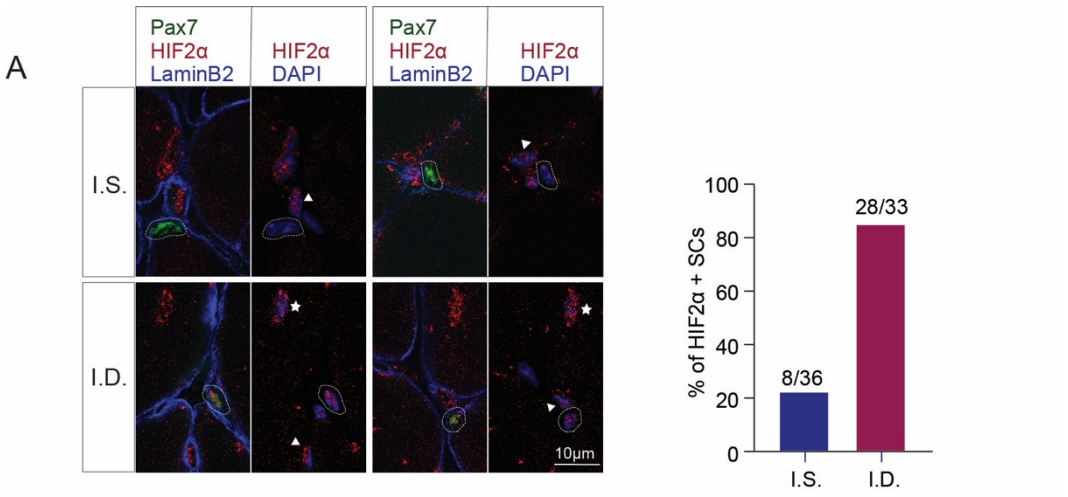
A
Pax7
HIF2α
LaminB2
HIF2α
DAPI
Pax7
HIF2α
LaminB2
HIF2α
DAPI
I.S.
I.D.
10μm
% of HIF2α + SCs
100
80
60
40
20
0
28/33
8/36
I.S.
I.D.

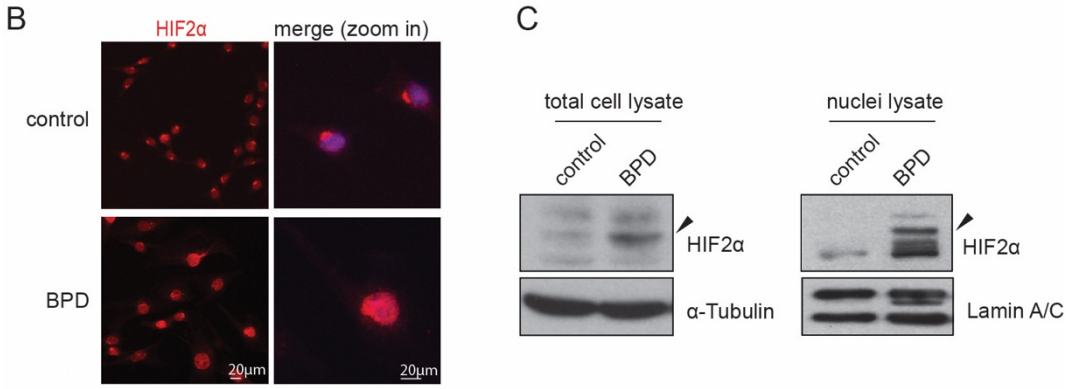
B
HIF2α
merge (zoom in)
control
BPD
20μm
20μm
C
total cell lysate
nuclei lysate
control
BPD
control
BPD
HIF2α
HIF2α
α-Tubulin
Lamin A/C

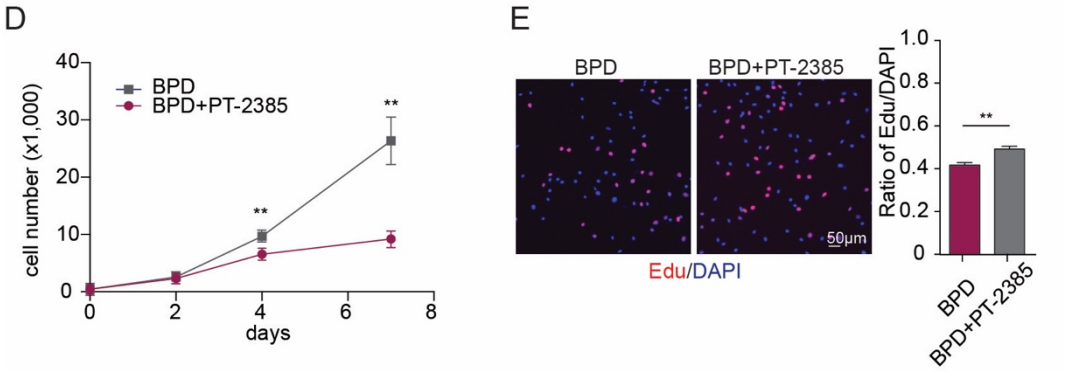
D
cell number (x1,000)
40
30
20
10
0
BPD
BPD+PT-2385
**
**
0
2
4
6
8
days
E
BPD
BPD+PT-2385
50μm
Edu/DAPI
Ratio of Edu/DAPI
1.0
0.8
0.6
0.4
0.2
0
**
BPD
BPD+PT-2385

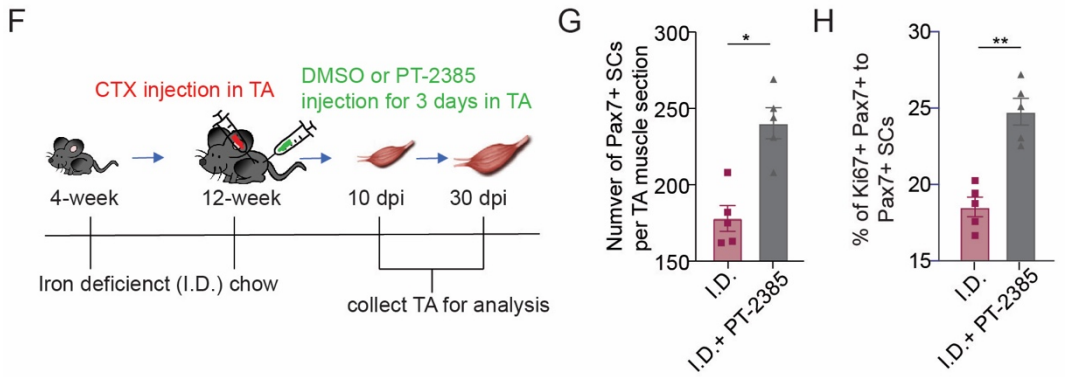
F
CTX injection in TA
DMSO or PT-2385
injection for 3 days in TA
4-week
12-week
10 dpi
30 dpi
Iron deficienct (I.D.) chow
collect TA for analysis
G
Numver of Pax7+ SCs
per TA muscle section
300
250
200
150
*
I.D.
I.D.+ PT-2385
H
% of Ki67+ Pax7+ to
Pax7+ SCs
30
25
20
15
**
I.D.
I.D.+ PT-2385

Figure 3.4. Iron depletion-induced HIF2α stabilization blocks the myoblasts proliferation

A. Representative HIF2α (red), Pax7 (green), Laminin B2 (purple) or DAPI (purple) immunofluorescence images and quantification of HIF2α positive SCs of TA section at 10 dpi from iron sufficient (I.S.) and iron deficient (I.D.) mice.
B. Representative images of HIF2α (red) and DAPI (blue) staining of control (DMSO) and BPD-treated C2C12 myoblasts.
C. Immunoblot showing higher level of HIF2α in whole-cell lysate and nuclei fraction lysate of BPD-treated myoblasts.
D. Proliferation curve of BPD and BPD and PT-2385 co-treated C2C12 myoblasts.
E. Representative images of Edu labeling and quantification of the ratio of Edu positive cells to DAPI positive cells of BPD and BPD and PT-2385 co-treated C2C12 myoblasts.
F. Timeline of PT-2385 administration and CTX-induced muscle injury in iron deficient mice.
G. Number of Pax7 positive SCs per TA section at 10 dpi in TA muscle of iron sufficient (I.S.) and iron deficient (I.D.) mice (N=5).
H. The ratio of Pax7 and Ki67 double positive SCs to all Pax7 positive SCs per section at 10 dpi in TA muscle of iron sufficient (I.S.) and iron deficient (I.D.) mice (N=5).

HIF2α represses the expression of E2F targets via targeting Rb1

To investigate whether HIF2α is sufficient for repressing proliferation, we overexpressed HIF2α in C2C12 myoblasts. Since HIF2α is unstable at normal oxygen level (21%), we overexpressed a mutated form of HIF2α (P405A/P530V/N851A), also called HIF2αTM, with which HIF2α can be stably expressed. We established an inducible overexpression of HIF2α in which HIF2αTM was cloned into a tet-on system combined with lentivirus infection on C2C12.

We named the cells without doxycycline WT and doxycycline-treated myoblasts HIF2α OE. The immunoblot result confirmed that HIF2α was induced by doxycycline (**Figure S3.5A**). We noticed that HIF2α was mainly expressed in the nuclei after doxycycline treatment (**Figure 3.5A**), which is similar to BPD treated myoblasts. The proliferation curve and Edu labeling also showed repression of proliferation after HIF2α was overexpressed in myoblasts (**Figure 3.5B** and **S3.5B**). To further identify whether the antiproliferation effect induced by HIF2α was associated with cell cycle arrest, we stained WT and HIF2αOE cells with propidium iodide (PI) and ran FACS for quantification. As showed in **Figure 3.5C**, comparing to WT (G0/G1 phase of 57.7%), there were more HIF2α myoblasts stuck at G0/G1 phase with the percentage of 70.2%. Correspondingly, the percentage of HIF2α OE cells at S phase and G2/M phase were smaller. The result suggests that HIF2α overexpression induces a block of the cell cycle at G0/G1 phase.

In order to gain insight into how HIF2α blocks proliferation at the transcriptomic level, we collected RNA from WT and HIF2α OE myoblasts and performed RNA sequencing. Expectedly, mRNA of Epas1 and our previous reported HIF2α targets [101]: *Atp7a*, *Cav1*, *Vegfa* were displayed in the up-regulated genes group (**Figure S3.5C**). To determine the biological processes that were specifically enhanced by HIF2α overexpression, we performed Gene Set Enrichment Analysis (GSEA) using Hallmark gene sets. As expected, hypoxia and several inflammatory pathways were enriched in the gene sets up-regulated by HIF2α. Specifically, we noticed the top set downregulated by HIF2α, "E2F TARGETS" (**Figure 3.5D** and **Figure 3.5E**). E2F transcription factors are well known for their role in controlling cell cycle progression. E2F1, E2F2 and E2F3 belong to a subclass of E2F factors thought to act as transcriptional activators that are essential for progression through the G1/S transition [164, 165]. Heatmap of E2F targets exhibited the inhibition of E2F targets by HIF2α overexpression, and PT-2385 could fully rescue the repression

of E2F targets (**Figure 3.5F**). qPCR confirmed that mRNA expression of representative E2F targets, *Ccna2*, *Ccnb1*, were repressed by HIF2α and could be rescued by PT-2385 (**Figure 3.5G**). Consistently, BPD treatment resulted in the same repression of E2F targets, which could again be partially rescued by PT-2385 (**Figure S3.5D**).

The retinoblastoma tumor suppressor (Rb) pathway is believed to have a critical role in regulating E2F activities and controlling cellular proliferation [166]. We tend to investigate if HIF2α targets *Rb1* for E2F target repression. We first compared the mRNA of *Rb1* in WT and HIF2α OE myoblast. Notably, the mRNA of *Rb1* was induced upon HIF2α OE (**Figure 3.5H**). Moreover, PT-2385 could reduce *Rb1*, which suggests the regulation of Rb1 is associated with the transcription activity of HIF2α. Consistently, BPD-treated myoblasts expressed a higher mRNA level of Rb1 (**Figure S3.5E**). To further determine whether *Rb1* is a direct target for HIF2α, we performed ChIP-qPCR using HIF2α OE myoblasts. We first confirmed the enrichment of known HIF2α targets, *Vegfa* and *Cav1* (**Figure S3.5F**). HIF proteins were reported to binds hypoxia-responsive elements (HREs) (5′-RCGTG-3′) and activate target gene expression. We checked the promoter region of Rb1 and found a conserved HRE sequence (**Figure S3.5G**). So we designed primers flanking the HRE region and performed ChIP-qPCR. The result exhibited the enrichment of HRE-containing region at *Rb1* promoter in HIF2α pull down comparing with IgG control (**Figure 3.5I**). Rb1 was reported to interact with histone deacetylase to repress transcription [167, 168]. To test whether the acetylation of E2F targets is changed associating with HIF2α, we performed ChIP with transcriptional activation histone marker H3K27ac in WT and HIF2α OE myoblasts. We detected the enrichment of H3K27ac at the promoter of E2F targets: *Ccna2*, *Ccnb*1, *Cdk2* and *Cdc25a*. The promoter region of *Vegfa* was include as a positive control (**Figure S3.5H**). As shown in Figure 3.5 J, there was a significant decrease of H3K27ac at the promoter region of

E2F targets upon HIF2α overexpression. To test the engagement of Rb1 in proliferation repression induced by HIF2α, we knocked down Rb1 utilizing Rb1 siRNA. We observed a higher proliferation rate after *Rb1* was knocked down (**Figure 3.5K**). Meanwhile, the mRNA of representative E2F targets was promoted in the Rb1 siRNA sample comparing with control siRNA (**Figure 3.5L**). In summary, HIF2α directly targeted the transcription of *Rb1*, further repressed the E2F targets for proliferation inhibition.

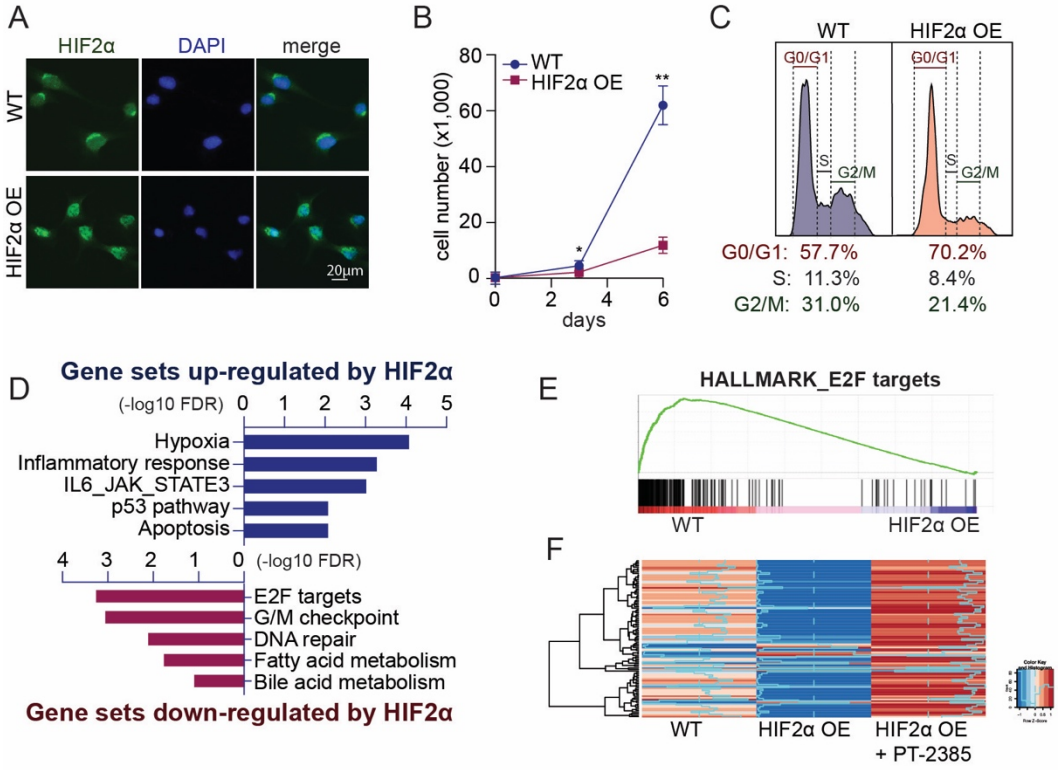
A
HIF2α
DAPI
merge
WT
HIF2α OE
20μm
B
WT
HIF2α OE
cell number (x1,000)
days
C
WT
HIF2α OE
G0/G1
S
G2/M
G0/G1: 57.7% 70.2%
S: 11.3% 8.4%
G2/M: 31.0% 21.4%
D
Gene sets up-regulated by HIF2α
(-log10 FDR)
Hypoxia
Inflammatory response
IL6_JAK_STATE3
p53 pathway
Apoptosis
E2F targets
G/M checkpoint
DNA repair
Fatty acid metabolism
Bile acid metabolism
Gene sets down-regulated by HIF2α
E
HALLMARK_E2F targets
WT
HIF2α OE
F
WT
HIF2α OE
HIF2α OE
+ PT-2385

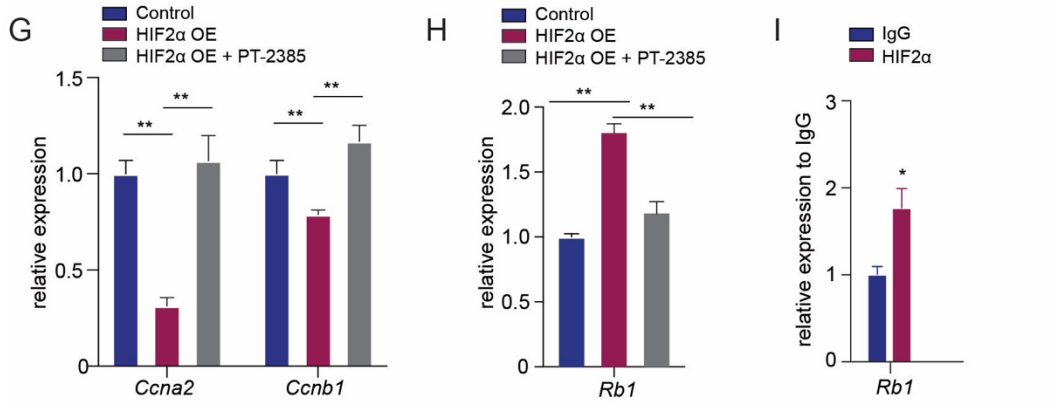
G
Control
HIF2α OE
HIF2α OE + PT-2385
relative expression
Ccna2
Ccnb1
H
Control
HIF2α OE
HIF2α OE + PT-2385
relative expression
Rb1
I
IgG
HIF2α
relative expression to IgG
Rb1

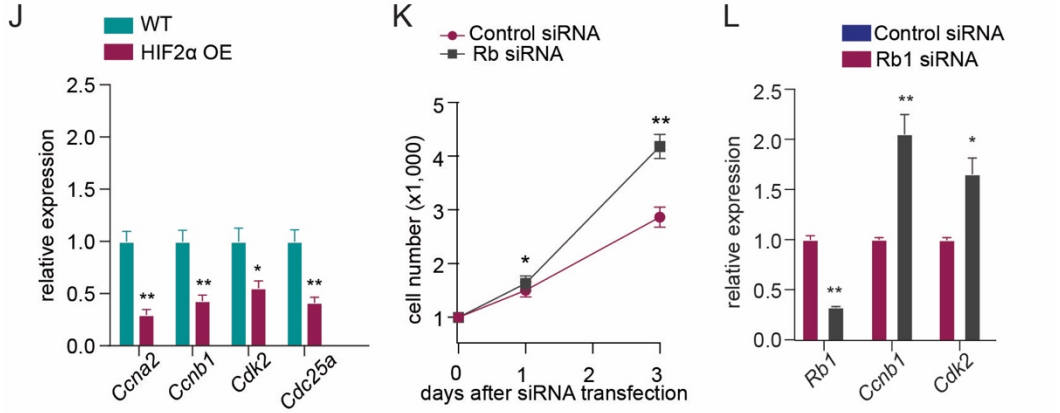
J
WT
HIF2α OE
relative expression
Ccna2
Ccnb1
Cdk2
Cdc25a
K
Control siRNA
Rb siRNA
cell number (x1,000)
days after siRNA transfection
L
Control siRNA
Rb1 siRNA
relative expression
Rb1
Ccnb1
Cdk2

Figure 3.5. HIF2α represses the expression of E2F targets via targeting Rb1

A. Representative images of HIF2α (green) and DAPI (blue) staining of WT (no dox) and HIF2α OE (dox) C2C12 myoblasts.
B. Proliferation curve of WT and HIF2α OE C2C12 myoblasts.
C. Flow cytometry analysis of cell cycle distribution of WT and HIF2α OE C2C12 myoblasts.
D. Gene set enrichment analysis (GSEA) showing genesets that are positively (blue) and negatively (red) enriched in HIF2α OE myoblasts.
E. GSEA enrichment plot for hallmark E2F_targets.
F. Heatmap depicting the expression of E2F Targets pathway genes in WT, HIF2α OE and HIF2α OE myoblasts treated by PT-2385.
G. RT-qPCR of representative E2F targets: Ccna2 and Ccnb1 in myoblasts of WT, HIF2α OE and HIF2α OE treated by PT-2385.
H. RT-qPCR of Rb1 in myoblasts of WT, HIF2α OE and HIF2α OE treated by PT-2385.
I. ChIP-qPCR analysis for HIF2α occupancy in the HRE-containing promoter region of Rb1. Known HIF2α targets Vegfa and Cav1 serve as positive control.
J. ChIP-qPCR analysis for histone modification marker H3K27ac occupancy in the promoter region of representative E2F targets: Ccna2, Ccnb1, Cdk2, Cdc25a in WT and HIF2α OE myoblasts. Known HIF2α targets Vegfa serves as positive control.
K. Proliferation curve of HIF2α OE myoblasts treated by control siRNA and Rb1 siRNA.
L. RT-qPCR of representative E2F targets: Ccnb1 and Cdk2 in HIF2α OE myoblasts treated by control siRNA and Rb1 siRNA.

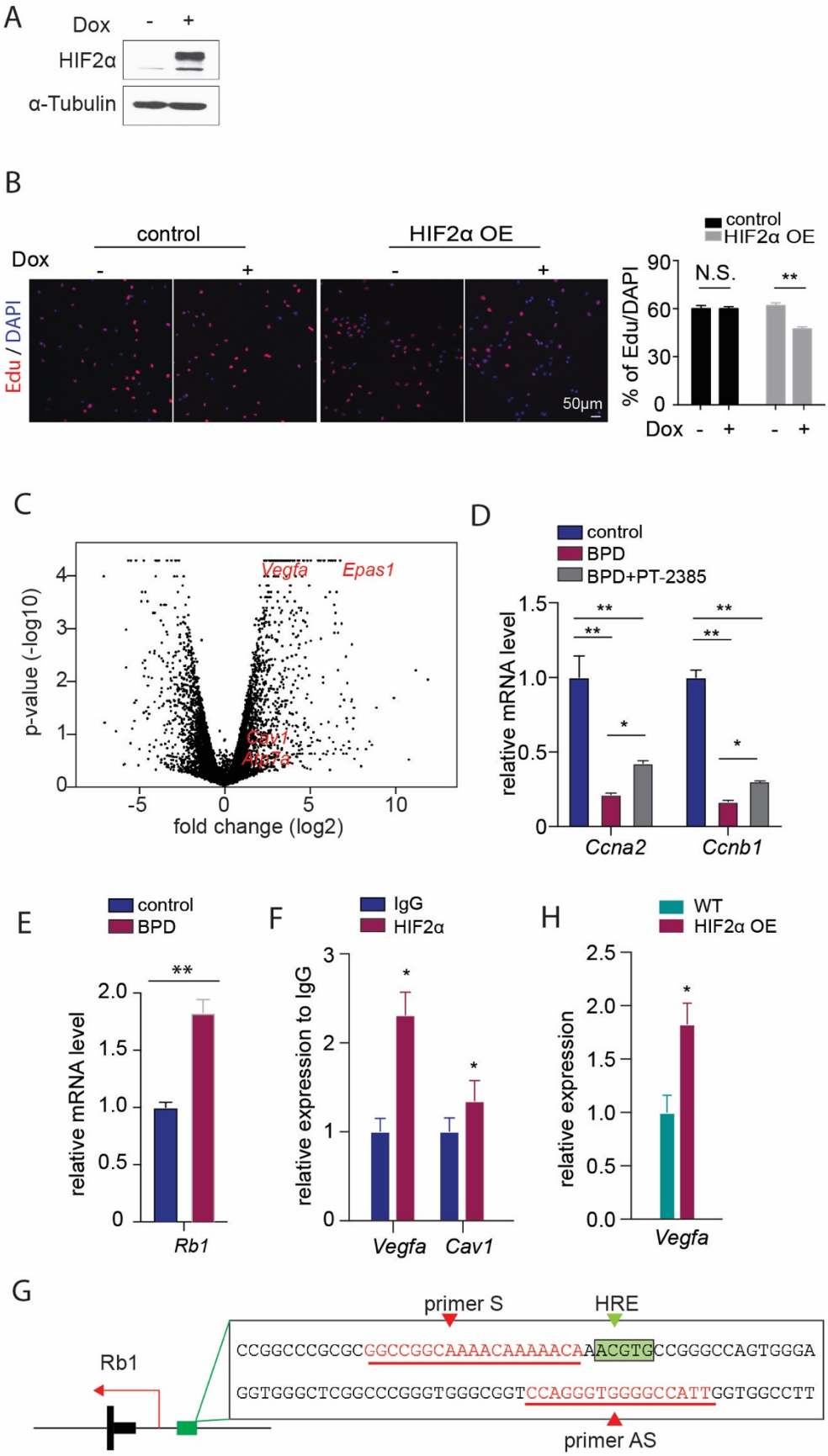
A
Dox - +
HIF2α
α-Tubulin
B
control
HIF2α OE
Dox - + - +
Edu / DAPI
50μm
control
HIF2α OE
% of Edu/DAPI
N.S.
**
Dox - + - +
C
Vegfa
Epas1
Cav1
Arg2
p-value (-log10)
fold change (log2)
D
control
BPD
BPD+PT-2385
relative mRNA level
Ccna2
Ccnb1
E
control
BPD
relative mRNA level
Rb1
F
IgG
HIF2α
relative expression to IgG
Vegfa
Cav1
H
WT
HIF2α OE
relative expression
Vegfa
G
primer S
HRE
Rb1
CCGGCCCGCGCGGCCGGCAAAACAAAAACAAACGTGCCGGGCCAGTGGGA
GGTGGGCTCGGCCCGGGTGGGCGGTCCAGGGTGGGGCCATTGGTGGCCTT
primer AS

Figure S3.5. Supplementary_HIF2α represses the expression of E2F targets via targeting Rb1

A. Immunoblot showing the stabilization of HIF2α after doxycycline treatment in HIF2α OE C2C12 myoblasts.
B. Representative images of Edu labeling and quantification of the ratio of Edu positive cells to DAPI positive cells of control and HIF2α OE myoblasts with and without doxycycline treatment.
C. A volcano plot showing RNA-seq results of WT and HIF2α OE myoblasts. Known HIF2α target genes (red) were displayed in the HIF2α OE group.
D. RT-qPCR of representative E2F targets: Ccna2 and Ccnb1 in control, BPD and BPD and PT-2385 co-treated myoblasts.
E. RT-qPCR of Rb1 in control and BPD-treated myoblasts.
F. ChIP-qPCR analysis for HIF2α occupancy in the promoter region of known targets: Vegfa and Cav1.
G. HRE-containing DNA sequence and primer design of Rb1 promoter region for ChIP-qPCR analysis.
H. ChIP-qPCR analysis for histone modification marker H3K27ac occupancy in the promoter region of Vegfa.

Transient pharmacological HIF2α inhibition improves muscle regeneration upon iron deficiency

Given the crucial role of HIF2α in mediating the proliferation repression by iron deprivation, we looked forward to the beneficial effect of HIF2α inhibitor on skeletal muscle regeneration. We

administered HIF2α inhibitor, PT-2385, into the TA muscle as shown in Figure 4. 10 days and 30 days after injury, we collected TA muscle for phenotype characterization. At 10 dpi and 30 dpi, comparing with ID mice, transient PT-2385 treated muscle contained regenerated myofibers of increased calibers (**Figure 3.6A** and **3.6B**). The expression of eMyHC was increased in PT-2385 treated myofibers at 10dpi and almost all eMyHC was diminished by 30 dpi, suggesting the acceleration of fiber maturation induced by PT-2385 (**Figure 3.6C**). At 30 dpi, both ID control and PT-2385 treated ID mice had a comparable number of Pax7+ SCs, indicating PT-2385 treatment does not change the self-renewal of SCs (**Figure 3.6D**). In general, transient HIF2α inhibition by PT-2385 accelerates the progression of regeneration in ID mice.

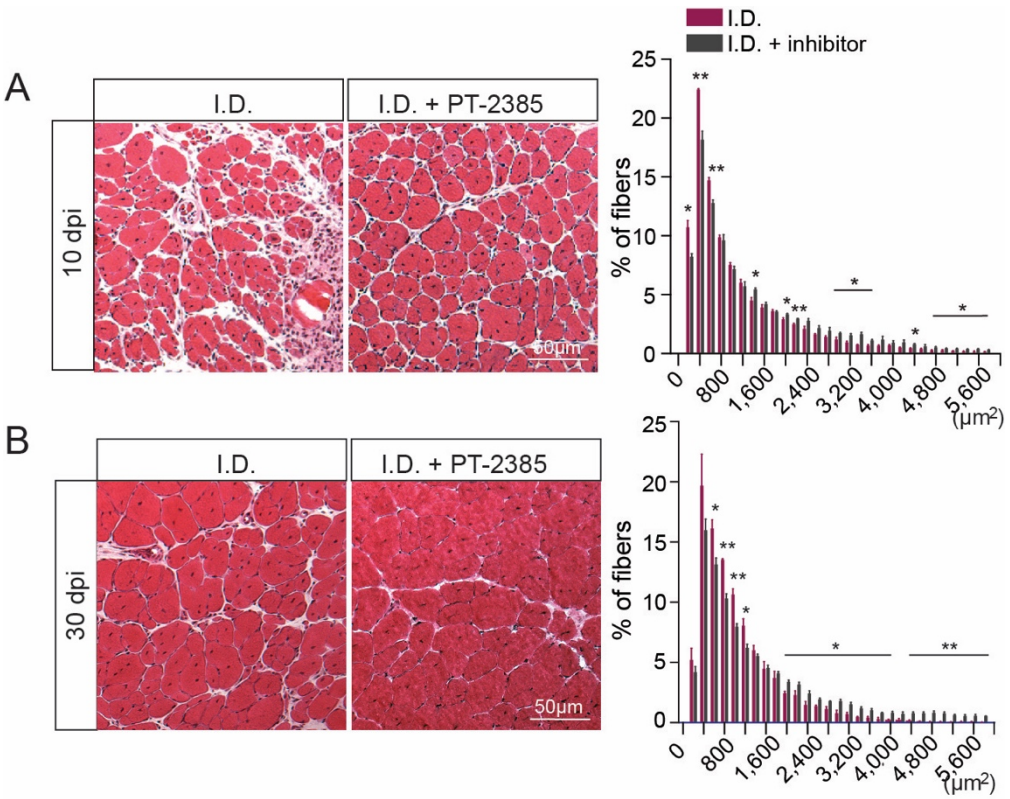
A
I.D.
I.D. + PT-2385
10 dpi
50μm
I.D.
I.D. + inhibitor
% of fibers
0
800
1,600
2,400
3,200
4,000
4,800
5,600
(μm²)
B
I.D.
I.D. + PT-2385
30 dpi
50μm
% of fibers
(μm²)

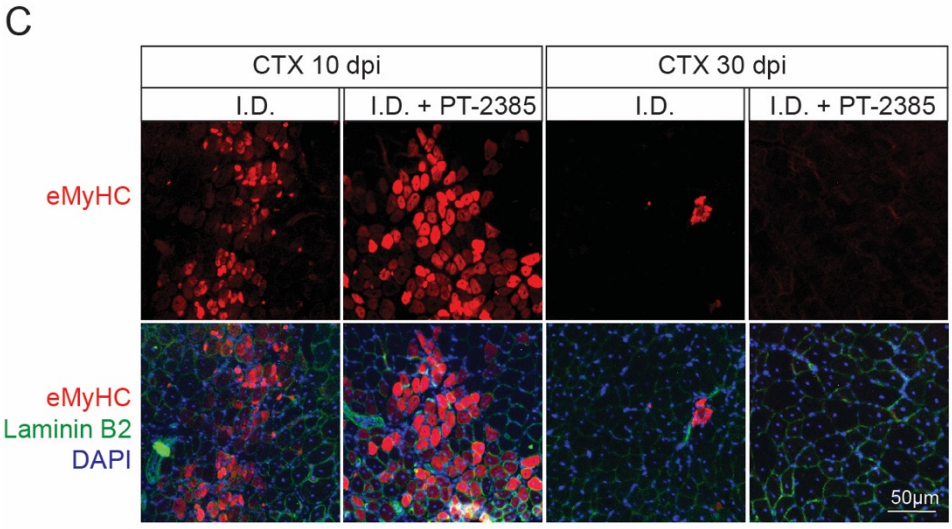
C
CTX 10 dpi
CTX 30 dpi
I.D.
I.D. + PT-2385
I.D.
I.D. + PT-2385
eMyHC
eMyHC
Laminin B2
DAPI
50μm

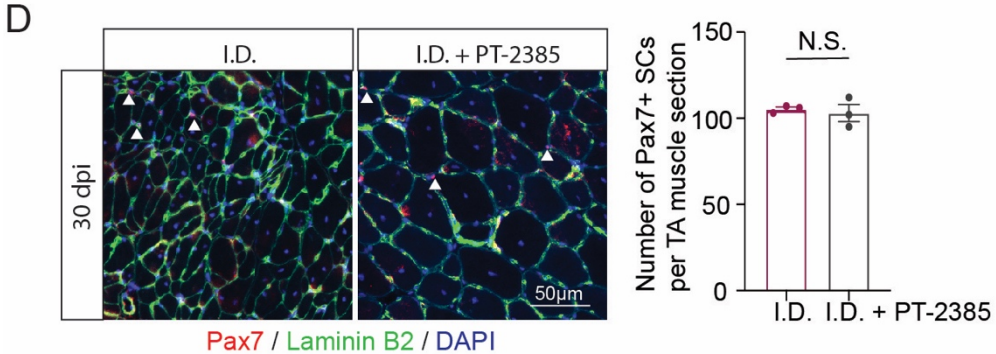
D
I.D.
I.D. + PT-2385
30 dpi
50μm
Pax7 / Laminin B2 / DAPI
Number of Pax7+ SCs per TA muscle section
N.S.
150
100
50
0
I.D.
I.D. + PT-2385

Figure 3.6. Transient pharmacological HIF2α inhibition improves muscle regeneration with iron deficiency

A. Representative images of the H&E staining and distribution of the fiber cross-sectional area of TA cross-section at 10 dpi from DMSO and PT-2385 treated iron deficient (I.D.) mice (N=3).
B. Representative images of the H&E staining and distribution of the fiber cross-sectional area of TA cross-section at 30 dpi from DMSO and PT-2385 treated iron deficient (I.D.) mice (N=3).
C. Representative eMyHC (red) and Laminin B2 (green) immunofluorescence images of TA section at 10 dpi and 30 dpi from DMSO and PT-2385 treated iron deficient (I.D.) mice.
D. Representative images of Pax7 (red), Laminin B2 (green) and DAPI (blue) staining and the number of Pax7 positive SCs per TA muscle cross-section at 30 dpi from DMSO and PT-2385 treated iron deficient (I.D.) mice (N=3).

3.5 Discussion

Satellite cells are skeletal muscle stem cells that are responsible for injury-induced skeletal muscle at adult age. The process of regeneration is accompanied by regulation of external nutrient factors, such as growth factor, amino acid, metals. Perturbation of either factor could result in impairment of regeneration [169-173]. Iron, an important trace metal, is involved in multiple biological processes. Our study is the first to directly investigate the effect of iron deprivation on skeletal muscle regeneration. Our data showed that iron is essential for satellite cell proliferation and skeletal muscle regeneration. Comparing to the starvation-induced quiescent stage, we observed more iron and iron-related genes in proliferating progenitor cells. Upon iron depletion, progenitor cells fail to proliferate, and skeletal muscle regeneration is jeopardized. Mechanistically, low iron stabilizes HIF2α. We first reveal the direct targeting of *Rb1* by HIF2α.

Inhibition of *Rb1* could partially rescue the proliferation repression induced by HIF2α overexpression. Fortunately, pharmacological inhibition of HIF2 by PT-2385 can rescue the impairment of injury-induced skeletal muscle regeneration.

Iron binds to transferrin and will be absorbed into the cell by binding to transferrin receptor 1(TfR1). Skeletal muscle-specific TfR1 knockout leads to iron deficiency in muscle and causes pathological changes in skeletal muscle, adipose tissue and liver [123]. Specifically, a recent study demonstrated that satellite cell-specific TfR1 knockout impedes muscle regeneration. TfR1 KO in satellite cells displayed irreversible depletion of satellite cells number and impairment of regeneration by ferroptosis [174]. Besides, iron recycling by macrophage was found to be critical for skeletal muscle regeneration [150]. Selective disruption of macrophage ferroportin (Fpn) results in iron accumulation within muscle-infiltrating macrophages and jeopardizes muscle healing, prompting fat accumulation. All of these studies support our conclusion that iron homeostasis is critical for the regeneration of skeletal muscle.

Iron homeostasis in satellite cells during skeletal muscle regeneration has not been extensively characterized, probably because of the technical issue of detecting iron ion in satellite cells. To investigate the change of iron between QSCs and ASCs, we first detected the mRNA level of iron-loading gene genes in QSCs and ASCs, and found the induction of Tfr1 in ASCs. Then we tried to explore the dynamic of iron status during regeneration utilizing an *in vitro* model by comparing the iron level in non-cycling myoblasts and cycling myoblast to mimic quiescent and activated proliferating satellite cells. Though it may not be the direct evidence to show the changes of iron ion in satellite cells, the results indicate more iron uptake in proliferating myoblasts.

Our data prove that iron deprivation stabilized HIF2α. HIF2α is sufficient for blocking proliferation via the canonical Rb/E2F axis. Iron is a critical component of mitochondrial electronic transport chain as well as several iron-sulfur mitochondrial enzymes and heme-containing mitochondrial enzymes. Iron deficiency leads to dysfunction of skeletal muscle via impairing the normal function of mitochondrial. However, satellite cells are skeletal muscle stem cells that display many stem- cell features. One of the features is the small number of mitochondria in satellite cells. After activation, comparing to newly formed myotube, activated proliferating cells contain a limited number of mitochondria and its energy source mainly comes from glycolysis for quick proliferation [151, 152]. Given this, we provide a mechanism to explain the defect of iron deficiency on proliferation and it is independent of mitochondria dysfunction. However, it is not deniable that mitochondria may also participate in the regulation of proliferation in the iron-depleted myoblasts. In glycolytic proliferating cells, even though functional limited, mitochondria are essential for normal proliferation [175]. They work by converting the diverse nutrients available to cells into the fundamental building blocks for cell growth [176, 177]. Aspartate is one of the blocks that found to be pivotal for proliferation regulation [177-180]. ETC inhibition failed to support the synthesis of aspartate, which is limiting for DNA and RNA synthesis, leading to proliferation impairment [177]. In addition, in myoblasts, electron transport chain (ETC) inhibition blocks proliferation by hindering aspartate synthesis and ultimately depletes asparagine, further activating the ISR via the eIF2α kinase GCN2. Besides, H_2O_2 generated by mitochondria work as signaling molecules to regulate proliferation [181-183]. Considering the fact that PT-2385 could partially not fully rescue the reduced proliferation by BPD treatment, it is possible that mitochondria dysfunction may play a part in the repression of proliferation induced by iron deprivation.

Our iron deficiency model is a relatively mild, not anemia level. The mild iron deficiency did not cause cell death of satellite cells. Given the experience of our BPD-treated myoblasts, a longer time or a higher concentration of BPD treatment may cause apoptosis of satellite cells. Consistently, *in vivo* satellite cells-specific knockout of TfR1 leads to irreversible depletion of satellite cells [174]. All of these suggest the possibility that long-time iron deficiency may cause irreversible damage to satellite cells that may not be rescued by iron repletion. However, transient HIF2α inhibition by PT-2385 could expand satellite numbers and accelerate the progression of regeneration. It gives us hope for the therapeutic implication in improving regeneration caused by severe iron deficiency.

Overall, this study reveals the function of iron in the proliferation of satellite cells and general skeletal muscle regeneration. We provide a novel explanation of which HIF2α is involved in regulating Rb/E2F pathway. Ultimately, we hope that pharmacological inhibition of HIF2α could be a potential therapeutic way to improve muscle regeneration of iron deficient patients.

CHAPTER 4

CONCLUDING REMARKS

The work here reveals the key roles of iron in brown adipocyte thermogenesis and skeletal muscle regeneration (**Figure 4**). To be specific, in brown adipose tissue, we found that brown adipocyte activation induces iron accumulation in a TfR1 dependent way. Deprivation of iron by TfR1 ablation or iron chelation dampens the thermogenic activity of brown adipocyte. In skeletal muscle stem cells (satellite cells), more iron accumulates in proliferating myoblasts, and it is required for myoblasts proliferation and skeletal muscle regeneration.

Iron is utilized in different cellular fraction for specific functions. Our work depicts the biology of iron in the mitochondrial of brown adipocyte and in the cytosol of satellite cells. During brown adipocyte activation, iron transports into mitochondria, catalyzes and engages in ROS (hydroxyl radical and lipid peroxidation) generation via Fenton's reaction. The ROS production are required for brown adipocyte activation.

In satellite cells, cytosolic iron participates in the stability regulation of HIF2α, which mediates the repression of proliferation. As a transcription factor, HIF2α binds to the HRE region of Rb1 and promotes its transcription, further repressing E2F targets for proliferation regulation.

Iron deficiency has been associated with cold tolerance and muscle weakness, which is associated with two organs: adipose tissue and skeletal muscle. Our work provides mechanistic evidence of the involvement of brown adipocyte and satellite cells in iron deficiency-related cold tolerance and muscle health, respectively. Furthermore, our study shows the beneficial effect of HIF2α inhibitor,

PT-2385, on the injury induced skeletal muscle regeneration in iron deficient mice, which could be a therapeutically target to iron deficient population.

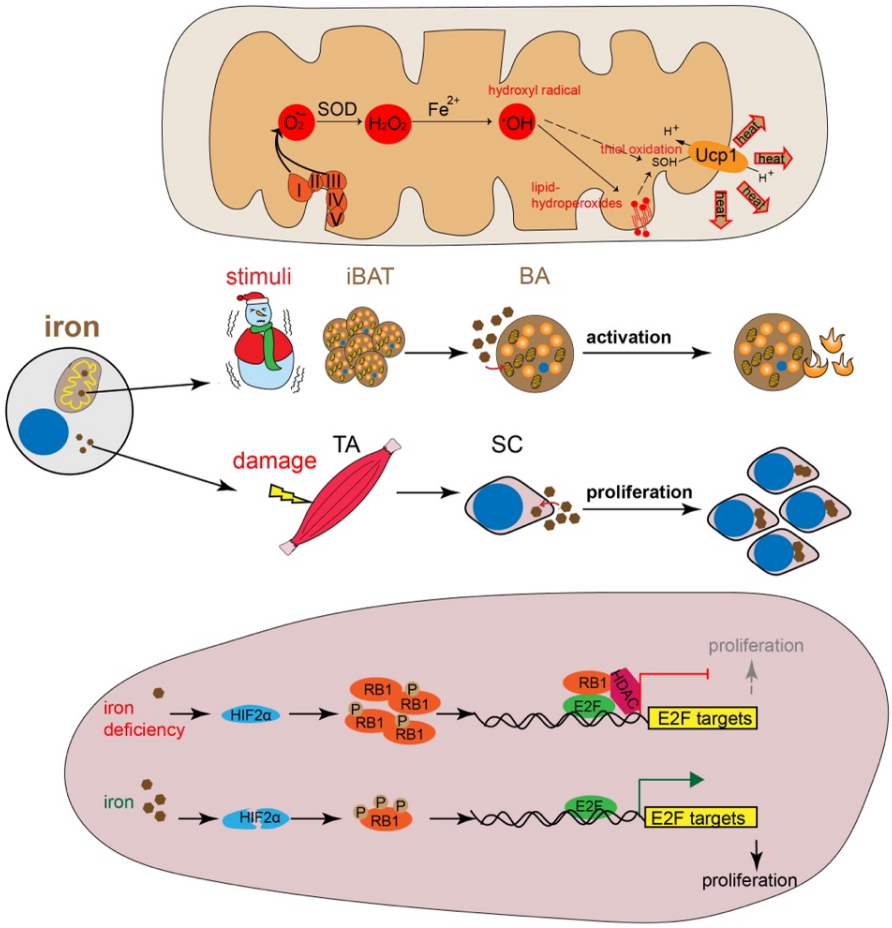

Figure 4. Illustration of the role of mitochondrial iron in brown adipocyte and cytosolic iron in satellite cell

REFERENCE

1. Shaw, G.C., et al., *Mitoferrin is essential for erythroid iron assimilation.* Nature, 2006. **440**(7080): p. 96-100.
2. Sheftel, A.D., et al., *Direct interorganellar transfer of iron from endosome to mitochondrion.* Blood, 2007. **110**(1): p. 125-32.
3. Hamanaka, R.B. and N.S. Chandel, *Mitochondrial reactive oxygen species regulate cellular signaling and dictate biological outcomes.* Trends Biochem Sci, 2010. **35**(9): p. 505-13.
4. Guo, B., et al., *Iron regulates the intracellular degradation of iron regulatory protein 2 by the proteasome.* J Biol Chem, 1995. **270**(37): p. 21645-51.
5. Guo, B., Y. Yu, and E.A. Leibold, *Iron Regulates Cytoplasmic Levels of a Novel Iron-Responsive Element-Binding Protein without Aconitase Activity.* Journal of Biological Chemistry, 1994. **269**(39): p. 24252-24260.
6. Samaniego, F., et al., *Molecular characterization of a second iron-responsive element binding protein, iron regulatory protein 2. Structure, function, and post-translational regulation.* J Biol Chem, 1994. **269**(49): p. 30904-10.
7. Salahudeen, A.A., et al., *An E3 Ligase Possessing an Iron-Responsive Hemerythrin Domain Is a Regulator of Iron Homeostasis.* Science, 2009. **326**(5953): p. 722-726.
8. Epstein, A.C.R., et al., *C-elegans EGL-9 and mammalian homologs define a family of dioxygenases that regulate HIF by prolyl hydroxylation.* Cell, 2001. **107**(1): p. 43-54.
9. Thompson, J.W. and R.K. Bruick, *Protein degradation and iron homeostasis.* Biochim Biophys Acta, 2012. **1823**(9): p. 1484-90.
10. Nandal, A., et al., *Activation of the HIF prolyl hydroxylase by the iron chaperones PCBP1 and PCBP2.* Cell Metab, 2011. **14**(5): p. 647-57.
11. Sheftel, A., O. Stehling, and R. Lill, *Iron-sulfur proteins in health and disease.* Trends Endocrinol Metab, 2010. **21**(5): p. 302-14.
12. Zhang, C., *Essential functions of iron-requiring proteins in DNA replication, repair and cell cycle control.* Protein Cell, 2014. **5**(10): p. 750-60.
13. Harms, M. and P. Seale, *Brown and beige fat: development, function and therapeutic potential.* Nat Med, 2013. **19**(10): p. 1252-63.
14. Cypess, A.M., et al., *Identification and importance of brown adipose tissue in adult humans.* N Engl J Med, 2009. **360**(15): p. 1509-17.
15. Wu, J., et al., *Beige adipocytes are a distinct type of thermogenic fat cell in mouse and human.* Cell, 2012. **150**(2): p. 366-76.
16. Sharp, L.Z., et al., *Human BAT Possesses Molecular Signatures That Resemble Beige/Brite Cells.* Plos One, 2012. **7**(11).
17. Lidell, M.E., et al., *Evidence for two types of brown adipose tissue in humans.* Nat Med, 2013. **19**(5): p. 631-4.
18. Saito, M., et al., *High incidence of metabolically active brown adipose tissue in healthy adult humans: effects of cold exposure and adiposity.* Diabetes, 2009. **58**(7): p. 1526-31.

19. van der Lans, A.A., et al., *Cold acclimation recruits human brown fat and increases nonshivering thermogenesis.* J Clin Invest, 2013. **123**(8): p. 3395-403.
20. Lee, P., et al., *Temperature-acclimated brown adipose tissue modulates insulin sensitivity in humans.* Diabetes, 2014. **63**(11): p. 3686-98.
21. Cypess, A.M., et al., *Activation of human brown adipose tissue by a beta3-adrenergic receptor agonist.* Cell Metab, 2015. **21**(1): p. 33-8.
22. Beard, J.L., M.J. Borel, and J. Derr, *Impaired thermoregulation and thyroid function in iron-deficiency anemia.* Am J Clin Nutr, 1990. **52**(5): p. 813-9.
23. Lukaski, H.C., C.B. Hall, and F.H. Nielsen, *Thermogenesis and thermoregulatory function of iron-deficient women without anemia.* Aviat Space Environ Med, 1990. **61**(10): p. 913-20.
24. Martinez-Torres, C., et al., *Effect of exposure to low temperature on normal and iron-deficient subjects.* Am J Physiol, 1984. **246**(3 Pt 2): p. R380-3.
25. Rosenzweig, P.H. and S.L. Volpe, *Iron, thermoregulation, and metabolic rate.* Crit Rev Food Sci Nutr, 1999. **39**(2): p. 131-48.
26. Yook, J.S., et al., *Dietary Iron Deficiency Modulates Adipocyte Iron Homeostasis, Adaptive Thermogenesis, and Obesity in C57BL/6 Mice.* J Nutr, 2021. **151**(10): p. 2967-2975.
27. Qiu, J., et al., *Transferrin Receptor Functionally Marks Thermogenic Adipocytes.* Front Cell Dev Biol, 2020. **8**: p. 572459.
28. Li, J., et al., *Transferrin Receptor 1 Regulates Thermogenic Capacity and Cell Fate in Brown/Beige Adipocytes.* Adv Sci (Weinh), 2020. **7**(12): p. 1903366.
29. Yook, J.S., et al., *The thermogenic characteristics of adipocytes are dependent on the regulation of iron homeostasis.* J Biol Chem, 2021. **296**: p. 100452.
30. Yook, J.S., et al., *Essential role of systemic iron mobilization and redistribution for adaptive thermogenesis through HIF2-alpha/hepcidin axis.* Proc Natl Acad Sci U S A, 2021. **118**(40).
31. Bai, N., et al., *Bola3 Regulates Beige Adipocyte Thermogenesis via Maintaining Mitochondrial Homeostasis and Lipolysis.* Front Endocrinol (Lausanne), 2020. **11**: p. 592154.
32. Turchi, R., et al., *Frataxin deficiency induces lipid accumulation and affects thermogenesis in brown adipose tissue.* Cell Death Dis, 2020. **11**(1): p. 51.
33. Blankenhaus, B., et al., *Ferritin regulates organismal energy balance and thermogenesis.* Mol Metab, 2019. **24**: p. 64-79.
34. Galmozzi, A., et al., *PGRMC2 is an intracellular haem chaperone critical for adipocyte function.* Nature, 2019. **576**(7785): p. 138-142.
35. Matthias, A., et al., *Thermogenic responses in brown fat cells are fully UCP1-dependent. UCP2 or UCP3 do not substitute for UCP1 in adrenergically or fatty scid-induced thermogenesis.* J Biol Chem, 2000. **275**(33): p. 25073-81.
36. Boulton, F.E., *The myoglobin content of human skeletal muscle.* Br J Haematol, 1973. **25**(2): p. 281.
37. McLane, J.A., et al., *Physiological and biochemical effects of iron deficiency on rat skeletal muscle.* Am J Physiol, 1981. **241**(1): p. C47-54.
38. Ohira, Y., et al., *Oxygen consumption and work capacity in iron-deficient anemic rats.* J Nutr, 1981. **111**(1): p. 17-25.

39. Brownlie, T., et al., *Tissue iron deficiency without anemia impairs adaptation in endurance capacity after aerobic training in previously untrained women.* American Journal of Clinical Nutrition, 2004. **79**(3): p. 437-443.
40. Celsing, F., et al., *Effects of Iron-Deficiency on Endurance and Muscle Enzyme-Activity in Man.* Medicine and Science in Sports and Exercise, 1986. **18**(2): p. 156-161.
41. Tkaczyszyn, M., et al., *Depleted iron stores are associated with inspiratory muscle weakness independently of skeletal muscle mass in men with systolic chronic heart failure.* J Cachexia Sarcopenia Muscle, 2018. **9**(3): p. 547-556.
42. Brownlie, T., et al., *Marginal iron deficiency without anemia impairs aerobic adaptation among previously untrained women. (vol 75, pg 734, 2002).* American Journal of Clinical Nutrition, 2004. **79**(2): p. 343-343.
43. Hinton, P.S., et al., *Iron supplementation improves endurance after training in iron-depleted, nonanemic women.* Journal of Applied Physiology, 2000. **88**(3): p. 1103-1111.
44. Ackrell, B.A., et al., *Effect of iron deficiency on succinate- and NADH-ubiquinone oxidoreductases in skeletal muscle mitochondria.* J Biol Chem, 1984. **259**(16): p. 10053-9.
45. Hagler, L., et al., *Influence of Dietary Iron-Deficiency on Hemoglobin, Myoglobin, Their Respective Reductases, and Skeletal-Muscle Mitochondrial Respiration.* American Journal of Clinical Nutrition, 1981. **34**(10): p. 2169-2177.
46. Maguire, J.J., et al., *Effects of dietary iron deficiency of iron-sulfur proteins and bioenergetic functions of skeletal muscle mitochondria.* Biochim Biophys Acta, 1982. **679**(2): p. 210-20.
47. Ohira, Y., et al., *Mitochondrial NADH dehydrogenase in iron-deficient and iron-repleted rat muscle: an EPR and work performance study.* Br J Haematol, 1982. **52**(4): p. 623-30.
48. Rineau, E., et al., *Iron Deficiency without Anemia Decreases Physical Endurance and Mitochondrial Complex I Activity of Oxidative Skeletal Muscle in the Mouse.* Nutrients, 2021. **13**(4).
49. Leermakers, P.A., et al., *Iron deficiency-induced loss of skeletal muscle mitochondrial proteins and respiratory capacity; the role of mitophagy and secretion of mitochondria-containing vesicles.* FASEB J, 2020. **34**(5): p. 6703-6717.
50. Merrill, J.F., et al., *Iron deficiency causes a shift in AMP-activated protein kinase (AMPK) subunit composition in rat skeletal muscle.* Nutr Metab (Lond), 2012. **9**(1): p. 104.
51. Higashida, K., S. Inoue, and N. Nakai, *Iron deficiency attenuates protein synthesis stimulated by branched-chain amino acids and insulin in myotubes.* Biochem Biophys Res Commun, 2020. **531**(2): p. 112-117.
52. Bolster, D.R., et al., *AMP-activated protein kinase suppresses protein synthesis in rat skeletal muscle through down-regulated mammalian target of rapamycin (mTOR) signaling.* J Biol Chem, 2002. **277**(27): p. 23977-80.
53. Winder, W.W., et al., *Activation of AMP-activated protein kinase increases mitochondrial enzymes in skeletal muscle.* J Appl Physiol (1985), 2000. **88**(6): p. 2219-26.
54. Xu, J., et al., *Iron accumulation with age, oxidative stress and functional decline.* PLoS One, 2008. **3**(8): p. e2865.

55. Xu, J.Z., et al., *Long-term perturbation of muscle iron homeostasis following hindlimb suspension in old rats is associated with high levels of oxidative stress and impaired recovery from atrophy.* Experimental Gerontology, 2012. **47**(1): p. 100-108.
56. Nakagawa, C., et al., *Association of Increased Serum Ferritin With Impaired Muscle Strength/Quality in Hemodialysis Patients.* J Ren Nutr, 2016. **26**(4): p. 253-7.
57. Reardon, T.F. and D.G. Allen, *Iron injections in mice increase skeletal muscle iron content, induce oxidative stress and reduce exercise performance.* Exp Physiol, 2009. **94**(6): p. 720-30.
58. Ikeda, Y., et al., *Iron-induced skeletal muscle atrophy involves an Akt-forkhead box O3-E3 ubiquitin ligase-dependent pathway.* J Trace Elem Med Biol, 2016. **35**: p. 66-76.
59. Moreno-Navarrete, J.M., et al., *Obesity Is Associated With Gene Expression and Imaging Markers of Iron Accumulation in Skeletal Muscle.* Journal of Clinical Endocrinology & Metabolism, 2016. **101**(3): p. 1282-1289.
60. Jahng, J.W.S., et al., *Iron overload inhibits late stage autophagic flux leading to insulin resistance.* EMBO Rep, 2019. **20**(10): p. e47911.
61. Lee, K., et al., *Iron Overload Plays an Important Role in ER Stress-Induced Insulin Resistance in Human Skeletal Muscle Cells.* Diabetes, 2018. **67**.
62. Cui, R., et al., *Iron overload by transferrin receptor protein 1 regulation plays an important role in palmitate-induced insulin resistance in human skeletal muscle cells.* Faseb Journal, 2019. **33**(2): p. 1771-1786.
63. Ikeda, Y., et al., *Iron accumulation causes impaired myogenesis correlated with MAPK signaling pathway inhibition by oxidative stress.* Faseb Journal, 2019. **33**(8): p. 9551-9564.
64. Zon, L.I., *Intrinsic and extrinsic control of haematopoietic stem-cell self-renewal.* Nature, 2008. **453**(7193): p. 306-313.
65. Morrison, S.J. and J. Kimble, *Asymmetric and symmetric stem-cell divisions in development and cancer.* Nature, 2006. **441**(7097): p. 1068-74.
66. Pazhanisamy, S.K., *Stem cells, DNA damage, ageing and cancer.* Hematol Oncol Stem Cell Ther, 2009. **2**(3): p. 375-84.
67. Han, Z.B., et al., *Iron overload inhibits self-renewal of human pluripotent stem cells via DNA damage and generation of reactive oxygen species.* Febs Open Bio, 2020. **10**(5): p. 726-733.
68. Muto, Y., et al., *Essential role of FBXL5-mediated cellular iron homeostasis in maintenance of hematopoietic stem cells.* Nat Commun, 2017. **8**: p. 16114.
69. Han, Z., et al., *Iron Homeostasis Determines Fate of Human Pluripotent Stem Cells Via Glycerophospholipids-Epigenetic Circuit.* Stem Cells, 2019. **37**(4): p. 489-503.
70. Liu, T.M., et al., *Ascorbate and Iron Are Required for the Specification and Long-Term Self-Renewal of Human Skeletal Mesenchymal Stromal Cells.* Stem Cell Reports, 2020. **14**(2): p. 210-225.
71. Wang, S., et al., *Transferrin receptor 1-mediated iron uptake plays an essential role in hematopoiesis.* Haematologica, 2020. **105**(8): p. 2071-2082.
72. Song, D., et al., *Effect of iron deficiency on c-kit(+) cardiac stem cells in vitro.* PLoS One, 2013. **8**(6): p. e65721.
73. Borriello, A., et al., *Iron overload enhances human mesenchymal stromal cell growth and hampers matrix calcification.* Biochim Biophys Acta, 2016. **1860**(6): p. 1211-23.

74. Chanvorachote, P. and S. Luanpitpong, *Iron induces cancer stem cells and aggressive phenotypes in human lung cancer cells.* Am J Physiol Cell Physiol, 2016. **310**(9): p. C728-39.
75. Liu, N., et al., *Enhanced proliferation and differentiation of HO-1 gene-modified bone marrow-derived mesenchymal stem cells in the acute injured kidney.* Int J Mol Med, 2018. **42**(2): p. 946-956.
76. Yamauchi, T., et al., *FBXL5 Inactivation in Mouse Brain Induces Aberrant Proliferation of Neural Stem Progenitor Cells.* Molecular and Cellular Biology, 2017. **37**(8).
77. Balogh, E., et al., *Iron overload inhibits osteogenic commitment and differentiation of mesenchymal stem cells via the induction of ferritin.* Biochim Biophys Acta, 2016. **1862**(9): p. 1640-9.
78. Zhang, Y., et al., *Effects of iron overload on the bone marrow microenvironment in mice.* PLoS One, 2015. **10**(3): p. e0120219.
79. Yang, F., et al., *Melatonin protects bone marrow mesenchymal stem cells against iron overload-induced aberrant differentiation and senescence.* J Pineal Res, 2017. **63**(3).
80. Mehta, K.J., *Role of iron and iron-related proteins in mesenchymal stem cells: Cellular and clinical aspects.* J Cell Physiol, 2021. **236**(10): p. 7266-7289.
81. Chai, X., et al., *ROS-mediated iron overload injures the hematopoiesis of bone marrow by damaging hematopoietic stem/progenitor cells in mice.* Sci Rep, 2015. **5**: p. 10181.
82. Jin, X., et al., *Iron overload impairs normal hematopoietic stem and progenitor cells through reactive oxygen species and shortens survival in myelodysplastic syndrome mice.* Haematologica, 2018. **103**(10): p. 1627-1634.
83. Lu, W., et al., *Free iron catalyzes oxidative damage to hematopoietic cells/mesenchymal stem cells in vitro and suppresses hematopoiesis in iron overload patients.* Eur J Haematol, 2013. **91**(3): p. 249-61.
84. Huang, L., et al., *Iron Overload Impairs Bone Marrow Mesenchymal Stromal Cells from Higher-Risk MDS Patients by Regulating the ROS-Related Wnt/beta-Catenin Pathway.* Stem Cells Int, 2020. **2020**: p. 8855038.
85. Nakajima, O., et al., *Heme deficiency in erythroid lineage causes differentiation arrest and cytoplasmic iron overload.* EMBO J, 1999. **18**(22): p. 6282-9.
86. Si, Z., et al., *Heme Oxygenase 1 Inhibits Adult Neural Stem Cells Proliferation and Survival via Modulation of Wnt/beta-Catenin Signaling.* J Alzheimers Dis, 2020. **76**(2): p. 623-641.
87. Cozzi, A., et al., *Stem Cell Modeling of Neuroferritinopathy Reveals Iron as a Determinant of Senescence and Ferroptosis during Neuronal Aging.* Stem Cell Reports, 2019. **13**(5): p. 832-846.
88. Lu, W.Y., et al., *[Effect and mechanism of iron-catalyzed oxidative stress on mesenchymal stem cells].* Zhongguo Yi Xue Ke Xue Yuan Xue Bao, 2013. **35**(1): p. 6-12.
89. Sart, S., L. Song, and Y. Li, *Controlling Redox Status for Stem Cell Survival, Expansion, and Differentiation.* Oxid Med Cell Longev, 2015. **2015**: p. 105135.
90. Bigarella, C.L., R. Liang, and S. Ghaffari, *Stem cells and the impact of ROS signaling.* Development, 2014. **141**(22): p. 4206-18.
91. Ryu, J.M., et al., *Regulation of Stem Cell Fate by ROS-mediated Alteration of Metabolism.* Int J Stem Cells, 2015. **8**(1): p. 24-35.

92. Upadhyay, M. and S. Agarwal, *Ironing the mitochondria: Relevance to its dynamics.* Mitochondrion, 2020. **50**: p. 82-87.
93. Sumneang, N., et al., *The effects of iron overload on mitochondrial function, mitochondrial dynamics, and ferroptosis in cardiomyocytes.* Arch Biochem Biophys, 2020. **680**: p. 108241.
94. Fu, W., Y. Liu, and H. Yin, *Mitochondrial Dynamics: Biogenesis, Fission, Fusion, and Mitophagy in the Regulation of Stem Cell Behaviors.* Stem Cells Int, 2019. **2019**: p. 9757201.
95. Levi, S. and E. Rovida, *The role of iron in mitochondrial function.* Biochim Biophys Acta, 2009. **1790**(7): p. 629-36.
96. Gao, X., et al., *Mitochondrial DNA damage in iron overload.* J Biol Chem, 2009. **284**(8): p. 4767-75.
97. Walter, P.B., et al., *Iron deficiency and iron excess damage mitochondria and mitochondrial DNA in rats.* Proc Natl Acad Sci U S A, 2002. **99**(4): p. 2264-9.
98. Willis, W.T. and P.R. Dallman, *Impaired control of respiration in iron-deficient muscle mitochondria.* Am J Physiol, 1989. **257**(6 Pt 1): p. C1080-5.
99. Khacho, M. and R.S. Slack, *Mitochondrial activity in the regulation of stem cell self-renewal and differentiation.* Curr Opin Cell Biol, 2017. **49**: p. 1-8.
100. Park, I.H., et al., *Constitutive stabilization of hypoxia-inducible factor alpha selectively promotes the self-renewal of mesenchymal progenitors and maintains mesenchymal stromal cells in an undifferentiated state.* Exp Mol Med, 2013. **45**: p. e44.
101. Xie, L., et al., *Transient HIF2A inhibition promotes satellite cell proliferation and muscle regeneration.* J Clin Invest, 2018. **128**(6): p. 2339-2355.
102. Das, B., et al., *MYC Regulates the HIF2alpha Stemness Pathway via Nanog and Sox2 to Maintain Self-Renewal in Cancer Stem Cells versus Non-Stem Cancer Cells.* Cancer Res, 2019. **79**(16): p. 4015-4025.
103. Kajimura, S., B.M. Spiegelman, and P. Seale, *Brown and Beige Fat: Physiological Roles beyond Heat Generation.* Cell Metab, 2015. **22**(4): p. 546-59.
104. van Marken Lichtenbelt, W.D., et al., *Cold-activated brown adipose tissue in healthy men.* N Engl J Med, 2009. **360**(15): p. 1500-8.
105. Yoneshiro, T., et al., *Recruited brown adipose tissue as an antiobesity agent in humans.* J Clin Invest, 2013. **123**(8): p. 3404-8.
106. Shabalina, I.G., et al., *Uncoupling protein-1 is not leaky.* Biochim Biophys Acta, 2010. **1797**(6-7): p. 773-84.
107. Cao, W., et al., *beta-Adrenergic activation of p38 MAP kinase in adipocytes: cAMP induction of the uncoupling protein 1 (UCP1) gene requires p38 MAP kinase.* J Biol Chem, 2001. **276**(29): p. 27077-82.
108. Cao, W., et al., *p38 mitogen-activated protein kinase is the central regulator of cyclic AMP-dependent transcription of the brown fat uncoupling protein 1 gene.* Mol Cell Biol, 2004. **24**(7): p. 3057-67.
109. Fedorenko, A., P.V. Lishko, and Y. Kirichok, *Mechanism of fatty-acid-dependent UCP1 uncoupling in brown fat mitochondria.* Cell, 2012. **151**(2): p. 400-13.
110. Chouchani, E.T., et al., *Mitochondrial ROS regulate thermogenic energy expenditure and sulfenylation of UCP1.* Nature, 2016. **532**(7597): p. 112-6.
111. Ro, S.H., et al., *Sestrin2 inhibits uncoupling protein 1 expression through suppressing reactive oxygen species.* Proc Natl Acad Sci U S A, 2014. **111**(21): p. 7849-54.

112. Han, Y.H., et al., *Adipocyte-Specific Deletion of Manganese Superoxide Dismutase Protects From Diet-Induced Obesity Through Increased Mitochondrial Uncoupling and Biogenesis.* Diabetes, 2016. **65**(9): p. 2639-51.
113. Mills, E.L., et al., *Accumulation of succinate controls activation of adipose tissue thermogenesis.* Nature, 2018. **560**(7716): p. 102-106.
114. Chouchani, E.T., L. Kazak, and B.M. Spiegelman, *Mitochondrial reactive oxygen species and adipose tissue thermogenesis: Bridging physiology and mechanisms.* J Biol Chem, 2017. **292**(41): p. 16810-16816.
115. Dixon, S.J. and B.R. Stockwell, *The role of iron and reactive oxygen species in cell death.* Nat Chem Biol, 2014. **10**(1): p. 9-17.
116. Gutteridge, J.M., *Lipid peroxidation initiated by superoxide-dependent hydroxyl radicals using complexed iron and hydrogen peroxide.* FEBS Lett, 1984. **172**(2): p. 245-9.
117. Echtay, K.S., et al., *A signalling role for 4-hydroxy-2-nonenal in regulation of mitochondrial uncoupling.* EMBO J, 2003. **22**(16): p. 4103-10.
118. Malingriaux, E.A., et al., *Fatty acids are key in 4-hydroxy-2-nonenal-mediated activation of uncoupling proteins 1 and 2.* PLoS One, 2013. **8**(10): p. e77786.
119. Mailloux, R.J., et al., *Crucial yet divergent roles of mitochondrial redox state in skeletal muscle vs. brown adipose tissue energetics.* FASEB J, 2012. **26**(1): p. 363-75.
120. Ganz, T., *Systemic iron homeostasis.* Physiol Rev, 2013. **93**(4): p. 1721-41.
121. Levy, J.E., et al., *Transferrin receptor is necessary for development of erythrocytes and the nervous system.* Nat Genet, 1999. **21**(4): p. 396-9.
122. Chen, A.C., et al., *Noncanonical role of transferrin receptor 1 is essential for intestinal homeostasis.* Proc Natl Acad Sci U S A, 2015. **112**(37): p. 11714-9.
123. Barrientos, T., et al., *Metabolic Catastrophe in Mice Lacking Transferrin Receptor in Muscle.* EBioMedicine, 2015. **2**(11): p. 1705-17.
124. Kasibhatla, S., et al., *A role for transferrin receptor in triggering apoptosis when targeted with gambogic acid.* Proc Natl Acad Sci U S A, 2005. **102**(34): p. 12095-100.
125. Richardson, D.R., et al., *Mitochondrial iron trafficking and the integration of iron metabolism between the mitochondrion and cytosol.* Proc Natl Acad Sci U S A, 2010. **107**(24): p. 10775-82.
126. Petrat, F., et al., *Selective determination of mitochondrial chelatable iron in viable cells with a new fluorescent sensor.* Biochem J, 2002. **362**(Pt 1): p. 137-47.
127. Kalyanaraman, B., et al., *Measuring reactive oxygen and nitrogen species with fluorescent probes: challenges and limitations.* Free Radic Biol Med, 2012. **52**(1): p. 1-6.
128. Ma, Y., V. Abbate, and R.C. Hider, *Iron-sensitive fluorescent probes: monitoring intracellular iron pools.* Metallomics, 2015. **7**(2): p. 212-22.
129. Li, L., et al., *Binding and uptake of H-ferritin are mediated by human transferrin receptor-1.* Proc Natl Acad Sci U S A, 2010. **107**(8): p. 3505-10.
130. Todd, T.J., Z. Zhen, and J. Xie, *Ferritin nanocages: great potential as clinically translatable drug delivery vehicles?* Nanomedicine (Lond), 2013. **8**(10): p. 1555-7.
131. Kramarova, T.V., et al., *Mitochondrial ATP synthase levels in brown adipose tissue are governed by the c-Fo subunit P1 isoform.* FASEB J, 2008. **22**(1): p. 55-63.
132. Asano, T., et al., *Experimental evaluation of the beneficial effect of an antioxidant on cerebral vasospasm.* Neurol Res, 1984. **6**(1-2): p. 49-53.
133. Ku, K., et al., *The role of a hydroxyl radical scavenger (nicaraven) in recovery of cardiac function following preservation and reperfusion.* Transplantation, 1996. **62**(8): p. 1090-5.

134. A, A., M. MF, and A. S, *Lipid Peroxidation: Production, Metabolism, and Signaling Mechanisms of Malondialdehyde and 4-Hydroxy-2-Nonenal.* Oxidative Medicine and Cellular Longevity, 2014. **Volume 2014**.
135. Barja de Quiroga, G., et al., *Effect of cold acclimation on GSH, antioxidant enzymes and lipid peroxidation in brown adipose tissue.* Biochem J, 1991. **277 (Pt 1)**: p. 289-92.
136. Quesada-Lopez, T., et al., *The lipid sensor GPR120 promotes brown fat activation and FGF21 release from adipocytes.* Nat Commun, 2016. **7**: p. 13479.
137. Sadurskis, A., et al., *Polyunsaturated fatty acids recruit brown adipose tissue: increased UCP content and NST capacity.* Am J Physiol, 1995. **269**(2 Pt 1): p. E351-60.
138. Braughler, J.M., et al., *Novel 21-amino steroids as potent inhibitors of iron-dependent lipid peroxidation.* J Biol Chem, 1987. **262**(22): p. 10438-40.
139. Schaur, R.J., *Basic aspects of the biochemical reactivity of 4-hydroxynonenal.* Mol Aspects Med, 2003. **24**(4-5): p. 149-59.
140. Collins, Y., et al., *Mitochondrial redox signalling at a glance.* J Cell Sci, 2012. **125**(Pt 4): p. 801-6.
141. Han, E.S., et al., *The in vivo gene expression signature of oxidative stress.* Physiol Genomics, 2008. **34**(1): p. 112-26.
142. Tapryal, N., G.V. Vivek, and C.K. Mukhopadhyay, *Catecholamine stress hormones regulate cellular iron homeostasis by a posttranscriptional mechanism mediated by iron regulatory protein: implication in energy homeostasis.* J Biol Chem, 2015. **290**(12): p. 7634-46.
143. Anderson, C.P., et al., *Mammalian iron metabolism and its control by iron regulatory proteins.* Biochim Biophys Acta, 2012. **1823**(9): p. 1468-83.
144. Zhang, Y., et al., *Lipocalin 2 regulates brown fat activation via a nonadrenergic activation mechanism.* J Biol Chem, 2014. **289**(32): p. 22063-77.
145. Brand, M.D., *Mitochondrial generation of superoxide and hydrogen peroxide as the source of mitochondrial redox signaling.* Free Radic Biol Med, 2016. **100**: p. 14-31.
146. May, F.J., et al., *Lipidomic Adaptations in White and Brown Adipose Tissue in Response to Exercise Demonstrate Molecular Species-Specific Remodeling.* Cell Rep, 2017. **18**(6): p. 1558-1572.
147. Okado-Matsumoto, A. and I. Fridovich, *Subcellular distribution of superoxide dismutases (SOD) in rat liver: Cu,Zn-SOD in mitochondria.* J Biol Chem, 2001. **276**(42): p. 38388-93.
148. Gill, D., et al., *The Effect of Iron Status on Risk of Coronary Artery Disease: A Mendelian Randomization Study-Brief Report.* Arterioscler Thromb Vasc Biol, 2017. **37**(9): p. 1788-1792.
149. Rocha, B.M.L., G.J.L. Cunha, and L.F. Menezes Falcao, *The Burden of Iron Deficiency in Heart Failure: Therapeutic Approach.* J Am Coll Cardiol, 2018. **71**(7): p. 782-793.
150. Corna, G., et al., *The Repair of Skeletal Muscle Requires Iron Recycling through Macrophage Ferroportin.* J Immunol, 2016. **197**(5): p. 1914-25.
151. Hoffmann, C., et al., *The effect of differentiation and TGFbeta on mitochondrial respiration and mitochondrial enzyme abundance in cultured primary human skeletal muscle cells.* Sci Rep, 2018. **8**(1): p. 737.
152. Sin, J., et al., *Mitophagy is required for mitochondrial biogenesis and myogenic differentiation of C2C12 myoblasts.* Autophagy, 2016. **12**(2): p. 369-380.

153. Jiang, Y., et al., *Iron-dependent histone 3 lysine 9 demethylation controls B cell proliferation and humoral immune responses.* Nat Commun, 2019. **10**(1): p. 2935.
154. Kuvibidila, S.R., et al., *Reduced thymocyte proliferation but not increased apoptosis as a possible cause of thymus atrophy in iron-deficient mice.* Br J Nutr, 2001. **86**(2): p. 157-62.
155. Pourcelot, E., et al., *Iron for proliferation of cell lines and hematopoietic progenitors: Nailing down the intracellular functional iron concentration.* Biochim Biophys Acta, 2015. **1853**(7): p. 1596-605.
156. Yan, Z., et al., *Highly coordinated gene regulation in mouse skeletal muscle regeneration.* J Biol Chem, 2003. **278**(10): p. 8826-36.
157. Hosoyama, T., et al., *Rb1 gene inactivation expands satellite cell and postnatal myoblast pools.* J Biol Chem, 2011. **286**(22): p. 19556-64.
158. Sousa-Victor, P., et al., *Geriatric muscle stem cells switch reversible quiescence into senescence.* Nature, 2014. **506**(7488): p. 316-21.
159. Sousa-Victor, P., E. Perdiguero, and P. Munoz-Canoves, *Geroconversion of aged muscle stem cells under regenerative pressure.* Cell Cycle, 2014. **13**(20): p. 3183-90.
160. Motohashi, N., Y. Asakura, and A. Asakura, *Isolation, culture, and transplantation of muscle satellite cells.* J Vis Exp, 2014(86).
161. Epsztejn, S., et al., *Fluorescence analysis of the labile iron pool of mammalian cells.* Anal Biochem, 1997. **248**(1): p. 31-40.
162. Schiaffino, S., et al., *Developmental myosins: expression patterns and functional significance.* Skelet Muscle, 2015. **5**: p. 22.
163. Wallace, E.M., et al., *A Small-Molecule Antagonist of HIF2alpha Is Efficacious in Preclinical Models of Renal Cell Carcinoma.* Cancer Res, 2016. **76**(18): p. 5491-500.
164. Johnson, D.G., et al., *Expression of transcription factor E2F1 induces quiescent cells to enter S phase.* Nature, 1993. **365**(6444): p. 349-52.
165. Wu, L., et al., *The E2F1-3 transcription factors are essential for cellular proliferation.* Nature, 2001. **414**(6862): p. 457-62.
166. Harbour, J.W. and D.C. Dean, *The Rb/E2F pathway: expanding roles and emerging paradigms.* Genes Dev, 2000. **14**(19): p. 2393-409.
167. Luo, R.X., A.A. Postigo, and D.C. Dean, *Rb interacts with histone deacetylase to repress transcription.* Cell, 1998. **92**(4): p. 463-73.
168. Ferreira, R., et al., *Cell cycle-dependent recruitment of HDAC-1 correlates with deacetylation of histone H4 on an Rb-E2F target promoter.* EMBO Rep, 2001. **2**(9): p. 794-9.
169. Sheehan, S.M. and R.E. Allen, *Skeletal muscle satellite cell proliferation in response to members of the fibroblast growth factor family and hepatocyte growth factor.* J Cell Physiol, 1999. **181**(3): p. 499-506.
170. Pawlikowski, B., et al., *Regulation of skeletal muscle stem cells by fibroblast growth factors.* Dev Dyn, 2017. **246**(5): p. 359-367.
171. Fernyhough, M.E., et al., *The Effect of Nutritional Supplements on Muscle-Derived Stem Cells in vitro.* Int J Stem Cells, 2010. **3**(1): p. 63-7.
172. Harthan, L.B., D.C. McFarland, and S.G. Velleman, *The effect of nutritional status and myogenic satellite cell age on turkey satellite cell proliferation, differentiation, and expression of myogenic transcriptional regulatory factors and heparan sulfate proteoglycans syndecan-4 and glypican-1.* Poult Sci, 2014. **93**(1): p. 174-86.

173. Vest, K.E., et al., *Dynamic changes in copper homeostasis and post-transcriptional regulation of Atp7a during myogenic differentiation.* Metallomics, 2018. **10**(2): p. 309-322.
174. Ding, H., et al., *Transferrin receptor 1 ablation in satellite cells impedes skeletal muscle regeneration through activation of ferroptosis.* J Cachexia Sarcopenia Muscle, 2021.
175. Antico Arciuch, V.G., et al., *Mitochondrial regulation of cell cycle and proliferation.* Antioxid Redox Signal, 2012. **16**(10): p. 1150-80.
176. Malecki, M., et al., *Mitochondrial respiration is required to provide amino acids during fermentative proliferation of fission yeast.* EMBO Rep, 2020. **21**(11): p. e50845.
177. Sullivan, L.B., et al., *Supporting Aspartate Biosynthesis Is an Essential Function of Respiration in Proliferating Cells.* Cell, 2015. **162**(3): p. 552-63.
178. Garcia-Bermudez, J., et al., *Aspartate is a limiting metabolite for cancer cell proliferation under hypoxia and in tumours.* Nat Cell Biol, 2018. **20**(7): p. 775-781.
179. Mick, E., et al., *Distinct mitochondrial defects trigger the integrated stress response depending on the metabolic state of the cell.* Elife, 2020. **9**.
180. Birsoy, K., et al., *An Essential Role of the Mitochondrial Electron Transport Chain in Cell Proliferation Is to Enable Aspartate Synthesis.* Cell, 2015. **162**(3): p. 540-51.
181. Bosutti, A. and H. Degens, *The impact of resveratrol and hydrogen peroxide on muscle cell plasticity shows a dose-dependent interaction.* Sci Rep, 2015. **5**: p. 8093.
182. Nindl, G., et al., *Effect of hydrogen peroxide on proliferation, apoptosis and interleukin-2 production of Jurkat T cells.* Biomed Sci Instrum, 2004. **40**: p. 123-8.
183. Zhou, X., et al., *Signaling in H2O2-induced increase in cell proliferation in Barrett's esophageal adenocarcinoma cells.* J Pharmacol Exp Ther, 2011. **339**(1): p. 218-27.

APPENDICES

LIST OF PUBLICATIONS

1. Jiang W, Yin L, Chen H, Paschall AV, Zhang L, **Fu W**, Zhang W, Todd T, Yu KS, Zhou S, Zhen Z, Butler M, Yao L, Zhang F, Shen Y, Li Z, Yin A, Yin H, Wang X, Avci FY, Yu X, Xie J. NaCl Nanoparticles as a Cancer Therapeutic. *Adv Mater*. 2019
2. Liu Y, **Fu W**, Seese K, Yin A, Yin H. Ectopic brown adipose tissue formation within skeletal muscle after brown adipose progenitor cell transplant augments energy expenditure. *FASEB J*. 201
3. **Fu W**, Liu Y, Yin H. Mitochondrial Dynamics: Biogenesis, Fission, Fusion, and Mitophagy in the Regulation of Stem Cell Behaviors. *Stem Cells Int*. 2019
4. **Fu W**, Liu Y, Sun C, Yin H. Transient p53 inhibition sensitizes aged white adipose tissue for beige adipocyte recruitment by blocking mitophagy. *FASEB J.* 2019
5. Chen HZ, Wang F, Gao P, Pei JF, Liu Y, Xu TT, Tang X, **Fu WY**, Lu J, Yan YF, Wang XM, Han L, Zhang ZQ, Zhang R, Zou MH, Liu DP. Age-Associated Sirtuin 1 Reduction in Vascular Smooth Muscle Links Vascular Senescence and Inflammation to Abdominal Aortic Aneurysm. *Circ Res*. 2016
6. Liu Y, Wang TT, Zhang R, **Fu WY**, Wang X, Wang F, Gao P, Ding YN, Xie Y, Hao DL, Chen HZ, Liu DP. Calorie restriction protects against experimental abdominal aortic aneurysms in mice. *J Exp Med*. 2016

7. Mu W, Zhang Q, Tang X, **Fu W**, Zheng W, Lu Y, Li H, Wei Y, Li L, She Z, Chen H, Liu D. Overexpression of a dominant-negative mutant of SIRT1 in mouse heart causes cardiomyocyte apoptosis and early-onset heart failure. Sci China Life Sci. 2014